Quantum nanophotonics with ytterbium in yttrium orthovanadate

Thesis by
Jonathan Miners Kindem

In Partial Fulfillment of the Requirements for the
Degree of
Doctor of Philosophy

CALIFORNIA INSTITUTE OF TECHNOLOGY
Pasadena, California

2019
Defended March 14, 2019

Jonathan Miners Kindem
ORCID: 0000-0002-7737-9368

ACKNOWLEDGEMENTS

Thank you Andrei for being such a wonderful advisor throughout my time at Caltech. Your enthusiasm and excitement for doing science is contagious. Thanks for your patience as I climbed out of various “pits of incompetency" over the years and for having a good sense of humor. Thank you for setting high expectations for our work while giving me freedom in the lab to pursue things I found interesting. It’s been a lot of fun.

Thank you to the Faraon group: Tian for getting me up to speed in the lab and teaching me so much over the years. Evan for all the late-night chats in the office and trips to the climbing gym. John for always being willing to answer “quick questions” that were never really quick questions and for your enthusiasm for rare-earths. Jake for keeping the rare-earth ego in check and for fabricating nanobeams. Andrei R. for bringing a fresh set of eyes to the experiment and for the fun times getting the singles measurements working. I’m glad to be leaving the experiment in good hands and look forward to seeing where experiments go in the future. Ioana for always being a source of positivity in lab and for letting me monopolize the fridge over the last few months. Chuting for your kindness over the years. Tian and Mi for bringing your energy to the lab. Yan Qi for answering all my questions about Python. The entire flat optics subgroup for listening to all the rare-earths talks over the years and for your friendship.

Thank you to friends from Caltech that helped me escape from lab on occasion: The Steuben house for all the parties. Everyone in the Greer group for letting me tag along on your social events. Ivan and David for burgers and beers. All the friends that went on ski trips with me. Nick for mountain bikes, skiing, and all the bad puns. Max for the morning bike rides.

Thank you to my friends from Reed that helped me relax and refocus: Will and Alec for bikes. Zach for trips to Telluride. Erin for all the laughs.

Thank you to Ottman and Asher for being fun housemates and good friends.

Thanks to Prof. Painter, Prof. Vahala, and Prof. Hutzler for serving on my committee and for the excellent classes early in my time at Caltech.

Thank you to all the wonderful administrators at Caltech that make things run so smoothly. Especially thank you to Cecilia for putting up with my late receipts!

Thanks to Rufus and Charles for your hospitality during our trip to Bozeman and for sharing your overflowing knowledge on rare-earths.

Thanks to my professors from Reed for getting me interested in physics in the first place. Thanks to Dr. Justin Taraska for showing me how fun it can be to do research.

Thanks to my brothers for always making fun of me for never having a tan even though I live in southern California. Thanks to my parents for their support and confidence in me throughout my academic career.

Thanks to anyone I might have missed. And thanks to the reader for reading!

ABSTRACT

Quantum light-matter interfaces that can reversibly map quantum information between photons and atoms are essential for building future quantum networks. Crystals doped with rare-earth ions (REIs) are an attractive solid-state platform for such light-matter interfaces due to their exceptional optical and spin coherence properties at cryogenic temperatures. Building scalable REI-based technology has proven to be challenging due to the inherently weak coupling of REIs with light. This thesis explores the integration of REIs with nanophotonic resonators to overcome this weak light-matter interaction and enable efficient, scalable quantum light-matter interfaces. Specifically, this work focuses on the development of quantum nanophotonics with ytterbium in yttrium orthovanadate (Yb^{3+}:YVO_4).

This thesis begins with an introduction to a nanophotonic platform based on photonic crystal cavities fabricated directly in rare-earth host materials and highlights the initial successes of this platform with neodymium-doped materials. This motivates an examination of the optical and spin coherence properties of ^{171}Yb:YVO_4, a REI material that was previously unexplored for quantum technology applications. This material is found to have strong optical transitions compared to other REI-doped materials, a simple energy level structure, and long optical and spin coherence lifetimes.

The focus then turns to the detection and coherent manipulation of single ytterbium ions coupled to nanophotonic cavities. The Purcell-enhancement in these cavities enables efficient optical detection and spin initialization of individual ytterbium ions. We identify ions corresponding to different isotopes of ytterbium and show that the coupling of electron and nuclear spin in ytterbium-171 at zero-field gives rise to strong electron-spin-like transitions that are first-order insensitive to magnetic field fluctuations. This allows for coherent microwave control and the observation of long spin coherence lifetimes at temperatures up to 1 K. We then make use of the optical selection rules and energy structure of ^{171}Yb:YVO_4 to demonstrate high-fidelity single-shot optical readout of the spin state. These results establish nanophotonic devices in ^{171}Yb:YVO_4 as a promising platform for solid-state quantum light-matter interfaces.

PUBLISHED CONTENT AND CONTRIBUTIONS

1. J.M. Kindem, A. Ruskuc, J.G. Bartholomew, J. Rochman, and A. Faraon,"Optical detection and spin manipulation of single Yb ions in yttrium orthovanadate," *In preparation*.

JMK built experimental setup, performed measurements, processed data, and wrote manuscript.

2. T. Zhong, J.M. Kindem, J.G. Bartholomew, J. Rochman, I. Craiciu, V. Verma, S.W. Nam, F. Marsili, M. D Shaw, A. D. Beyer, A. Faraon. "Optically addressing single rare-earth ions in a nanophotonic cavity," In: *Physical Review Letters* 121, 183603 (2018) DOI: 10.1103/PhysRevLett.121.183603.

JMK built experimental setup, performed measurements, and helped with writing of manuscript.

3. J.M. Kindem, J.G. Bartholomew, P.J.T. Woodburn, T. Zhong, I. Craiciu, R. L. Cone, C. W. Thiel, and A. Faraon,"Characterization of ^{171}Yb:YVO_4 for photonic quantum technologies," In: *Physical Review B*, 80, 024404, (2018) DOI: 10.1103/PhysRevB.98.024404

JMK built experimental setup, performed measurements, processed data, and wrote manuscript.

4. J.G. Bartholomew, T. Zhong, J.M Kindem, R. Lopez-Rios, J. Rochman, I. Craiciu, E. Miyazono, A. Faraon, "Controlling rare-earth ions in a nanophotonic resonator using the ac Stark shift," In: *Physical Review A*, 97, 063854 (2018) DOI 10.1103/PhysRevA.97.063854

JMK built experimental setup, performed measurements, and helped with writing of manuscript.

5. T. Zhong, J.M. Kindem, J. G. Bartholomew, J. Rochman, I. Craiciu, E. Miyazono, M. Bettinelli, E. Cavalli, V. Verma, S. W. Nam, F. Marsili, M. D. Shaw, A. D. Beyer, and A. Faraon, "Nanophotonic rare-earth quantum memory with optically controlled retrieval," In: *Science*, vol. 1395, pp. 1392 -1395, (2017). DOI: 10.1126/science.aan5959

JMK built experimental setup, performed measurements, processed data, and helped with writing of manuscript.

6. T. Zhong, J.M. Kindem, J. Rochman, and A. Faraon, "Interfacing broadband photonic qubits to on-chip cavity-protected rare-earth ensembles," In: *Nature Communications*, vol. 8, pp. 1- 7, (2017). DOI: 10.1038/ncomms14107

JMK built experimental setup, performed measurements, processed data, and helped with writing of manuscript.

7 . T. Zhong, J. Rochman, J.M. Kindem, E. Miyazono, and A. Faraon,"High quality factor nanophotonic resonators in bulk rare-earth doped crystals," In: *Optics Express*, vol. 24, no. 1, p. 536, (2016). DOI: 10.1364/OE.24.000536

JMK performed measurements of nanocavities.

8 . T. Zhong, J.M. Kindem, E. Miyazono, and A. Faraon,"Nanophotonic coherent light-matter interfaces based on rare-earth-doped crystals," In: *Nature Communications*, vol. 6, p. 8206, (2015). DOI: 10.1038/ncomms9206

JMK built experimental setup, performed measurements, processed data, and helped with writing of manuscript.

TABLE OF CONTENTS

Acknowledgements . . . iii
Abstract . . . v
Published Content and Contributions . . . vi
Table of Contents . . . viii
List of Illustrations . . . x
List of Tables . . . xii
Chapter I: Introduction . . . 1
1.1 Structure of this thesis . . . 3
1.2 Basics of rare-earth ion physics . . . 3
1.3 What's been done with the rare-earth ions? . . . 7
1.4 Photonic crystal cavities fabricated in rare-earth ion hosts . . . 9
Chapter II: Nanophotonic interfaces in Nd:YSO and Nd:YVO . . . 11
2.1 Preservation of optical coherence in nanocavities . . . 11
2.2 Ensemble strong coupling . . . 13
2.3 Nanophotonic quantum memory . . . 14
2.4 Detection of single ions . . . 15
2.5 Toward coherent spin control . . . 15
Chapter III: Spectroscopy of ^{171}Yb:YVO_4 . . . 17
3.1 Introduction . . . 17
3.2 Background . . . 18
3.3 Experimental Methods . . . 20
3.4 Optical and spin properties of ^{171}Yb:YVO_4 . . . 24
3.5 Summary and Conclusion . . . 33
Chapter IV: Theory: An ion in a cavity . . . 36
4.1 Setting up the problem . . . 36
4.2 Bad cavity limit . . . 38
4.3 Purcell Enhancement . . . 41
4.4 Cavity reflection spectrum in the low excitation regime . . . 44
4.5 What do we expect to be able to achieve? . . . 50
Chapter V: Experimental setup for single ion work . . . 53
5.1 Sample . . . 54
5.2 Triangular nanobeam photonic crystal resonators in YVO . . . 55
5.3 Montana Cryostat . . . 58
5.4 Bluefors Dilution Refrigerator . . . 59
5.5 Optical setup . . . 64
5.6 Microwave sources . . . 71
Chapter VI: Measurements of a single Yb ion in YVO . . . 74
6.1 Detection of single ions . . . 74
6.2 Line scans and spectral diffusion . . . 78

6.3 Determining coupling rate to cavity . . . 80
6.4 Verifying that we have a single ion . . . 80
6.5 Zeeman splitting in an applied magnetic field . . . 84
6.6 Optical pumping with single ions . . . 85
6.7 Cross-correlation measurements . . . 87
6.8 Spin initialization . . . 90
6.9 Optical coherence measurements . . . 91
6.10 Optically detected magnetic resonance . . . 95
6.11 Spin coherence measurements . . . 96
6.12 Conclusion . . . 97
Chapter VII: Measurements of single ^{171}Yb:YVO_4 ions . . . 98
7.1 Why work at zero field? . . . 98
7.2 Zero-field level structure and initialization . . . 101
7.3 Identifying single 171 ions . . . 103
7.4 Photon correlation measurements . . . 105
7.5 Lifetime measurements . . . 106
7.6 Spectral diffusion . . . 106
7.7 ODMR measurements . . . 107
7.8 Spin initialization . . . 109
7.9 Coherent optical measurements . . . 111
7.10 Coherent spin measurements . . . 114
7.11 Extending the spin coherence . . . 116
7.12 Spin lifetime . . . 119
7.13 Single-shot spin readout . . . 120
Chapter VIII: Future directions . . . 126
8.1 Limitations to zero-field coherence lifetimes . . . 126
8.2 Coupling to nearby spins . . . 127
8.3 Toward generation of entanglement . . . 127
8.4 Conclusion . . . 129
Bibliography . . . 130
Appendix A: Transition selection rules in ^{171}Yb:YVO_4 . . . 144
A.1 Setting up the problem . . . 144
A.2 Calculating transition strengths from the spin Hamiltonian . . . 147

LIST OF ILLUSTRATIONS

Number *Page*

1.1 Example of the photonic crystal nanobeam resonators used in the Faraon group 10
2.1 Highlights from [1] 12
2.2 Highlights from [2]. 13
2.3 Highlights from [3] 14
2.4 Highlights from [4]. 15
3.1 Energy level diagram for ^{171}Yb:YVO_4 21
3.2 Optical absorption in ^{171}Yb:YVO_4 24
3.3 Magnetic field ramp in ^{171}Yb:YVO_4 26
3.4 Excited-state lifetime measurement 28
3.5 Photon echo measurements. 29
3.6 Nuclear spin inhomogeneity. 31
3.7 Nuclear spin echo decays. 32
3.8 All-optical nuclear spin echo decays 33
4.1 Jaynes-Cummings model 37
4.2 Semi-classical reflection spectrum. 47
4.3 Corrected semi-classical expressions. 50
5.1 SEM images of device used for measurement. 55
5.2 Cavity reflection spectrum. 57
5.3 Bluefors sample mount. 58
5.4 Confocal microscope setup in Montana cryostat. 59
5.5 Layout of singles experiment in Bluefors. 60
5.6 Schematic of optical network used for measurements of single ions . 65
5.7 Frequency drift of M^2 Ti:Sapph 68
5.8 Simplified schematic of microwave setup. 72
6.1 Single photon counting integration time estimates. 76
6.2 PLE scan in nanocavity 78
6.3 Fine PLE scans over ion Z. 79
6.4 Lifetime measurement on ion Z. 80
6.5 $g^{(2)}$ measurement on ion Z 83
6.6 PLE scans in magnetic field. 85

6.7 Zeeman splitting of ion Z. 86
6.8 Correlation measurements on ion Z. 90
6.9 Spin initialization of ion Z. 92
6.10 Spin lifetime measurement on ion Z. 92
6.11 Optical Rabi oscillations on ion Z. 94
6.12 Optical echo on ion Z. 94
6.13 Schematic for ODMR measurement. 95
6.14 ODMR on ion Z. 96
6.15 Coherent spin measurements on ion Z. 97
7.1 Zero-field energy level structure of ^{171}Yb:YVO_4 99
7.2 Overlap of different Yb isotopes. 101
7.3 Level structure of ^{171}Yb:YVO_4 for singles experiments. 102
7.4 Fine PLE scan over transition *A*. 104
7.5 Verification of Yb-171 ions. 104
7.6 Second-order photon correlation measurements on ion **A** 106
7.7 Optical lifetime measurements on ions **A** and **A**. 107
7.8 Spectral diffusion scans 107
7.9 Ground-state ODMR. 108
7.10 Excited state ODMR 109
7.11 Example of spin initialization 110
7.12 Optical Rabi oscillations on transition *A* 112
7.13 Optical coherence measurements. 112
7.14 Prediction of bulk T2 113
7.15 Rabi oscillations of ^{171}Yb:YVO_4 spin. 114
7.16 Spin Ramsey measurements. 115
7.17 Spin echo measurements 116
7.18 Initial CPMG measurements. 117
7.19 Fine CPMG measurements. 118
7.20 Fixed CPMG scans. 118
7.21 Measurement of spin lifetime. 120
7.22 Single-shot readout with single readout sequence. 121
7.23 Optical branching ratio measurement. 122
7.24 Improved single-shot readout scheme. 124
7.25 Implementation of improved single-shot readout scheme. 125

LIST OF TABLES

Number *Page*

3.1 Absorption properties of the ^{171}Yb:YVO_4 transitions as labeled in Fig. 3.2, including the transition polarization [5], integrated absorption coefficient, oscillator strength, and radiative decay rate at zero magnetic field. 27

4.1 Table of expected system parameters for the Yb:YVO system assuming $Q = 10^4$ and $V \approx 1(\lambda/n)^3$ as described in text assuming different local field correction factors in extracting the dipole moment from the absorption measurements. These predictions are the best case scenario in which we assume an ion maximally coupled and aligned to the cavity mode. 52

A.1 Character table for D_{2d} 145

A.2 Character table for angular momentum states 145

A.3 Electric dipole selection rules in D_{2d} 146

A.4 Electric dipole transition selection rules 147

Chapter 1

INTRODUCTION

Interest in quantum technologies has exploded in recent years with the promise of quantum computers that can outperform their classical counterparts, ultra-secure communication guaranteed by the laws of quantum mechanics, and advances in precision metrology. The aim of this “second quantum revolution" [6] is to create useful technologies that harness quantum mechanical effects such as superposition and entanglement. Fundamental to this goal is the ability to both control and read-out individual quantum systems and engineer interactions between them to enable scalability. Despite impressive experimental efforts, the fragile nature of quantum states makes direct scaling to build large quantum systems an outstanding challenge.

Quantum networks, in which quantum nodes for processing and storing quantum information are connected by quantum channels, have emerged as a route to building scalable and flexible quantum-enhanced technologies that can make use of relatively elementary quantum systems currently available [7]. Optical photons are excellent carriers of quantum information and the ideal candidate for establishing long-distance, room-temperature links between quantum nodes. The challenge lies in finding a way to efficiently and reversibly map information from light into quantum nodes where it can be stored and processed. The development of such quantum light-matter interfaces is then of vital importance to the successful implementation of a quantum network.

Among the wide variety of approaches and platforms that have been developed toward this goal [8–10], solid-state spins with optical transitions offer a promising route to robust and scalable light-matter interfaces. There are many different optically-addressable solid-state spins currently being investigated for this application, including quantum dots, color centers in diamond or silicon carbide, donors in silicon, and rare-earth ions in solids (see [11] for an excellent review of the state-of-the-art in these systems at the time of writing).

In order for a solid-state quantum emitter to be useful in the context of a quantum network, it must have long spin coherence lifetimes to enable storage of quantum information and spectrally stable optical transitions to enable the generation of indistinguishable photons necessary for entanglement generation. To enable the effi-

cient extraction of emitted photons into a well-defined optical mode, these emitters should be coupled to optical cavities. Crucially, the emitters must maintain their desired spin and optical properties when integrated into these cavities.

Finding a system that can satisfy these requirements is a fundamental challenge in the field of solid-state quantum emitters. Quantum dots have efficient interactions with light, but suffer from large inhomogeneous broadening (i.e. the wavelength of emission between different quantum dots on the same substrate is very different) and short spin coherence times [12]. This reduces indistinguishability and makes establishing entanglement over large distances difficult. Nitrogen vacancies (NVs) in diamond have been one of the most well-studied solid-state systems for quantum networks [11], but suffer from low photon collection efficiency and degradation of optical properties when integrated with nanophotonics [13]. Silicon vacancies (SiVs) have emerged recently as a promising alternative to the NV with superior optical properties and integration with nanophotonic structures [14, 15]. One disadvantage of this system is that achieving long coherence times requires operation at dilution refrigerator temperatures (<100 mK) [16, 17].

Rare-earth ions (REIs) in solids combine exceptional optical coherence properties with electron and nuclear spin states that offer the possibility of fast microwave manipulation and long-term storage. These exceptional properties come at the cost of weak optical transitions, which provides a challenge for building efficient light-matter interfaces. As a result, most demonstrations using rare-earth ions for light-matter interfaces have relied on ensembles of emitters in bulk crystals to provide a stronger interaction with light. To overcome this, we can take the approach of cavity quantum electrodynamics (CQED) and integrate these ions into optical cavities with small-mode volumes and high quality factors. By engineering the environment of the REIs in this way, we can enhance the interaction at the single-photon level and enable new quantum technologies using the REIs.

This thesis presents recent progress on the development of a quantum light-matter interface based on a nanophotonic cavity coupled to single $^{171}Yb^{3+}$ ions in the yttrium orthovanadate (YVO_4) host crystal. Purcell-enhancement in the nanocavity enables efficient optical detection and spin initialization of individual Yb^{3+} ions. We identify single $^{171}Yb^{3+}$ ions and show that the coupling of electron and nuclear spin gives rise to strong electron-spin transitions that are first-order insensitive to magnetic field fluctuations. This allows for coherent microwave control and the observation of long spin coherence times at temperatures up to 1 K. Furthermore,

the optical selection rules and energy structure of ^{171}Yb:YVO_4 enable high-fidelity single-shot optical readout of the spin state. These results are the first of their kind for rare-earth ions and point to a promising solid-state technology for quantum networks.

1.1 Structure of this thesis

The rest of this chapter provides more background for the thesis with a brief survey of rare-earth ion physics and an introduction to the nanophotonic platform that is the foundation of this work.

Chapter 2 highlights the initial successes of this nanophotonic platform with neodymium-doped materials. These experiments were the focus of the first few years of my time at Caltech and set the stage for the work in ^{171}Yb:YVO_4 that is the main focus of this thesis.

Chapter 3 is an in-depth investigation into a REI material that was previously unexplored for applications in quantum technologies: the 171 isotope of Yb in YVO. We measure the optical transition strengths, determine the spin Hamiltonian, and assess the optical and nuclear spin coherence properties of this system. These results point to ^{171}Yb:YVO_4 as a promising material for quantum technologies.

Chapter 4 provides the basic theoretical background necessary to understanding the experiments with single ions. This is primarily a review of the Jaynes-Cummings model in the bad-cavity limit and Purcell enhancement.

Chapter 5 provides an overview of the experimental setup used for measurements of single Yb ions.

Chapters 6 and 7 present the main result: detection and manipulation of single Yb ions in a nanophotonic cavity. Chapter 6 focuses on the properties of an ion that we determine to have zero nuclear spin. Chapter 7 builds on these results with measurements of single Yb-171 ions.

Chapter 8 concludes with a discussion of some of the "known unknowns" in this system and measurements to explore in the future.

1.2 Basics of rare-earth ion physics

In this section, I will give a heavily abridged introduction to the physics of rare-earth ions in solid-state hosts. Rather than rewrite or reproduce the many excellent

textbooks written on the subject over the years [1], my goal here is to give the reader a general lay of the land and point to the relevant resources for the interested reader. In Chapter 3, I will elaborate further when we take a closer look at the specific material system used for the work in this thesis.

In the context of solid-state spectroscopy, the rare-earth ions of interest are the lanthanides from cerium to ytterbium. In solids, these are most commonly found in the trivalent state, where they take the form of a xenon core with a partly filled $4f$ shell: $[Xe]4f^N$, where $N = 1$ for cerium up to $N = 13$ for ytterbium. We are interested in, and are usually referring to, the transitions occurring within the manifold of $4f$ electrons. The interesting and unique properties of the rare-earth ions result from the localized nature of these $4f$ orbitals. The $4f$ electron orbitals are closer to the nucleus than the $5s$ and $5p$ orbitals, and so these outer orbitals act to shield the $4f$ electrons. This is often likened to a partial Faraday cage in the sense that the ions are shielded from the electric field of the crystal. The result is that the $4f$ electrons have little participation in chemical bond formation and their energy structure is only slightly modified from the case of free ion when placed in a solid-state host. This then invokes the picture of a trapped ion in the solid state.

The energy levels within the $4f$ shell are determined starting from the free ion. One can determine these with the standard approaches from the quantum theory of atomic spectroscopy with a multi-electron Hamiltonian that includes the mutual Coulomb interaction and spin-orbit coupling. In the case of rare-earths, the magnitude of the Coulomb and spin-orbit coupling are of a similar magnitude. Calculations of the resulting energy levels can get quite close to the observed energy levels, but typically the constants used in describing these interactions are extracted from fits to the observed spectra. These calculations are quite cumbersome, but the free energy levels of most all the rare-earths have been deduced in this way. These then provide good free-ion wavefunctions that can be used to describe the energy levels once we place them in solids. The free states of this ion are typically described in Russell-Saunders notation with quantum numbers S, L, and J (spin, orbital angular momentum, and total angular momentum) with standard spectroscopic notation $^{2S+1}L_J$. Luckily for the modern worker in the field, one does not need to start from scratch when approaching a new system or slog through the aforementioned calculations thanks to the tireless efforts of many dedicated spectroscopists over the past 100 years.

[1] See the end of this section for a list of recommended resources.

Once placed in a solid, the resulting crystal field leads to a perturbation of the spin-orbit coupling and breaks the degeneracy of the spin-orbit manifolds. Because the specific crystalline environment is a relatively weak perturbation to the free ion energy levels, the energy levels of a given rare-earth ion in a typical host can be taken as representative of the energy level structure in all hosts. One ubiquitous reference is the compilation of all the energy levels of the rare-earths in $LaCl_3$, commonly referred to as the Dieke diagram [18]. If the site symmetry is known, one can use group theory to determine the number of crystal field levels that a free ion term with total angular momentum J will split into and determine their symmetry properties (e.g., transition selection rules). While assigning the states in this way is straightforward, calculating the magnitude of this crystal field splitting is substantially harder. The crystal field theory can do fairly well, but ultimately relies on spectroscopy to feed back to the crystal field models. This is again quite cumbersome and there are still research groups actively focused on solving such models. (See, e.g., [19] for a recent example of this applied to $^{167}Er{:}Y_2SiO_5$.)

We are usually interested in optical transitions between the lowest energy crystal field levels of different total angular momentum states. These transitions are usually electric dipole in nature. Since these transitions are within the $4f$ orbital, they should be forbidden by the parity selection rule. That these transitions are partially allowed can typically be explained by the crystal field mixing the $4f$ levels with states of opposite parity (such as $5d$ states). These transitions are then called induced or forced electric dipole transitions and this provides an explanation for the weak oscillator strengths of the rare-earth ion optical transitions.

As the local crystal fields determine the energy levels, variations in the crystal field between site to site due to imperfections in the crystal lattice (including the imperfections caused by the rare-earths themselves!) lead to inhomogeneous broadening of the rare-earth transitions. This is a static inhomogeneous distribution that for the optical transition can be anywhere from $\sim$ 10 MHz to $>$ 10 GHz depending on the specific host crystal and rare-earth used.

The number of levels that the free ion term will split into also depends on the properties of the ion itself. For ions with an odd number of electrons (e.g. the ones we are primarily focused on in the Faraon group: Nd, Yb, and Er), Kramers' theorem states that each crystal field level must be at least two-fold degenerate in the presence of only electric fields. Each J level will then split into $J+\frac{1}{2}$ states. These states are referred to as Kramers doublets and often serve as effective spin 1/2 systems.

Further structure is defined by the hyperfine interaction between the nuclear magnetic moment and electronic magnetic moment. The zero-field degeneracy of these resulting hyperfine levels will be determined by the symmetry. In a magnetic field, we also add in the Zeeman interaction which leads to a breaking of the remaining degeneracy.

While these levels can in principle be described in terms of mixtures of m_j states, the energies and interactions within a given crystal field level are usually written down in terms of an effective spin Hamiltonian. Once completely determined[2], this spin Hamiltonian allows one to determine how energy states will behave in an applied magnetic and make predictions on the relative strengths of optical and spin transitions. While it does not give a complete picture and one must be aware of its limits, this spin Hamiltonian is typically of the most utility to the experimentalist.

Coherence properties

Since the optical transitions within the $4f$ shell are only weakly allowed, the corresponding optical lifetimes of the transitions of interest (between the lowest crystal field levels of the LSJ configurations) are quite long and range from $\sim$ 100 μs to $>$ 10 ms. The coherence properties are then primarily determined by the coherence lifetimes of the underlying spin transitions. At room temperature, the coherence of the spin transition is limited by spin lattice relaxation. This spin lattice relaxation scales drastically with temperature. The spin lattice relaxation is mediated by direct or indirect photon processes with the dominant interaction at higher temperatures being the multi-phonon transitions through close lying crystal field levels. For Kramers ions, the relaxation time for the direct process scales with magnetic field B and temperature T as $|B|^{-2}T^{-1}$ and the indirect process scales as T^{-9}. In practice, this means spin lattice relaxation dominates the dynamics of the spin states until the crystal is cooled below liquid helium temperatures. At this point, the spin lifetime is also limited by cross relaxation (flip-flop) processes between the different ions. This rate depends on concentration and spin linewidth, so can typically be mitigated by working with dilute samples.

At cryogenic temperatures, the optical and spin coherence lifetimes are typically dominated by magnetic fluctuations. Once interactions with other rare-earths are

[2]This determination of the spin Hamiltonian can be quite difficult, especially for Kramers ions with high nuclear spin in low symmetry crystals, e.g., ^{167}Er:Y_2SiO_5 [19]. We will write down the spin Hamiltonian for ^{171}Yb:YVO_4 in the next chapter and should consider ourselves lucky to have a system that gives such a simple spin Hamiltonian.

taken care of by working with dilute samples, the main contribution to these magnetic fluctuations is from the nuclear magnetic moments of the dopants making up host crystal. For this reason, one typically works in hosts that are as "quiet" as possible. Yttrium orthosilicate (YSO) is a popular choice as the dominant magnetic moment in this material is yttrium, which has a magnetic moment of $0.14\mu_N$. By applying a large magnetic field, one can align these host crystal nuclei and significantly slow down their contribution to the dephasing. We can further reduce the sensitivity to magnetic field fluctuations by finding optical and spin transitions that are first-order insensitive to magnetic field. The recipe for maximizing coherence lifetimes in rare-earths is then crudely summarized as follows: go cold, work with a quiet host crystal at low doping concentrations, and apply the right magnetic field.

Recommended resources

There are many excellent resources available for the reader interested in learning more about rare-earths. For a rigorous introduction to REI spectroscopy, see the texts from two heroes of the field: Wybourne (1965) [20] and Dieke (1968) [18]. Hufner (1978) [21] is a good resource with worked examples of applying group theory to understand REI spectra. Powell (2010) is a more general group theory reference that is useful in this context. The compilation by Jaquier and Liu (2005) [22] is a nice compilation with the chapter by Reid recommended for those interested in learning more about crystal field theory in action and calculating transition strengths. Abragam and Bleaney (1970) [23] is the go-to for those interested in the spin Hamiltonian approach. Schweiger and Jeschke (2001) [24] is recommended to those looking for a more modern reference. Macfarlane and Kaplianksii have a useful compilation (1987), with the chapter by Macfarlane and Shelby [25] covering many of the spectroscopic tools used with rare-earth ensembles. In general, I recommend the work of Cone (and his students/coworkers) or Macfarlane as a good place to start for those interested in rare-earth spectroscopy. They have worked with basically everybody (and every REI crystal imaginable) in the field over the years and will at least set you down the right path.

1.3 What's been done with the rare-earth ions?

As a result of their long optical and spin coherence lifetimes, the dominant application of rare-earth ions to quantum technologies has been in the form of optical quantum memories. Quantum memories are essential components for quantum networks where they can be used to synchronize probabilistic events, for instance in quantum

repeater protocols for entanglement generation across a network. These memories rely on ensembles of rare-earth ions and are inspired by "photon echo" techniques that enable the reversible transfer of a quantum state of light to a collective atomic excitation. These protocols usually make use of the inhomogeneous distribution of the ensemble that is either statically structured or dynamically altered to control the absorption and subsequent re-emission of light. This field has rapidly evolved in the past ten years and there have been a variety of different protocols implemented with a wide range of host crystals. This has included demonstration of memories with high efficiencies (up to 69%) [26–28], long storage times (> 1 ms) [29, 30], and multimode storage capacity [30–32]. Importantly, these memories have also allowed for storage of quantum states of light [33] and preservation of entanglement [30, 34]. For relatively recent review articles, see [35–37]

Another growing application of rare-earth ions is in microwave-to-optical transduction of quantum states following the proposal by Williamson et al. [38] and O'Brien et al. [39] in 2014. Such transducers will find utility in establishing entanglement between the microwave and optical domains, i.e., linking superconducting circuits via optical photons. There have been initial demonstrations toward this goal [40, 41], but there is still a lot of work to be done in this direction.

Detection and manipulation of single rare-earth ions is a rapidly expanding line of research. The first definitive observation of a single rare-earth ion was in Pr:YAG nanocrystals by Kolesov et al in 2012 [42]. This work used an optical upconversion to a $4f5d$ state to take advantage of the short optical lifetime of this state. The use of nanocrystals allowed for spatial isolation of individual ions. Further demonstrations have followed relying on similar approaches. For example, resolved hyperfine splitting in Pr:YSO has been observed with the use of nanocrystals and solid-immersion lenses to enhance the photon collection efficiency [43, 44]. Following work showed microwave manipulation [45] and coherent population trapping [46] with single cerium ions in YAG along with ODMR of single ions in Pr:YAG [47]. These works have also demonstrated techniques for single ion implantation [45, 46, 48, 49]. In 2018, the first detection of single rare-earth ions coupled to a nanophotonic resonator was shown in Nd:YVO by our group [4] and in Er:YSO by the Thompson group [50].

The goal in the Faraon group has been to integrate rare-earth ions with nanophotonics to enable efficient and scalable interfaces with applications to all of the the technologies mentioned above. Early work in neodymium focused on building

nanoscale quantum memories and there are ongoing efforts to build optical quantum memories with erbium for operation at telecom wavelengths. Another project in the group is pursuing microwave-to-optical transduction, first with demonstrations in ^{171}Yb:YVO_4 and plans to move to telecom wavelengths. This thesis will focus on the efforts toward detection and manipulation of single ions in ^{171}Yb:YVO_4 .

1.4 Photonic crystal cavities fabricated in rare-earth ion hosts

Many of the demonstrations in the Faraon group over the past few years have used photonic crystal cavities fabricated directly in the host material using focused ion beam (FIB) milling[3]. One such device is shown in Fig. 1.1. These devices were initially designed and fabricated by one of the former postdocs in the lab, Dr. Tian Zhong, with further optimization and fabrication in YVO taken over by graduate student Jake Rochman.[4] The fabrication process is detailed in [53] and further details can be found in Evan Miyazono's thesis [51]. The fabrication process is briefly summarized as follows: a triangular nanobeam is fabricated in the surface of the host crystal using the focused ion beam. Periodic trenches are made in this material to form a photonic band gap with the spacing of these cuts tapered in the middle to form the cavity mode. Light is coupled into and out of these devices via total internal reflection using 45 degree couplers fabricated on both sides of the device.

For early measurements in these devices, we were typically working in transmission through "two-sided" devices where both sides of the cavity are designed to have equal reflectivity. Most devices made these days are measured in reflection and are "one-sided" devices in which the reflectivity of one side of the cavity is lowered by reducing the number of photonic crystal lattice periods to allow for more efficient coupling into the collection path.

The best quality factors we have achieved in these devices are up to 7×10^4 at 1536 nm in Er:YSO. At neodymium wavelengths ($\sim$ 880 nm), the best devices have given $Q \sim 2.5 \times 10^4$. For the devices in YVO, simulations of these designs give mode volumes of $\sim 1(\lambda/n)^3$ (n is the refractive index of YVO) and quality factors $\sim 10^6$. The resonances of the fabricated devices are usually within $5 - 10$ nm of the design wavelength. Tuning of the resonance wavelength of the cavities onto the optical transition of the rare-earth ion of interest is accomplished at cryogenic

[3] See [51] and [52] for details of a hybrid fabrication architecture that has also been pursued in the Faraon group.

[4] I cannot sufficiently express my gratitude for their fabrication efforts!

temperatures by depositing solid nitrogen to change the effective refractive index of the cavity mode [54].

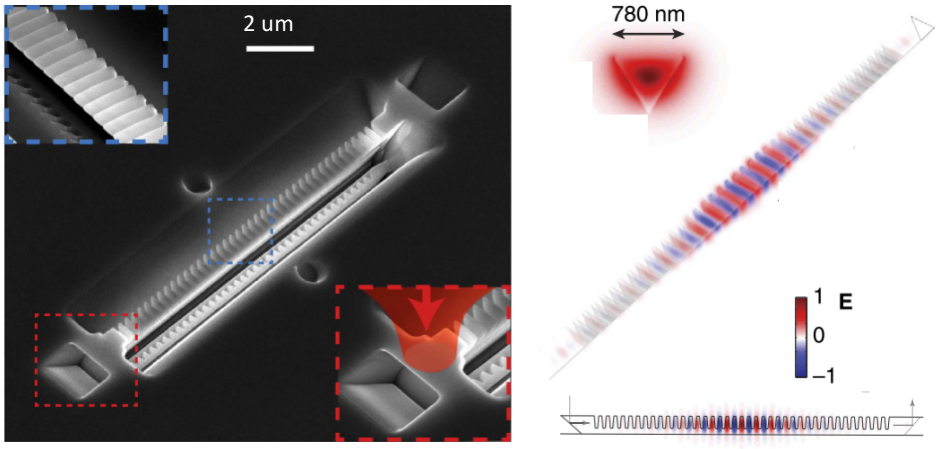

Figure 1.1: Example of the photonic crystal nanobeam resonators used in the Faraon group. The left is a scanning electron microscope image of a device fabricated in Nd:YSO and used for the work in [1]. Blue inset shows the trenches forming the photonic crystal. The red inset shows coupling into and out of the device through 45° cuts at the end of the device. The right shows further schematics of this particular device with the simulated electric field of the fundamental TE resonance.

Chapter 2

NANOPHOTONIC INTERFACES IN ND:YSO AND ND:YVO

In this chapter, I will summarize the work that was the focus of my first few years at Caltech. The goal of this chapter is to give a brief history of the measurements in the triangular nanobeam platform and contextualize the single ion work in ^{171}Yb:YVO_4. I will not discuss experiments in detail and instead refer the interested reader to the corresponding publications and supplementary materials. The results discussed here are published in [1–4, 53, 55]

2.1 Preservation of optical coherence in nanocavities

The first major goal of the research program in the Faraon group was to demonstrate coupling between rare-earth ions and a nanophotonic resonator and, crucially, to investigate whether the coherence properties of the rare-earth ions were degraded inside this nanophotonic device.

We achieved this goal by demonstrating coupling of an ensemble of neodymium atoms to a triangular nanobeam cavity fabricated in the yttrium orthosilicate (YSO) host crystal. This work is detailed in [1] with highlights shown in Fig. 2.1. The optical cavity used for this demonstration had a Q of 4,400 and simulated mode volume of $V \approx 1.65(\lambda/n)^3$. In this device, an enhancement of photoluminescence of the ions in the cavity was observed as the cavity was tuned onto resonance with the optical transition. Purcell-enhanced emission of the cavity-coupled ions was demonstrated with a reduction in the ion lifetime from 254 μs in bulk to 87 μs in the cavity (Fig. 2.1a). Taking into account the modest branching ratio of Nd in YSO (4.5 %), this corresponds to an averaged Purcell enhancement on the resonant transition of 42. In higher doping samples, we also directly showed that the ensemble of ions modifies the transmission spectra of the cavity.

Following the demonstration of cavity-coupling, the next major question was whether the coherence properties of the ions were preserved through the fabrication process. The coherence lifetimes of the ensemble of cavity-coupled ions was measured using photon echoes and we found no degradation from what was observed in the bulk material (Fig. 2.1c). Further, the inhomogeneous broadening of the ensemble was preserved in the device. Lastly, we observed statistical fine structure (SFS) on the

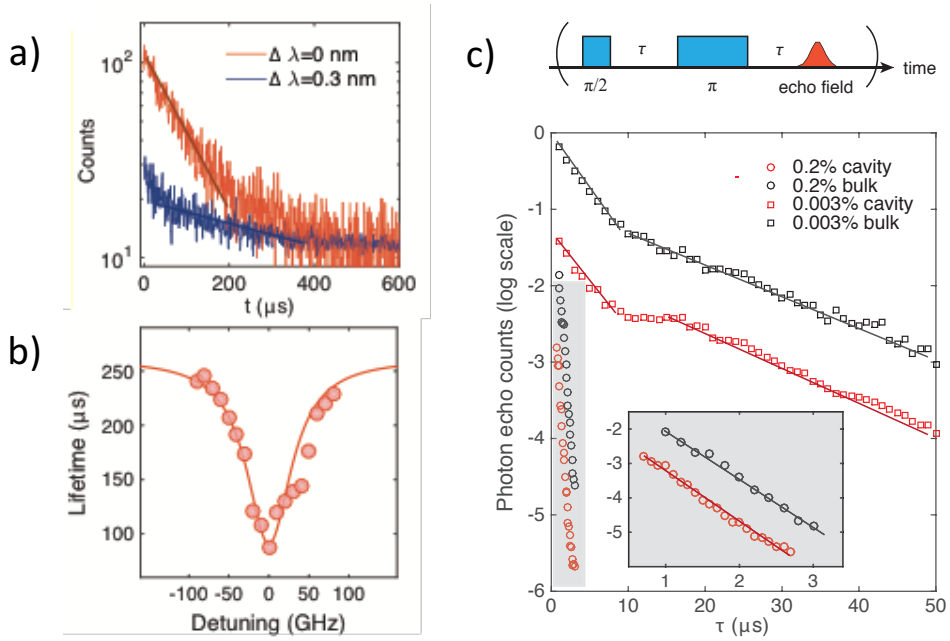

Figure 2.1: Highlights from [1]. a) Lifetime measurement of cavity-coupled ions with cavity on resonance (red) and detuned (blue) showing lifetime reduction from 254 μs to 87 μs. b) Measurement of Purcell enhancement as a function of detuning. c) Preservation of optical coherence lifetimes in cavity-coupled ensembles. Coherence is measured with photon echoes in two different doping densities and compared to the coherence lifetimes in bulk.

cavity transmission due to the coupling to the ions, which was an important step on the path to single ion detection

This was a significant first result for us in that it showed a path forward for this platform. If we had instead found that the coherence properties were rubbish after fabrication, I would probably be writing a very different thesis right now! Much of this initial time was spent developing the fabrication process for the nanobeam cavities and building up the measurement infrastructure and techniques in a new lab.

Following this initial result, the work shifted from Nd:YSO to Nd in yttrium orthovanadate (YVO). This allowed us to take advantage of the significantly stronger optical transitions available in this material. Increased fabrication efforts enabled higher quality factors in the resulting devices in YVO. Details on the development of the nanobeam resonators can be found in [53].

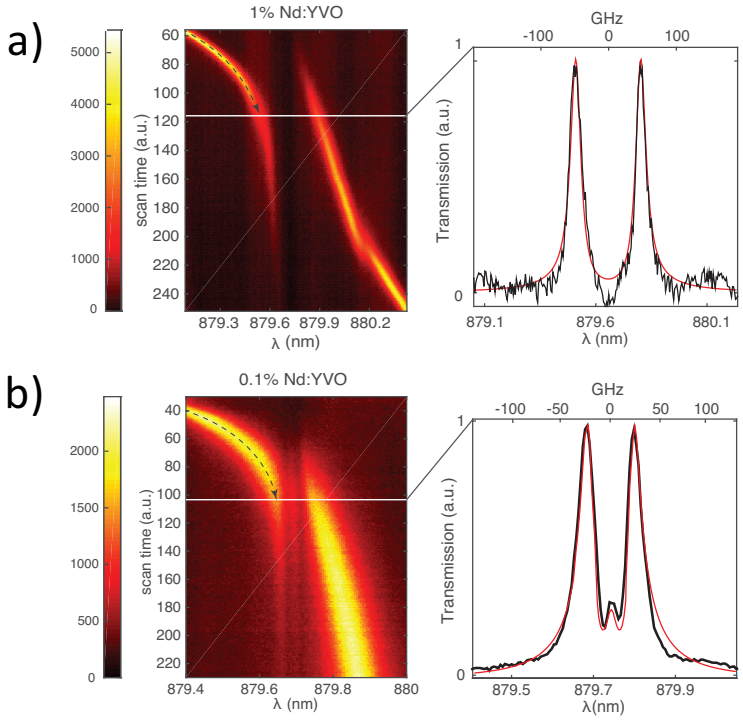

Figure 2.2: Highlight from [2] showing collective strong coupling of a Nd ensemble to YVO nanobeams fabricated in a) 1% and b) 0.2 % Nd:YVO. These plots show cavity transmission spectra as the cavities are tuned through the Nd optical transition at 879.7 nm.

2.2 Ensemble strong coupling

With the improved devices in Nd:YVO, the next result was demonstrating collective strong coupling of a cavity to an ensemble of ions. This work is detailed in [2] with representative results shown in Fig. 2.2. In this system, we demonstrated a phenomenon called cavity protection through which the coherence of the inhomogeneous ensemble can be suppressed through collective coupling to the cavity [56]. This technique had been demonstrated in the microwave domain with an NV spin ensemble [57, 58], but had not been demonstrated in the optical domain. This work also complimented the work of other groups demonstrating collective coupling of rare-earths to superconducting resonators in the microwave regime [59]. We showed that this effect could be used to store and retrieve frequency bin qubits in the collective ensemble excitation with high bandwidth ($\sim$ 50 GHz) and high retrieval fidelity (98.7%).

While this regime was not explored further, it allowed us to demonstrate interesting

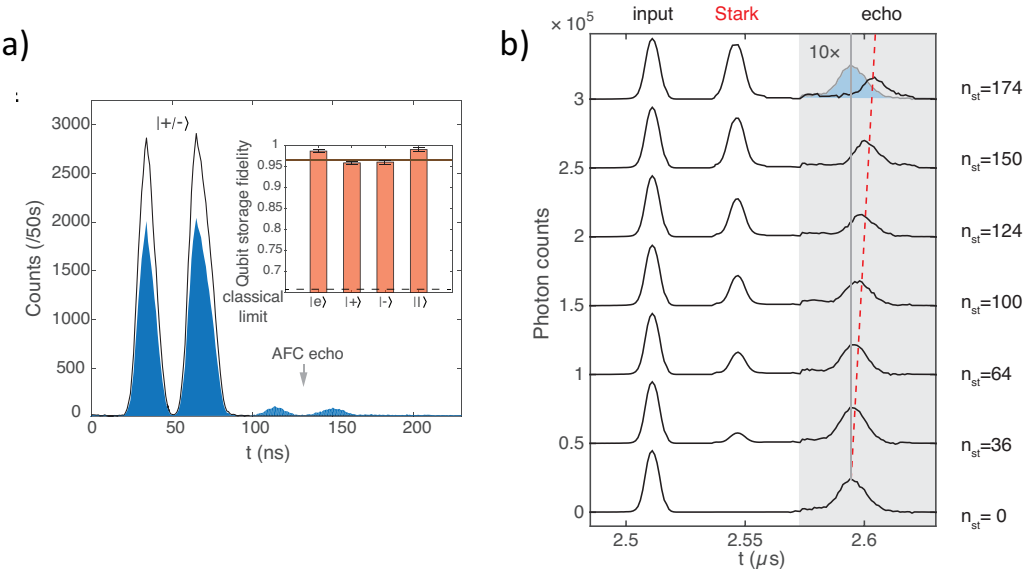

Figure 2.3: Highlights from [3]. a) Demonstration of atomic frequency comb storage in Nd:YVO nanocavity. A time-bin qubit is stored for 75 ns. The extracted fidelity for different input states with extracted storage fidelities > 95%. b) Demonstration of temporal shifting of AFC echoes using the cavity-enhanced AC stark shift.

REI physics in these devices. This demonstration of strong-coupling also brought us closer to the impedance-matched ensemble coupling necessary for the quantum memory work

2.3 Nanophotonic quantum memory

The next big result was the demonstration of a nanophotonic quantum memory using an ensemble of neodymium ions coupled to a YVO nanobeam cavity. These results are detailed in [3] with highlights shown Fig. 2.3.

The first step toward this goal was confirming that optical coherence was still preserved in the Nd:YVO devices. We then demonstrated that the Purcell enhancement could be used to enhance optical pumping between the Zeeman split ground states of Nd:YVO. With the ability to perform coherent optical measurements and initialize the spin state, we then implemented an atomic frequency comb (AFC) memory with the cavity coupled ensemble. We demonstrated modest storage times of $\sim$ 100 ns and device efficiencies of 2.5%, but more importantly showed that this device allowed for high-fidelity ($\sim$ 97%) storage at the single photon level. Furthermore, we demonstrated that the high Rabi frequencies in the cavity enabled a novel

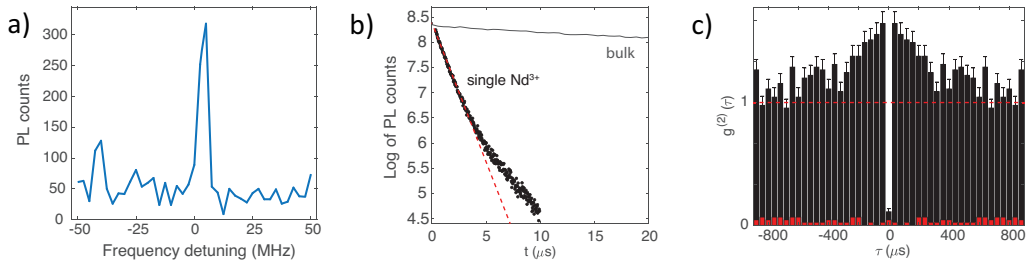

Figure 2.4: Highlights from [4]. a) PLE scan over isolated single Nd ion coupled to a YVO nanocavity. b) Purcell enhancement of single Nd ion showing lifetime of 2.3 μs compared to bulk lifetime of 90 μs. c) Second-order photon correlation measurement on emission from single Nd ion showing $g^{(2)}[0] = 0.09$.

method based on the cavity-enhanced AC stark shift that could be used to dynamically tune the shape of the atomic frequency comb during storage. This gave us the ability to shift the recall time of the otherwise fixed delay AFC protocol (Fig. 2.3b).

This work was followed with a more thorough investigation of the AC Stark shift in the ensemble, the results of which are published in [55]. Alongside and building upon this work, efforts of other members in the group have been focused on similar research in erbium-doped materials for ensemble based memories at telecom wavelengths. In these devices, they have demonstrated coupling to ions in Er:YSO in both a hybrid platform based on amorphous silicon [52] and the nanobeam platform [60]. Recently, AFC storage with high fidelity and improved storage times has been demonstrated in an Er:YSO nanobeam (publication in review).

2.4 Detection of single ions

After demonstrating an ensemble-based quantum memory, the focus then shifted to detection and manipulation of single ions in these cavities. In the same device as was used for the quantum memory work, we demonstrated optical detection of single Nd ions in YVO. Furthermore, we were able to demonstrate coherent control pulses on the optical transition and show that the Purcell-enhancement in cavity could be used to approach lifetime-limited optical coherence. This work is described in [4] with highlights shown in Fig. 2.4.

2.5 Toward coherent spin control

Building on all this work, the next big goal was coherent control of single REI spins. The electron spin transitions of Nd:YVO are known to have short coherence

lifetimes, so we were primarily interested in exploring nuclear spins. One option for working with nuclear spins would be using Nd-145 in YVO. The big disadvantage here is that the nuclear spin of this isotope is 7/2, which means that in a magnetic field there are 16 levels in both the ground and excited state. This leads to a forest of transitions that are closely spaced or overlapping, which was not an especially attractive option.

After wrapping up the quantum memory work, we started to look into the properties of ^{171}Yb:YVO_4 . While this material had not been explored in the context of quantum applications, the 171 isotope of ytterbium was especially intriguing, as it offered the simplest possible energy structure one could ask for with both electron and nuclear spin 1/2. As the optical transitions were within the reach of our Ti:Sapph laser and the rest of the optical setup, we decided to have a boule of ^{171}Yb:YVO_4 grown for us and see for ourselves whether this material might be useful. The rest of this thesis tells the story of ^{171}Yb:YVO_4 from there.

Chapter 3

SPECTROSCOPY OF ^{171}YB:YVO_4

This chapter presents the characterization of ^{171}Yb:YVO_4 with focus on its suitability for nanophotonic quantum technologies. The results presented in this chapter are published in [61].

3.1 Introduction

Rare-earth ions (REIs) doped into crystalline hosts have demonstrated significant progress in implementing solid-state quantum technologies. REIs possess some of the longest optical and spin coherence lifetimes in the solid state [62–65], which has provided the foundation for numerous demonstrations of quantum memories and quantum interfaces [26, 27, 33, 66–68]. For interfaces involving both microwave and optical photons, REIs with an odd number of electrons (i.e. Kramers ions), such as erbium, neodymium, and ytterbium, are of interest due to their electron spin transitions. The large magnetic moments of these ions allow for strong interactions with microwaves, enabling fast operations and the potential for interfacing with superconducting qubits. Isotopes of these ions with non-zero nuclear spin also offer the possibility of long-term quantum storage [65]. This combination of properties creates the potential for building interfaces between microwave photons, optical photons, and long-lived nuclear spins.

Among the Kramers ions, ytterbium is an attractive choice due to its simple level structure consisting of only two electronic multiplets. The optical transition between the lowest energy levels of these multiplets occurs around 980 nm, which is readily accessible by standard diode lasers. Furthermore, the $^{171}Yb^{3+}$ isotope is unique among the trivalent REIs as the only Kramers ion with a nuclear spin of 1/2. This gives the simplest possible hyperfine energy structure with both electron and nuclear spin degrees of freedom, which reduces the complexity of optical preparation and manipulation of spin states [69, 70]. Recent work in ^{171}Yb:Y_2SiO_5 [71–74], Yb^{3+}:$LiNbO_3$ [75], and Yb^{3+}:YAG [76] highlights the interest in this ion. In this work, we investigate $^{171}Yb^{3+}$ doped into the host crystal YVO_4. YVO_4 is an attractive choice for implementing quantum interfaces [3, 77] due to the ability to fabricate nanoscale devices [53] and high site symmetry in this material. Furthermore, previous work points to the potential for high oscillator strength transitions

for Yb^{3+} doped into YVO_4 [78].

In this chapter, we present an initial survey of the properties of optical and nuclear spin transitions in ^{171}Yb:YVO_4 at cryogenic temperatures. To determine whether this material can be used for efficient interactions with light, we characterized the strength and inhomogeneity of the optical transitions using high-resolution optical spectroscopy. Large hyperfine couplings and narrow optical inhomogeneous lines in this material result in resolved optical transitions between the hyperfine states, which allowed for characterization of the excited-state spin Hamiltonian directly from absorption measurements in an applied magnetic field. Knowledge of the spin Hamiltonian enables the identification of magnetic field orientations that create strongly spin-conserving transitions (for cyclic transitions) or strongly spin-mixing optical transitions (allowing for efficient lambda systems). To assess the possibility of storage and manipulation of quantum information in this material, we measured the coherence properties of the optical and nuclear spin transitions as a function of applied magnetic field. To demonstrate the potential for all-optical control of the nuclear spin states, we also measured spin echoes using bichromatic Raman pulses.

This chapter is organized as follows: Section 3.2 presents the material properties of the samples used in this work and the spin Hamiltonian used to model this system. Section 3.3 describes the experimental methods and apparatus. Section 3.4 presents the experimental results and discussion. This section is further divided into subsections: A (Optical absorption spectroscopy), B (Optical transition strengths), C (Excited-state lifetime), D (Optical coherence measurements), E (Nuclear spin measurements), and F (All-optical spin coherence measurements).

3.2 Background

Material properties

YVO_4 (also called yttrium orthovanadate or YVO) forms a zircon tetragonal crystal with D_{4h} symmetry [79]. Ytterbium substitutes for yttrium in sites of local D_{2d} point group symmetry. The z-axis of the site coincides with the crystalline 4-fold axis (the c-axis of the crystal). The uniaxial nature of this site reduces the number of parameters needed to characterize the system compared to a lower symmetry crystal such as Y_2SiO_5 [71, 72].

The majority of measurements presented in this paper were performed in samples cut from a boule of YVO_4 doped with isotopically enriched $^{171}Yb^{3+}$ custom grown by Gamdan Optics. The concentration of ^{171}Yb was measured to be 100 ppm using

secondary ion mass spectrometry (SIMS). The samples were cut and polished to various thicknesses appropriate to each measurement. Fluorescence lifetime measurements were performed using a nominally undoped sample of YVO_4 (Gamdan Optics), which was measured using SIMS to have a residual $^{171}Yb^{3+}$ concentration of approximately 2 ppm.

Spin Hamiltonian

The $4f^{13}$ configuration of Yb^{3+} consists of two electronic multiplets: $^2F_{7/2}$ and $^2F_{5/2}$. In the crystal field of YVO_4, the ground-state multiplet ($^2F_{7/2}$) splits into four Kramers doublets and the excited-state multiplet ($^2F_{5/2}$) splits into three Kramers doublets. The energies of these crystal-field levels have been measured previously [80] and are shown in Fig. 3.1. At liquid helium temperatures, only the lowest energy doublet of the ground state is thermally occupied. The optical transition of interest for quantum interfaces is between the lowest energy doublets of the ground state and excited state ($^2F_{7/2}(0) \rightarrow {}^2F_{5/2}(0)$). This transition occurs at approximately 984.5 nm for Yb^{3+} doped into YVO_4.

In this work, we focus on the ^{171}Yb isotope, which has a nuclear spin $I = 1/2$. Treating the Kramers doublets as effective spins with $S = 1/2$, we can describe the system with the following spin Hamiltonian [23]:

$$H_{\text{eff}} = \mu_B \mathbf{B} \cdot \mathbf{g} \cdot \mathbf{S} + \mathbf{I} \cdot \mathbf{A} \cdot \mathbf{S} - \mu_n \mathbf{B} \cdot \mathbf{g_n} \cdot \mathbf{I}. \tag{3.1}$$

The first term is due to the electronic Zeeman interaction, where μ_B is the Bohr magneton, $\mathbf{B}$ is the applied magnetic field, $\mathbf{g}$ is the electronic Zeeman tensor, and $\mathbf{S}$ is the spin 1/2 operator. The second term describes the coupling between the electron spin and nuclear spin via the hyperfine interaction, where $\mathbf{I}$ is the nuclear spin operator and $\mathbf{A}$ is the hyperfine interaction tensor. The last term arises from the nuclear Zeeman interaction, where μ_n is the nuclear magneton and $\mathbf{g_n}$ is the nuclear Zeeman tensor. For ^{171}Yb in YVO_4, the non-zero components of $\mathbf{g_n}$ will be of the order of the gyromagnetic moment of the free nucleus $g_n = 0.987$, which leads to a nuclear Zeeman interaction ~ 2000 times smaller than the electronic Zeeman term. For the magnetic field values used in this work, we treat this interaction by incorporating it into the electronic Zeeman tensor.

The energy structure in the absence of an external magnetic field ($\mathbf{B} = 0$) is determined by the hyperfine interaction $\mathbf{I} \cdot \mathbf{A} \cdot \mathbf{S}$. In the site symmetry of YVO_4, the degeneracy of these levels is partially lifted and the Hamiltonian has the following

eigenvalues at zero field: $E = \frac{A_\parallel}{4}, \frac{A_\parallel}{4}, \frac{-A_\parallel+2A_\perp}{4}, \frac{-A_\parallel-2A_\perp}{4}$, where $A_\perp$ and $A_\parallel$ are the components of the hyperfine tensor $\mathbf{A}$ perpendicular and parallel to the crystal symmetry axis (the c-axis) [23]. The order of the energies is determined by the signs of these components, which we have determined to be $A_\parallel^g < 0$ and $A_\perp^g, A_\parallel^e, A_\perp^e > 0$ (see Section 3.4) with the superscript g (e) denoting the ground (excited) state. The corresponding eigenstates numbered from lowest to highest energy are

$$|1\rangle_g = |\uparrow\Uparrow\rangle_g \qquad |1\rangle_e = \frac{1}{\sqrt{2}}\left(|\uparrow\Downarrow\rangle_e - |\downarrow\Uparrow\rangle_e\right) \tag{3.2}$$

$$|2\rangle_g = |\downarrow\Downarrow\rangle_g \qquad |2\rangle_e = \frac{1}{\sqrt{2}}\left(|\uparrow\Downarrow\rangle_e + |\downarrow\Uparrow\rangle_e\right) \tag{3.3}$$

$$|3\rangle_g = \frac{1}{\sqrt{2}}\left(|\uparrow\Downarrow\rangle_g - |\downarrow\Uparrow\rangle_g\right) \qquad |3\rangle_e = |\uparrow\Uparrow\rangle_e \tag{3.4}$$

$$|4\rangle_g = \frac{1}{\sqrt{2}}\left(|\uparrow\Downarrow\rangle_g + |\downarrow\Uparrow\rangle_g\right) \qquad |4\rangle_e = |\downarrow\Downarrow\rangle_e\,. \tag{3.5}$$

We denote the electron spin components as $|\uparrow\rangle \equiv \left|S_z = \frac{1}{2}\right\rangle$, $|\downarrow\rangle \equiv \left|S_z = -\frac{1}{2}\right\rangle$ and the nuclear spin components as $|\Uparrow\rangle \equiv \left|I_z = \frac{1}{2}\right\rangle$, $|\Downarrow\rangle \equiv \left|I_z = -\frac{1}{2}\right\rangle$.

For high magnetic fields applied along the c-axis, the electronic Zeeman interaction dominates over the hyperfine interaction. In this regime, mixing between the electron and nuclear spin is greatly reduced and the states effectively become

$$|1'\rangle_g \approx |\uparrow\Uparrow\rangle \qquad |1'\rangle_e \approx |\downarrow\Uparrow\rangle \tag{3.6}$$

$$|2'\rangle_g \approx |\uparrow\Downarrow\rangle \qquad |2'\rangle_e \approx |\downarrow\Downarrow\rangle \tag{3.7}$$

$$|3'\rangle_g \approx |\downarrow\Downarrow\rangle \qquad |3'\rangle_e \approx |\uparrow\Downarrow\rangle \tag{3.8}$$

$$|4'\rangle_g \approx |\downarrow\Uparrow\rangle \qquad |4'\rangle_e \approx |\uparrow\Uparrow\rangle\,. \tag{3.9}$$

We have again numbered the states from lowest to highest energy using the fact that $g_\parallel < 0$ for the ground state and $g_\parallel > 0$ for the excited state (see Section 3.4). The prime is used to distinguish between the high field and zero field state labels. In this work, we focus on the coherence properties of the optical and nuclear spin transitions in the regime where the linear Zeeman interaction is dominant.

3.3 Experimental Methods

High-resolution laser absorption scans with a home-built external-cavity diode laser (ECDL) using the design from [82] were performed to measure the inhomogeneous linewidth and absorption of the ${}^2F_{7/2}(0) \rightarrow {}^2F_{5/2}(0)$ transition. The energies of the optical transitions were extracted from absorption scans taken with magnetic

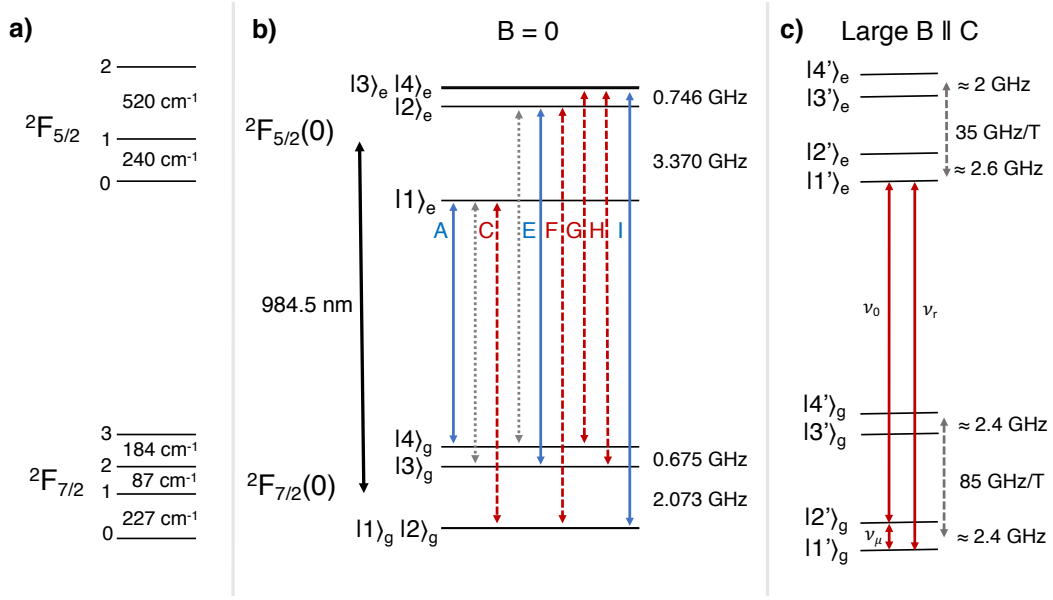

Figure 3.1: Energy level diagram for ^{171}Yb:YVO$_4$. a) Crystal field splittings of ^{171}Yb:YVO$_4$ reproduced from [80]. b) Zero-field energy level diagram for the $^2F_{7/2}(0) \rightarrow {}^2F_{5/2}(0)$ transition of ^{171}Yb:YVO$_4$ at 984.5 nm studied in this paper. Energy splittings in the ground and excited state are extracted from the excited-state hyperfine tensor determined in this work and previous measurements of the ground-state hyperfine tensor [81]. The transitions corresponding to the observed absorption spectrum in Fig. 3.2 for $E \parallel c$ ($E \perp$ c) are shown in solid blue (dashed red). The dotted grey lines correspond to transitions that are forbidden by symmetry. c) Energy level diagram for the linear Zeeman regime with $B \parallel c$ with arrows denoting the transitions studied in this work.

fields applied along the crystal symmetry axes and used to determine the excited-state spin Hamiltonian. For this purpose, we used a 90 μm thick a-cut sample of ^{171}Yb:YVO$_4$. This thickness was chosen such that the sample was not overabsorbing at 2 K. The sample was mounted in a custom sample mount and masked to avoid spurious light leakage around the crystal that could lead to inaccurate measurements of the optical depth. For the data presented here, the probe light propagated parallel to the a-axis of the crystal and perpendicular to the applied magnetic field ($\mathbf{k} \perp \mathbf{B}, c$). Additional axial spectra ($\mathbf{k} \parallel c$) were taken to confirm the electric dipole nature of the optical transitions [22]. The absorption was determined by measuring the transmission of the ECDL on a photodetector (New Focus 2031) as the frequency of the laser was scanned across resonance. The center frequency of the scan was calibrated with a wavemeter (Burleigh WA-1500) and the frequency detuning of the scan was calibrated using a Fabry-Perot reference cavity. The absorption ex-

periments were performed in an Oxford Spectromag cryostat at a temperature of 2 K with an applied magnetic field of up to 6 T.

For measurements of the excited-state, optical coherence, and spin coherence lifetimes, the optical transitions were addressed using a single frequency Ti:Sapphire laser (M-Squared Solstis) that was gated by an 80 MHz acousto-optic modulator in a double-pass configuration to create the required pulse sequence. For measurements of the coherence properties and inhomogeneity of the nuclear spin transition, the nuclear spin transition was addressed directly using a coaxial transmission line mounted directly next to the sample.

The excited-state lifetime was measured from the time-resolved fluorescence decay. We performed pulsed excitation on the ${}^2F_{7/2}(0) \rightarrow {}^2F_{5/2}(0)$ transition and collected the resulting fluorescence to the upper crystal field levels of the ground state (i.e. ${}^2F_{5/2}(0) \rightarrow {}^2F_{7/2}(1-3)$) using a 1000 nm long-pass filter. The fluorescence counts as a function of time were recorded using a silicon APD (Perkin-Elmer). Fluorescence measurements were performed in a 500 μm thick sample that was nominally undoped (residual ${}^{171}Yb^{3+}$ concentration of $\sim$ 2 ppm) and a 200 μm thick 100 ppm sample of ${}^{171}Yb{:}YVO_4$. These measurements were performed at 4 K with zero applied magnetic field in a Montana Instruments cryostat using a home-built confocal microscope setup.

The coherence properties of the optical transition were investigated using two-pulse photon echo decays as a function of magnetic field strength. For this purpose, two-pulse photon echoes on the $|1'\rangle_g \rightarrow |1'\rangle_e$ transition were measured using heterodyne detection. During the echo sequence, a fiber-based phase modulator EOM (IXBlue NIR-MPX-LN-20) was driven by a microwave source (Windfreak Synth HD) at 500 MHz to create an optical sideband resonant with the optical transition. The resulting echo was detected as a beat at the sideband frequency using an InGaAs photodiode (Thorlabs DET08CFC, BW = 5 GHz). Typical π-pulses for this measurement were 4 μs long.

Optical coherence measurements were performed with the sample mounted on the still plate of a Bluefors dilution refrigerator at a temperature of 650 mK. These measurements used a 500 μm thick c-cut 100 ppm sample with $\mathbf{k} \parallel c$. The light entered the refrigerator via single-mode optical fiber and was focused onto the back surface of the sample, which was coated in gold to enhance reflection. The reflected light was coupled back into the fiber and directed to the photodetector with a fiber beam splitter. A variable magnetic field of up to 1.5 T was applied along the crystal

c-axis using a homebuilt superconducting solenoid.

The inhomogeneous linewidth of the nuclear spin transition was measured using continuous-wave Raman heterodyne detection [83]. Frequency-swept microwave tones from a tracking generator (Anritsu) were amplified and applied to the sample. The coherence generated on the $|1'\rangle_g \rightarrow |2'\rangle_g$ nuclear spin transition was mapped to an optical coherence by applying a continuous wave laser to the $|2'\rangle_g \rightarrow |1'\rangle_e$ optical transition at frequency ν_0, which resulted in coherent Raman scattering on the $|1'\rangle_g \rightarrow |1'\rangle_e$ optical transition at ν_r. This signal was detected on the transmitted optical beam as a beat at the microwave transition frequency $(\nu_0 - \nu_r)$ using an InGaAs photodiode.

The nuclear spin coherence was measured using two-pulse spin echoes. Coherent manipulation on the nuclear spin state was performed with both direct microwave excitation and all-optical excitation with bichromatic Raman pulses [84–87]. The ions were first initialized into the $|1'\rangle_g$ state via optical pumping on the $|2'\rangle_g \rightarrow |1'\rangle_e$ transition. For direct manipulation, the echo sequence was performed using tones generated by a microwave source tuned to the $|1'\rangle_g \rightarrow |2'\rangle_g$ nuclear spin transition. Pulses were generated using microwave switches (Minicircuits ZASWA-2-50DR+) with typical π pulse lengths of 100 μs. For all-optical spin echoes, the nuclear spin transition was coherently manipulated via the shared excited state $|1'\rangle_e$ by applying bichromatic pulses to the $|2'\rangle_g \rightarrow |1'\rangle_e$ and $|1'\rangle_g \rightarrow |1'\rangle_e$ transitions as depicted in Fig. 3.1c. Typical spin π pulses for the all-optical sequence were 8 μs. The two optical frequencies were generated by driving a fiber-based phase modulator with a microwave source tuned to the nuclear spin transition frequency. The relative power of the two optical frequencies was chosen to maximize the echo signal. The resulting spin echo was optically detected via Raman heterodyne scattering by applying a readout pulse to the $|2'\rangle_g \rightarrow |1'\rangle_e$ transition at the time of the echo. The signal was detected as a beat on the probe laser at the nuclear spin transition frequency.

Nuclear spin coherence measurements were performed at approximately 700 mK. These measurements were done in transmission through a 2 mm thick a-cut sample with $\mathbf{k} \perp c, \mathbf{B}$. The polarization of the input light was set using a fiber polarization controller to maximize the echo signal. A variable magnetic field was applied to the crystal using a set of homebuilt superconducting Helmholtz coils. For the direct microwave measurements, the magnetic field was applied along the c-axis. For the all-optical measurements, the magnetic field was applied $\sim 20^\circ$ from the c-axis. As

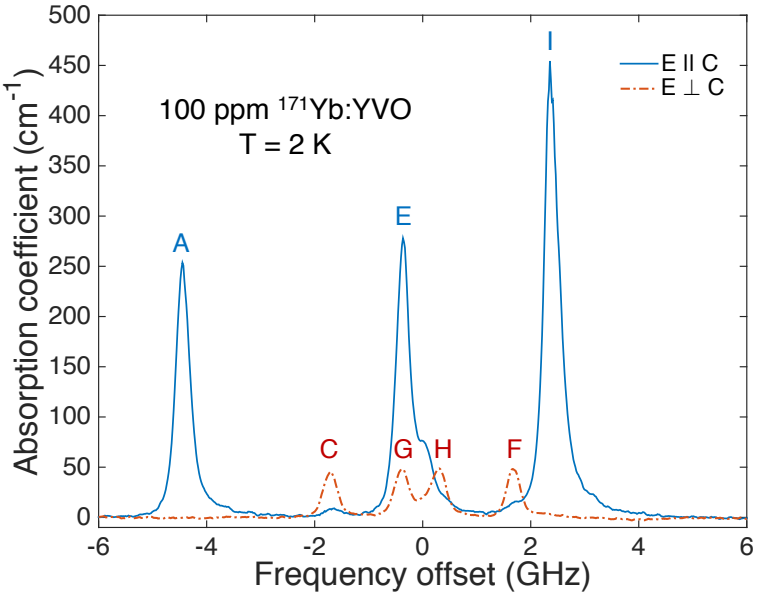

Figure 3.2: Optical absorption spectra of the ${}^2F_{7/2}(0) \rightarrow {}^2F_{5/2}(0)$ transition of ^{171}Yb:YVO_4 at 2 K and zero applied magnetic field for light polarized parallel (solid blue) and perpendicular (dashed red) to the crystal c-axis.

described in Section 3.4, this was done to help equalize the strengths of the optical transitions used in the measurement.

3.4 Optical and spin properties of ^{171}Yb:YVO_4

Optical absorption spectroscopy

The zero-field absorption spectra for the ${}^2F_{7/2}(0) \rightarrow {}^2F_{5/2}(0)$ transition of ^{171}Yb:YVO_4 at 2 K is shown in Fig. 3.2. We observed narrow inhomogeneous linewidths (average FWHM = 275 MHz), which allowed us to resolve and address individual optical-hyperfine transitions. For $\mathbf{E} \parallel c$, we observed three resolved transitions with a peak absorption coefficient for the strongest transition of 450 cm^{-1}. For $\mathbf{E} \perp c$, we observed four resolved transitions with a peak absorption of 50 cm^{-1}. The corresponding transitions on the energy diagram are labeled in Fig. 3.1. The strong polarization selection rules between the optical hyperfine transitions observed in Fig. 3.2 are consistent with those derived for electric-dipole transitions based on the site's point group symmetry [5]. [1]

We observed a peak at zero detuning, which corresponds to the presence of zero

[1] See appendix A for further details.

spin isotope in the sample (measured to be < 10 ppm from SIMS). We also noted the presence of additional satellite lines due to the 173 isotope.

The ground state Zeeman and hyperfine tensors of ^{171}Yb:YVO_4 have been determined using EPR [81], so a description of the system requires finding the corresponding values for the excited state. For a uniaxial crystal, this reduces to four parameters: the components of **g** and **A**, parallel and perpendicular to the crystal symmetry axis. The values for **A** can be determined by the energy level structure in the absence of a magnetic field, while **g** can be determined from the energy level structure as magnetic fields are applied parallel and perpendicular to the crystal's c-axis.

Fitting to the energy level splittings extracted from the absorption spectra, we find agreement with previously published data for the ground-state **A** tensor [81] ($A^g_\parallel/h = -4.82$ GHz, $A^g_\perp/h = 0.675$ GHz) and we determine the principal values of the excited-state hyperfine tensor to be $A^e_\parallel/h = 4.86 \pm 0.05$ GHz and $A^e_\perp/h = 3.37 \pm 0.05$ GHz.

The excited-state **g** tensor was determined by measuring the frequency of the optical transitions with magnetic fields applied parallel and perpendicular to the crystal's c-axis. Fig. 3.3a shows an example of one such measurement in which the absorption was recorded while the magnetic field perpendicular to the crystal c-axis was continuously ramped. By fitting to the energy levels extracted from this spectra and similar measurements for other field orientations, we determine $g_{e,\parallel} = 2.51 \pm 0.1$ and $g_{e,\perp} = 1.7 \pm 0.1$. Fig. 3.3b shows the absorption spectra expected from the spin Hamiltonian, which we see enables accurate predictions of the energy level splittings and relative transition absorption oscillator strengths in this case.

Optical transition strengths

The strength of the optical transitions can be characterized by assigning an oscillator strength to each individual transition. The absorption oscillator strength for a transition $|i\rangle \rightarrow |j\rangle$ for a polarized spectrum is given by [88, 89]

$$f_{ij} = 4\pi\epsilon_0 \frac{m_e c}{\pi e^2} \frac{1}{N} \sum_i \frac{9n_i}{(n_i^2+2)^2} \int \alpha_i(\nu) d\nu, \tag{3.10}$$

where ϵ is the vacuum permittivity, m_e is the mass of the electron, e is the charge on the electron, c is the speed of light, N is the number density, and the summation is over the three orthogonal polarizations states with α_i and n_i absorption coefficient

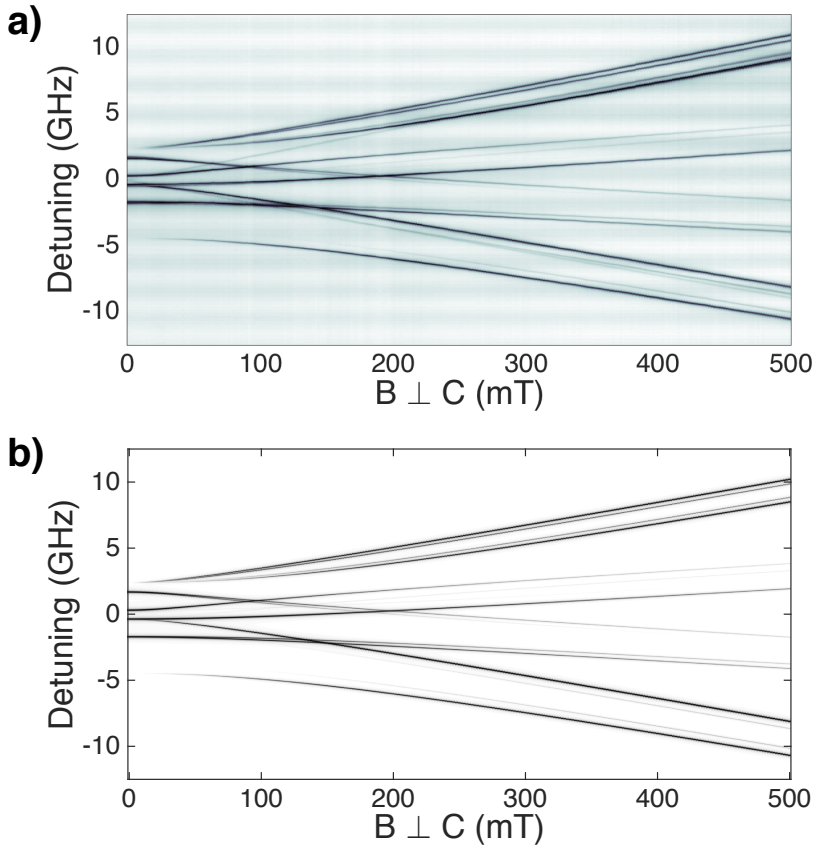

Figure 3.3: a) Typical high-resolution absorption spectra for a magnetic field ramp with $B, \mathbf{k} \perp c$ and $\mathbf{E} \perp c$ showing resolved optical hyperfine transitions. Darker regions correspond to higher absorption. b) Simulated absorption spectra using the experimentally determined spin Hamiltonian for magnetic field ramp with $B, \mathbf{k} \perp c$ and $\mathbf{E} \perp c$. The simulated absorption spectra take into account a slight misalignment ($\sim 1°$) between the crystal a-axis and the applied magnetic field.

and index of refraction, respectively. For YVO_4, $n_{\parallel} = 2.17$ and $n_{\perp} = 1.96$ at 984 nm [90].

Assuming a doping density of 100 ppm, the number density of Yb^{3+} in YVO_4 is calculated to be $N = 1.24{\times}10^{18}$ cm^{-3}, which is distributed between the four ground state levels according to Boltzmann statistics at 2 K. The integrated absorption coefficient and corresponding oscillator strengths for the observed transitions are summarized in Table 3.1. We measure an average oscillator strength of 5.3×10^{-6} for transitions allowed for $\mathbf{E} \parallel c$ (transitions A, E, I in Fig. 3.2) and 1.8×10^{-6} for transitions allowed for $\mathbf{E} \perp c$ (transitions C, F, G, H in Fig. 3.2).

The radiative lifetime for the ${}^2F_{5/2}(0) \rightarrow {}^2F_{7/2}(0)$ transitions can be determined

Table 3.1: Absorption properties of the ^{171}Yb:YVO_4 transitions as labeled in Fig. 3.2, including the transition polarization [5], integrated absorption coefficient, oscillator strength, and radiative decay rate at zero magnetic field.

Trans.	Pol.	$\int \alpha(\nu)d\nu$ (GHz/cm)	f (10^{-6})	$1/\tau_{\text{rad}}$ (kHz)
A	π	97.3	5.4	1.3
C	σ	16.4	1.0	0.3
E	π	102.7	5.5	1.4
F	σ	17.4	1.1	0.4
G	σ	20.2	2.6	0.2
H	σ	19.9	2.6	0.2
I	π	189.7	4.9	1.2

from the absorption measurements. The radiative lifetime for a transition $|j\rangle \rightarrow |i\rangle$ is related to the oscillator strength by [88, 89]

$$\frac{1}{\tau_{rad}} = \frac{2\pi e^2}{\epsilon_0 m_e c} \frac{(n^2+2)^2}{9n} \frac{n^2}{\lambda_0^2} \frac{f_{ji}}{3}, \tag{3.11}$$

where n is the index of refraction, λ_0 is the wavelength in vacuum, and f_{ji} is the emission oscillator strength. The emission oscillator strength is related to the absorption oscillator strength f_{ij} by $f_{ji} = \frac{g_i}{g_j} f_{ij}$, where g_i (g_j) is the degeneracy of state $|i\rangle$ ($|j\rangle$). The calculated emission rates for the observed transitions are included in Table 3.1. From these rates, we obtain an average radiative rate of $1/\tau_{rad} = 1/(590\ \mu\text{s})$ for the $^2F_{5/2}(0) \rightarrow {}^2F_{7/2}(0)$ transitions.

Excited state lifetimes

The excited-state lifetime is important for optical preparation of population among the spin states and sets the upper limit on the optical coherence time. The measured excited-state lifetime allows us to determine the optical branching ratio between the crystal field levels, which is important in the context of Purcell enhancement in nanophotonic cavities [91]. Here, we measure the excited-state lifetime through fluorescence decay.

To avoid the problem of radiation trapping [92] observed in previous measurements of excited-state lifetimes in Yb-doped materials [76, 78, 93], the excited-state lifetime was measured in a nominally undoped sample of YVO_4, which had a residual $^{171}Yb^{3+}$ concentration of approximately 2 ppm. In this sample, we did not see variations in the optical lifetime within the inhomogeneous line or other signs of radiation trapping. A typical fluorescence decay in this sample is shown in Fig. 3.4.

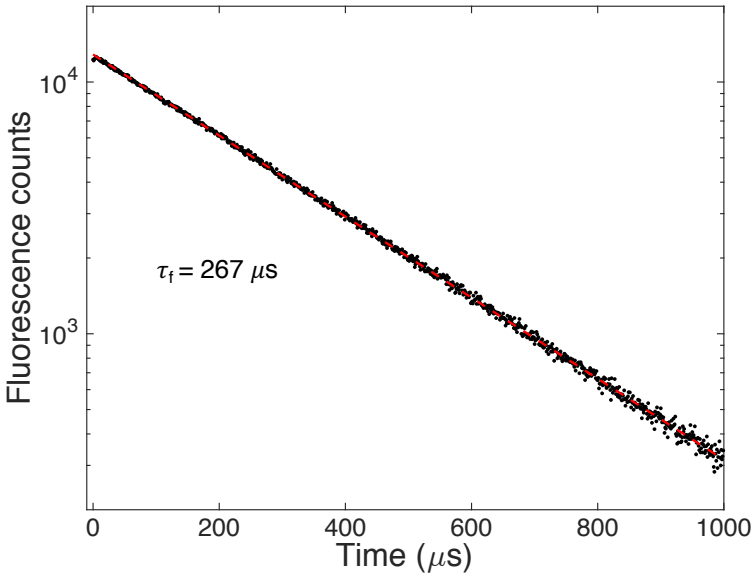

Figure 3.4: Excited-state lifetime measurement via fluorescence decay. An exponential fit (dashed line) gives $\tau_f = 267 \pm 1\ \mu s$.

Fitting to a single exponential gives a fluorescence lifetime of $\tau_f = 267 \pm 1\ \mu$s. The branching ratio back to the same crystal field level ($^2F_{5/2}(0) \rightarrow^2 F_{7/2}(0)$) is then given by $\beta = \tau_f/\tau_{rad}$, where τ_f and τ_{rad} are the fluorescence and radiative lifetimes. Using the radiative lifetime obtained from the absorption measurements, we determine the branching ratio to be $\beta = 0.45$

We also note that in a 200 μm thick 100 ppm sample we observed lifetimes longer than 500 μs in the center of the inhomogeneous distribution that decreased to less than 300 μs when the excitation pulse was detuned by 200 MHz from the center of the line. This behavior is attributed to radiation trapping due to the high optical depth and strong transition strengths of these ions.

Optical coherence measurements

To assess the ability to store quantum states in the material, we first investigate the coherence of the optical transition using two-pulse photon echoes (2PPE). For Kramers ions, we expect a dominant source of decoherence to be magnetic fluctuations due to magnetic dipole-dipole interactions between Yb ions [94]. One way to minimize this source of decoherence is to freeze out the electron spins by achieving a ground-state splitting much larger than k_bT [94]. For ^{171}Yb:YVO_4, the energy-level splitting is maximized for a magnetic field along the crystal c-axis. Here, we

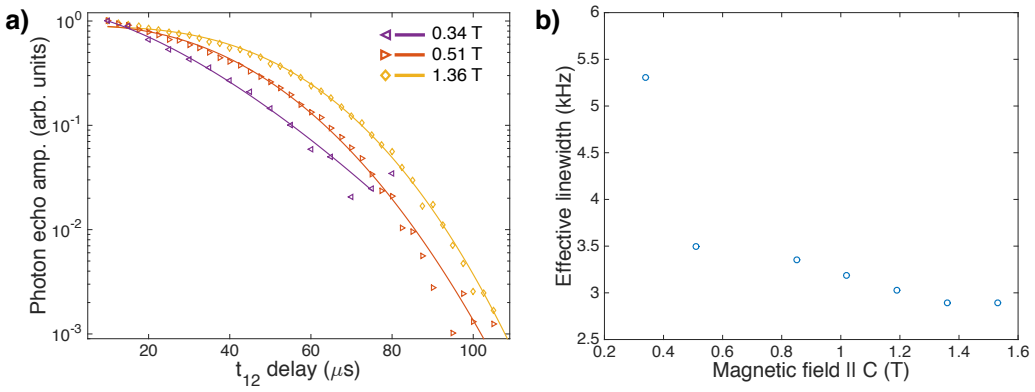

Figure 3.5: a) Typical photon echo decays for $B \parallel c$ showing an increase of coherence time and strong non-exponential decays with increasing magnetic field. Fits to a Mims decay are shown for each field value as a solid line (see main text for details). b) Effective linewidth extracted from the fits to the photon echo decays for $B \parallel c$.

present measurements of the optical coherence in the linear Zeeman regime with the magnetic field along the c-axis. While a comprehensive study is warranted to fully understand the decoherence mechanisms in this system, a large magnetic field applied parallel to c provides insight on the maximum achievable coherence times in this material and the dominant decoherence mechanisms.

Fig. 3.5a shows typical photon echo decays for magnetic fields ranging from 340 mT to 1.36 T along the crystal c-axis. We observed strong non-exponential decays, which can be attributed to spectral diffusion and described by a Mims decay [95]. For heterodyne detection, the decay of the echo field is given by [95]

$$E(t_{12}) = E_0 e^{-(2t_{12}/T_m)^x}, \tag{3.12}$$

where t_{12} is the delay between the two pulses used in the photon echo experiment, x is the Mims parameter describing the spectral diffusion, and T_m is phase memory time (the time at which the echo field amplitude decays to e^{-1} of its initial value). Fits to the Mims decay are shown as solid lines in Fig. 3.5a. From T_m, we can extract an effective homogeneous linewidth as $\Gamma_{\mathrm{h,eff}} = (\pi T_m)^{-1}$. The effective linewidth as a function of applied magnetic field along the c-axis is shown in Fig. 3.5b.

We observed a decrease in the linewidth with applied magnetic field from $\sim$5.5 kHz at 340 mT to $\sim$ 3 kHz at 1.5 T, which was the maximum magnetic field achievable for this measurement. The reduction in linewidth for increasing magnetic field is

expected for dephasing dominated by Yb-Yb spin flips and similar to that observed in other Kramers ions [94, 96]. At the highest magnetic fields, we saw that the coherence no longer increased with applied field. The non-exponential decay and saturation of coherence time in the high-field limit are typical signs of the superhyperfine limit [97]. In this limit, magnetic fluctuations due to the electron spins are effectively frozen out and the main contribution to dephasing is interactions with the nuclei of the host material.

We note that recent work in ^{171}Yb:Y_2SiO_5 [74] and ^{167}Er:Y_2SiO_5 [98] demonstrated an increase in coherence time due to reduced sensitivity to magnetic fluctuations at zero first-order Zeeman (ZEFOZ) points at $\mathbf{B} = 0$. While we did not explore the low-field regime in this work, Eq. (3.1) predicts similar zero-field ZEFOZ transitions in ^{171}Yb:YVO_4 between levels $|3\rangle_g$ and $|4\rangle_g$ of the ground state and $|1\rangle_e$ and $|2\rangle_e$ of the excited state.

Nuclear spin measurements

The coherence times of the ${}^2F_{7/2}(0)$ nuclear spin transitions will determine the feasibility of long-term quantum information storage in this system. In this section, we present measurements on the inhomogeneous linewidth and coherence properties of the $|1'\rangle_g \rightarrow |2'\rangle_g$ nuclear spin transition in the linear Zeeman regime.

The inhomogeneous broadening of the nuclear spin transition was measured using continuous-wave Raman heterodyne spectroscopy [83]. Fig. 3.6 shows a typical trace of the normalized Raman heterodyne signal power as the microwave frequency is swept across the resonance. Fitting this peak to a Lorentzian gives a FWHM of 250 kHz, which serves as an upper bound on the inhomogeneous broadening of the spin transition since the width of the observed signal can be power broadened by the Rabi frequencies of the optical and microwave fields used in the measurement [99]. The inhomogeneity of the nuclear spin transition can be attributed to variations in the crystal field due to strain and defects in the crystal and variations in the local magnetic field arising from spin-spin interactions [25], as well as inhomogeneity of the applied magnetic field along the beam path. This measurement was done with a field of 440 mT along c, but is typical of what was obtained for other magnetic field amplitudes applied along this direction.

The nuclear spin coherence was measured by spin echo decays with direct microwave manipulation of the $|1'\rangle_g \rightarrow |2'\rangle_g$ spin transition and optical detection

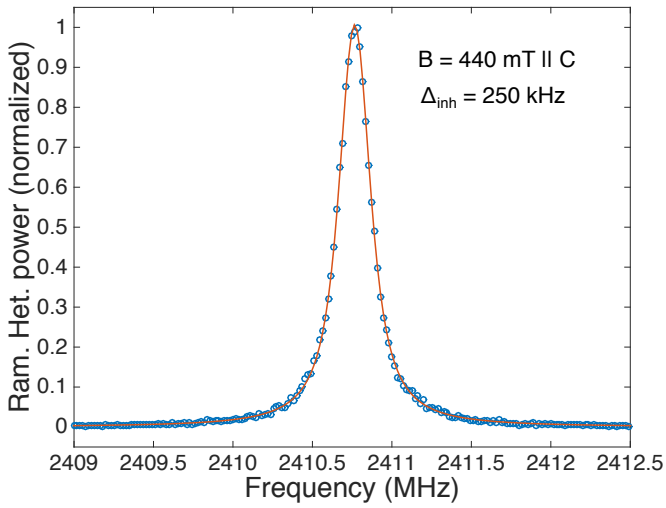

Figure 3.6: Continuous-wave Raman heterodyne measurement of the nuclear spin inhomogeneity with B = 440 mT parallel to the c-axis. A Lorentzian fit gives a FWHM of 250 kHz.

via coherent Raman scattering. Fig. 3.7 shows typical nuclear spin echo decays for increasing magnetic fields along the c-axis. For the higher field decays, we observed non-exponential decays resulting from time-varying dephasing mechanisms that can again described by the Mims decay using Eq. (3.12). We measured coherence times of 250 μs at 60 mT that increased up to 6.6 ms at a field of 440 mT, which was the maximum achievable magnetic field for the experimental configuration at the time of the measurement. Time-resolved measurements of the decay of the area of spectral holes prepared in the inhomogeneous line [25] gave spin relaxation times longer than 200 ms in this field configuration, indicating that these coherence times are not lifetime limited.

All-optical spin coherence measurements

In addition to direct microwave excitation of the nuclear spins, we are interested in performing coherent all-optical control on the nuclear spins. All-optical control allows us to take advantage of relatively strong optical transitions to perform faster manipulations on the spin. This approach also removes the need for a microwave circuit to be incorporated next to the sample, which reduces the complexity of the experimental setup and prevents additional heating of the sample through the microwave excitation. As an initial demonstration of the potential for all-optical control in this system, we use an all-optical Raman echo technique [100] to mea-

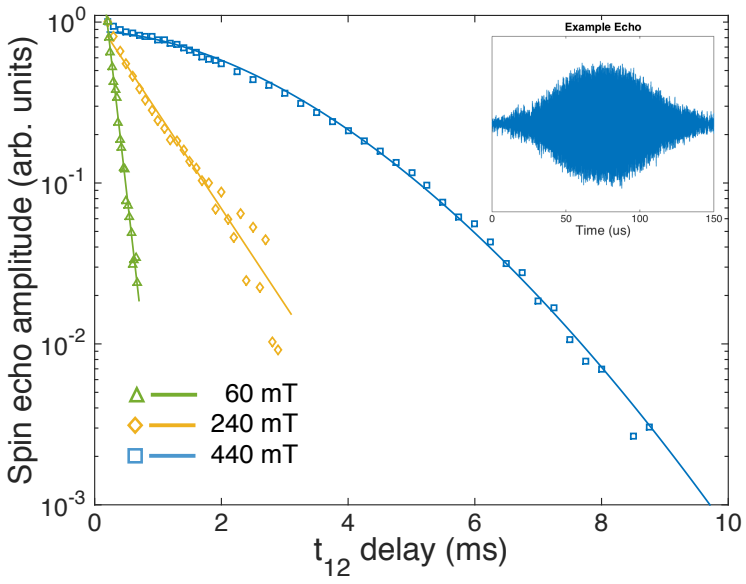

Figure 3.7: Typical nuclear spin echo decays for increasing applied magnetic field along the c-axis. The echo sequence is performed with direct microwave excitation and read out optically.

sure the coherence of the nuclear spin transition. The $|1'\rangle_g \rightarrow |2'\rangle_g$ transition is addressed by applying bichromatic pulses to the lambda system formed by the $|2'\rangle_g \rightarrow |1'\rangle_e$ and $|1'\rangle_g \rightarrow |1'\rangle_e$ optical transitions. Efficient rephasing of coherence on the spin transition using bichromatic pulses in this fashion requires that the Rabi frequencies of the two transitions of the lambda system are equal [85]. For magnetic fields applied parallel to the c-axis, one transition of the lambda system is weak because the wavefunctions have approached separability and the optical transition cannot flip the nuclear spin. Moving the field off axis induces mixing of the nuclear and electronic states, which allows for a more favorable branching ratio between the two arms of the lambda system.

Fig. 3.8 shows representative all-optical Raman echo decays for increasing applied magnetic fields applied 20° from the c-axis. Fitting to a Mims decay to describe the observed non-exponential behavior gave spin coherence times up to 1 ms at 480 mT, which was the maximum field available for this experiment. We note that moving the field off axis increases the magnetic sensitivity of the transition and therefore we expect a decrease of the spin coherence time in this regime. This configuration also reduces the ground state splitting, which would increase the contribution from Yb-Yb electron spin interactions. We expect to extend this coherence time with

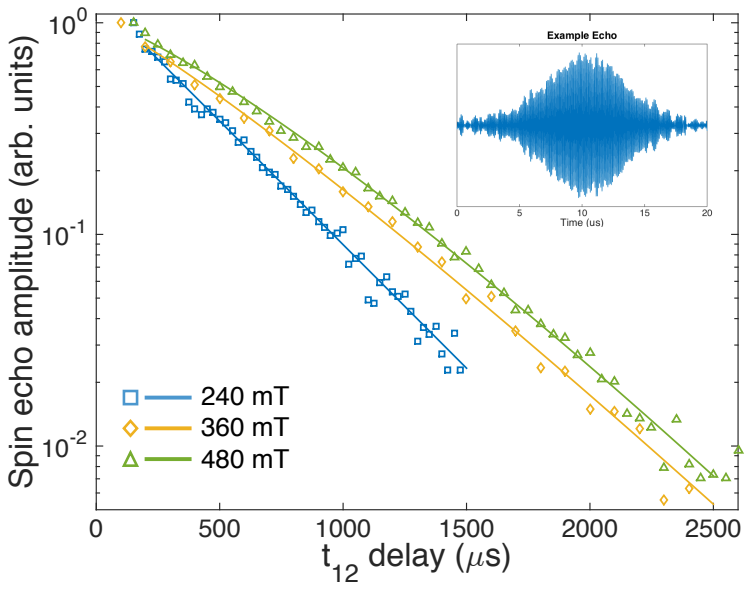

Figure 3.8: Typical nuclear spin echo decays for increasing magnetic fields applied 20° from the c-axis. Here, the entire sequence is performed using all-optical manipulation of the spins.

increasing magnetic fields as observed in the optical coherence measurements.

3.5 Summary and Conclusion

In this work, we have presented measurements assessing ^{171}Yb:YVO_4 for use in quantum interfaces focusing on the strength of the optical transitions, the energy level structure, and the coherence properties of the optical and spin transitions.

From optical absorption measurements, we extract oscillator strengths in the upper range of those observed in REIs and larger than those observed for $^{171}Yb^{3+}$ doped into Y_2SiO_5 and YAG [71, 76]. This oscillator strength is promising for detecting and manipulating single ions coupled to nanophotonic cavities. The combination of large oscillator strengths and narrow inhomogeneous broadening in this material gives rise to exceptionally large absorption coefficients for this material. Significantly, the peak absorption of 450 cm^{-1} is within a factor of 2 of the absorption in recently studied stoichiometric rare-earth crystals [101], even though the ion concentration is a factor of 10^4 more dilute. This absorption coefficient is promising for ensemble-based memories in bulk samples and reaching the impedance-matched regime necessary to achieve high-efficiency nanophotonic quantum memories. We observe a large branching ratio for relaxation directly to the ground state for the $^2F_{5/2}(0) \rightarrow {}^2F_{7/2}(0)$ transition, which is appealing in the context of Purcell en-

hancement of the emission rate in a nanocavity [1, 3].

The large hyperfine couplings and narrow inhomogeneous linewidths give rise to resolved optical-hyperfine transitions. This is useful for addressing and manipulating single transitions and states without additional preparation. The large nuclear spin transition splittings are also useful in the context of off-resonance memory schemes and high-bandwidth spin wave storage. We completed a characterization of the energy level structure by determining the excited-state spin Hamiltonian. The knowledge of the full spin Hamiltonian is essential for designing optimal quantum interfaces because it facilitates the prediction and engineering of lambda systems or highly cyclic transitions. The symmetry of the crystal gives rise to the strong selection rules on the optical transitions. These selection rules are advantageous for engineering cyclic transitions [102], especially in the context of a nanocavity that can preferentially enhance emission along one polarization.

For protocols requiring additional nuclear spin states, the ^{173}Yb isotope could be of interest because it has a nuclear spin of 5/2. The knowledge of the spin hamiltonian for the $^{171}Yb^{3+}$ isotope allows the spin Hamiltonian for the ^{173}Yb isotope to be approximated by scaling the hyperfine splittings by the ratio of the nuclear magnetic moments of the isotopes [103].

The optical coherence times are already sufficient for use in quantum applications and are promising from the perspective of reaching transform-limited photons in a nanocavity setting. The observed spin coherence properties show potential for use in spin-wave quantum memories and for single rare-earth ion qubits. In the linear Zeeman regime, the optical coherence times are limited by the superhyperfine interaction in the material. While a higher magnetic field regime was not available for the experimental configuration at the time of measurement, we expect the spin coherence times to increase with applied magnetic field as we completely freeze out the electron spin contribution. Further extension of the nuclear spin coherence time is predicted through the use of dynamic decoupling techniques [64]. We note that the doping density used in these measurements (100 ppm) is relatively high compared to many of the materials used for REI quantum technologies. We expect that by going to lower doping density samples we will reduce the contribution from Yb spin-spin interactions and observe longer optical and spin coherence times in the low field regime. Furthermore, by moving to lower temperatures, we can hope to freeze out the electron spins at lower magnetic fields. While this work focused on the optical and nuclear spin coherence properties in the linear Zeeman regime,

we calculate that a zero-field ZEFOZ transition exists for one of the ground state transitions, which is expected to lead to an enhancement of coherence [74, 98]. This configuration would also have the advantage of a strong electron spin transition between the ground states. This will be explored further in chapter 7. Future studies are warranted to investigate the spin coherence properties of this material at lower doping densities, temperatures, and different magnetic field regimes.

In summary, we find that ^{171}Yb:YVO_4 is a promising material for REI-based quantum interfaces, such as ensemble-based quantum memories, microwave-to-optical transduction, and single REIs in nanophotonic cavities. Based on these results, we decided to pursue optical detection and manipulation of single Yb ions using the nanobeam platform.

Chapter 4

THEORY: AN ION IN A CAVITY

"As everywhere in physics we mean by a model an approximation to the real state of affairs in which certain troublesome complications have been omitted; a model is a good one if the complications omitted have only a negligible influence on the main observed facts." - Dieke, *Spectra and Energy Levels of Rare Earth Ions in Crystals*

In this chapter, I give a brief introduction to the theoretical background relevant to understanding what happens when we place an ion in a nanophotonic cavity. I will start with the most fundamental model of interaction between light and atoms: the Jaynes-Cummings model. With the addition of a driving field and dissipation, I then discuss the physics of this model in the "bad cavity" regime where the cavity loss rate dominates over the other rates in the system and show how these equations of motion can be mapped to the semiclassical optical Bloch equations. This leads to a discussion of Purcell enhancement and how it can be achieved using cavities with high quality factors and low mode-volumes. After describing how the cavity can affect the properties of the ion, I'll show how the ion can modify the reflection and transmission response of the cavity in the low-excitation regime and comment on how to properly introduce dephasing when calculating power spectra in this regime. Lastly, I will plug in the experimentally relevant parameters to get a sense of what we can expect to achieve in this nanophotonic platform with ^{171}Yb:YVO_4 .

My goal in this chapter is develop some intuition and establish the vocabulary used in describing experimental results. In working this out, I will also explicitly point out any assumptions made and how definitions used here might differ from those seen in literature. The problem of an atom in a cavity has a long and rich history of research in quantum optics, which will not be covered comprehensively here. I will instead try to point the reader to useful resources along the way.

4.1 Setting up the problem

Here I am following a similar treatment to [104] and [105]. These papers in turn draw on a paper by Rice [106] and Carmichael's textbook [107], which are both suggested for the reader interested in a much more rigorous treatment. Steck's

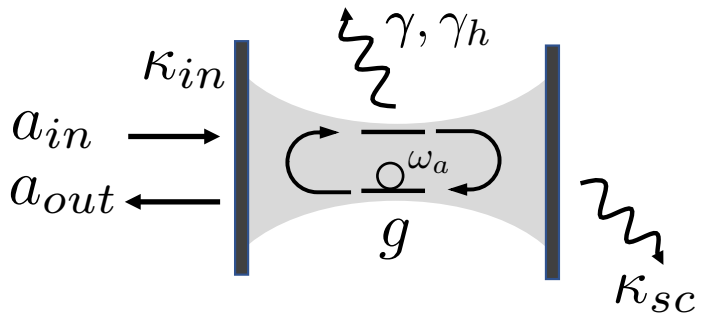

Figure 4.1: Jaynes-Cummings model of two-level emitter in a cavity. A two-level emitter with transition frequency ω_a and free space decay rate γ is coupled with single photon Rabi frequency $2g$ to a cavity with frequency ω_c. The cavity is probed in reflection with input coupling rate κ_{in} and total energy decay rate $\kappa = \kappa_{in} + \kappa_{sc}$.

Quantum Optics notes [108] also provide an excellent resource for this material.

We start with the most basic picture of the system as shown in Fig. 4.1. We consider a two-level atom with transition frequency ω_a in a single-mode optical cavity with frequency ω_c. The coupling between atom and cavity is determined by the single photon Rabi frequency, $2g$, which is given by

$$g = \frac{\mu}{\hbar}\sqrt{\frac{\hbar\omega}{2\epsilon_0 n^2 V}}. \tag{4.1}$$

Here, μ is the transition dipole moment, n is the refractive index of the medium, and V is the optical mode volume of the cavity [109]. We will assume that the atom sits in the maxima of the cavity electric field with optimal alignment between cavity polarization and dipole. We will interrogate this system with a laser of frequency ω_L. This is the standard Jaynes-Cummings model and in the rotating frame of the laser we can write the Hamiltonian for this system as:

$$H_{ac} = \frac{1}{2}\Delta_a\hat{\sigma}_z + \Delta_c\hat{a}^\dagger\hat{a} + g\left(\hat{a}^\dagger\hat{\sigma}_- + \hat{a}\hat{\sigma}_+\right), \tag{4.2}$$

where $\Delta_a = \omega_a - \omega_l$ and $\Delta_c = \omega_c - \omega_l$ are the atom and cavity detunings, respectively, $\hat{\sigma}_\pm$ corresponds to the standard Pauli operators for the emitter, and $\hat{a}$ ($\hat{a}^\dagger$) corresponds to the annihilation (creation) operator for the cavity mode. The first term in the Hamiltonian describes the free atom, the second describes the free cavity mode, and the last term is the atom-cavity electric dipole interaction in the rotating wave approximation. (Note $\hbar = 1$ throughout.)

We assume this is a one-sided cavity that we measure in reflection and introduce a classical coherent driving field that couples through the input mirror with rate κ_{in}.

The total cavity (energy) decay rate is given by $\kappa = \kappa_{in} + \kappa_{sc}$, where κ_{in} is the coupling rate of the input mirror and κ_{sc} encompasses all other loss mechanisms in the cavity (such as scattering loss or leakage through the other mirror). The atom (energy) decay rate in free space is γ. We start by considering the case where there is no additional dephasing of the two-level system, such that the homogeneous linewidth (HWHM) is determined by the lifetime as $\gamma_h = \gamma/2$. In contrast to atomic systems, solid-state systems typically exhibit excess dephasing on top of this lifetime limit. We will introduce this excess dephasing as γ_{deph} so that the total dephasing rate become becomes $\gamma_d = \gamma/2 + \gamma_{deph}$.

We start with the Heisenberg-Langevin approach to develop some intuition and obtain a set of equations that mirror semiclassical formalism. In this approach, the damping terms (κ and γ) are introduced using an open systems approach in which they correspond to a coupling to a continuum of bath modes [107]. From this Hamiltonian, the corresponding Heisenberg-Langevin equations (HLEs) of motion for the operators and the input-output relation for the cavity field are [104, 108]:

$$\dot{\hat{a}} = -ig\hat{\sigma}_- - \left(\frac{\kappa}{2} + i\Delta_c\right)\hat{a} - \sqrt{\kappa_{in}}\hat{a}_{in} + \hat{f} \tag{4.3}$$

$$\dot{\sigma}_- = ig\hat{a}\hat{\sigma}_z - \left(\frac{\gamma}{2} + i\Delta_a\right)\hat{\sigma}_- + \hat{g} \tag{4.4}$$

$$\dot{\sigma}_z = -2ig\left(\hat{\sigma}_+\hat{a} - \hat{a}^\dagger\hat{\sigma}_-\right) - \gamma\left(\hat{\sigma}_z + 1\right) + \hat{h} \tag{4.5}$$

$$\hat{a}_{out} = \sqrt{\kappa_{in}}\hat{a} + \hat{a}_{in}. \tag{4.6}$$

Note that $\hat{f}$, $\hat{g}$, and $\hat{h}$ are noise operators that must be introduced in the Heisenberg-Langevin formalism to properly preserve the commutation relations. For the purpose of the discussion here, we will invoke the cold vacuum assumption in which these decay terms only act to pull energy from the system [106]. This assumption is well justified for our ion-cavity systems where we work at optical frequencies and liquid helium temperatures. When we take expectation values of these equations, the noise operators will operate on vacuum and will evaluate to zero. With this in mind, I will drop these terms in the following expressions.

4.2 Bad cavity limit

The relevant physics of this system depends on the relative sizes of g, κ, and γ. For the ion-cavity systems investigated here, we are working in the "bad cavity" limit [1] in which the cavity decay dominates over all other rates in the system ($\kappa \gg g > \gamma$).

[1] This is also referred to as the "fast cavity" or"Purcell" limit depending on the optimism of the writer.

In this regime, we adiabatically eliminate the cavity mode (i.e., set $\dot{\hat{a}} = 0$) [106] to get the following expression for the cavity field:

$$\hat{a} = \frac{-ig\hat{\sigma}_- - \sqrt{\kappa_{in}}\hat{a}_{in}}{\tilde{\kappa}}, \tag{4.7}$$

where $\tilde{\kappa} = \kappa/2 + i\Delta_c$. We substitute this expression for the cavity field (Eq. (4.7)) into the HLEs (Eq. (4.4) and Eq. (4.5)) to get the following equations of motion for the atom

$$\dot{\sigma}_- = -\left(\tilde{\gamma} + \frac{g^2}{\tilde{\kappa}}\right)\hat{\sigma}_- - ig\frac{\sqrt{\kappa_{in}}}{\tilde{\kappa}}\hat{a}_{in}\hat{\sigma}_z \tag{4.8}$$

$$\dot{\sigma}_z = -\left(\gamma + \frac{g^2\kappa}{|\tilde{\kappa}|^2}\right)(\hat{\sigma}_z + 1) + 2ig\sqrt{\kappa_{in}}\left(\frac{\hat{\sigma}_+\hat{a}_{in}}{\tilde{\kappa}} - \frac{\hat{\sigma}_-\hat{a}_{in}^\dagger}{\tilde{\kappa}^\dagger}\right). \tag{4.9}$$

A few useful expressions

Before moving on, we can quickly extract a few useful expressions. In the case of no input field ($\hat{a}_{in} = 0$), the cavity field is given from Eq. (4.7) as

$$\hat{a} = \frac{-ig\hat{\sigma}_-}{\tilde{\kappa}}, \tag{4.10}$$

so that from Eq. (4.6) the field at the output of the cavity is given by

$$\hat{a}_{out} = -\frac{i\sqrt{\kappa_{in}}g\hat{\sigma}_-}{\tilde{\kappa}}. \tag{4.11}$$

The rate of photons leaving the cavity then follows as

$$n_{out} = \langle\hat{a}_{out}^\dagger\hat{a}_{out}\rangle = \frac{\kappa_{in}g^2}{|\tilde{\kappa}|^2}\langle\hat{\sigma}_+\hat{\sigma}_-\rangle \to \frac{\kappa_{in}}{\kappa}\frac{4g^2}{\kappa}\langle\hat{\sigma}_+\hat{\sigma}_-\rangle, \tag{4.12}$$

where the last expression holds on resonance ($\Delta_c = 0$). We see that the photon rate of the undriven cavity directly maps to the population of the atom. It is also useful to consider the case of an empty cavity ($g = 0$), in which

$$\hat{a} = \frac{-\sqrt{\kappa_{in}}\hat{a}_{in}}{\tilde{\kappa}}. \tag{4.13}$$

The mean photon number in the cavity is then

$$\bar{n} = \langle\hat{a}^\dagger\hat{a}\rangle = \frac{\kappa_{in}}{|\tilde{\kappa}|^2}\langle\hat{a}_{in}^\dagger\hat{a}_{in}\rangle. \tag{4.14}$$

We identify $n_{in} = \langle\hat{a}_{in}^\dagger\hat{a}_{in}\rangle$ as input photon rate (photons per second). The mean photon number in the cavity on-resonance is then

$$\bar{n} = \frac{4\kappa_{in}}{\kappa^2}n_{in} = \frac{4\kappa_{in}}{\kappa^2}\frac{P_{in}}{\hbar\omega}, \tag{4.15}$$

where P_{in} is the incident power. We can also write down the empty cavity reflection spectrum from the input-output relation:

$$r(\Delta_c) = \frac{\hat{a}_{out}}{\hat{a}_{in}} = 1 - \frac{\kappa}{\tilde{\kappa}}. \tag{4.16}$$

The reflected power spectrum from the cavity is then

$$|r(\Delta_c)|^2 = \frac{n_{out}}{n_{in}} = \left|1 - \frac{\kappa_{in}}{\tilde{\kappa}}\right|^2 = \frac{(\kappa_{in} - \kappa/2)^2 + \Delta_c^2}{(\kappa/2)^2 + \Delta_c^2}. \tag{4.17}$$

Mapping to optical Bloch equations

In the bad cavity limit, we can map the HLEs to the usual semiclassical optical Bloch equations for a two-level system. For simplicity, we assume that we are on resonance with the cavity ($\Delta_c = 0$). We can recover the semi-classical equations of motion by taking the expectation values of the HLEs. This semi-classical limit amounts to treating the input field as a well-defined classical amplitude such that the expectation values of field and cavity are separable [106]. The resulting equations are

$$\langle\dot{\hat{\sigma}}_-\rangle = -\left(\frac{1}{2}\left(\gamma + 4\frac{g^2}{\kappa}\right) + i\Delta_a\right)\langle\hat{\sigma}_-\rangle - ig\frac{2\sqrt{\kappa_{in}}}{\kappa}\langle\hat{a}_{in}\rangle\langle\hat{\sigma}_z\rangle \tag{4.18}$$

$$\langle\dot{\hat{\sigma}}_z\rangle = -\left(\gamma + 4\frac{g^2}{\kappa}\right)(\langle\hat{\sigma}_z\rangle + 1) + i2g\left(\langle\hat{\sigma}_+\rangle\frac{2\sqrt{\kappa_{in}}\langle\hat{a}_{in}\rangle}{\kappa} - \langle\hat{\sigma}_-\rangle\frac{2\sqrt{\kappa_{in}}\langle\hat{a}_{in}^\dagger\rangle}{\kappa}\right). \tag{4.19}$$

These equations can be put into the following form:

$$\langle\dot{\hat{\sigma}}_-\rangle = -\left(\frac{\gamma_{cav}}{2} + i\Delta_a\right)\langle\hat{\sigma}_-\rangle - i\frac{\Omega_r}{2}\langle\hat{\sigma}_z\rangle \tag{4.20}$$

$$\langle\dot{\hat{\sigma}}_z\rangle = -\gamma_{cav}\left(\langle\hat{\sigma}_z\rangle + 1\right) + i\Omega_r\left(\langle\hat{\sigma}_+\rangle - \langle\hat{\sigma}_-\rangle\right), \tag{4.21}$$

where we define $\gamma_{cav} = \gamma + 4g^2/\kappa$ as the decay rate of the ion in the cavity, $\sqrt{\bar{n}} = \frac{2\sqrt{\kappa_{in}}}{\kappa}\langle\hat{a}_{in}\rangle$ as the mean photon number in the cavity, and $\Omega_r = 2g\sqrt{\bar{n}}$ as the Rabi frequency in the cavity. We recognize these as the optical Bloch equations. In this approximation, we can then think of the dynamics of the atom using the usual intuition for the driven two-level system with a new lifetime and Rabi frequency defined by the coupling to the cavity. For a review of the two-level atom, the reader is referred to many fine resources, such as Steck [108], Fox [110], or the classic text by Allen and Eberly [111] .

4.3 Purcell Enhancement

From the above, we see that the decay rate of the atom in the cavity has been modified from its free space value γ to [2]

$$\gamma_{cav} = \gamma + \frac{g^2\kappa}{|\tilde{\kappa}|^2}. \tag{4.22}$$

This modification of the ion emission rate due to the presence of a cavity is the Purcell effect [91]. This is named after Purcell's seminal paper with the crucial insight that the lifetime of an emitter fundamentally depends on its local environment. The ratio of the emitter decay rate in the cavity to the emitter decay rate in free space is

$$\frac{\gamma_{cav}}{\gamma} = 1 + \frac{g^2\kappa}{|\tilde{\kappa}|^2\gamma}, \tag{4.23}$$

$$= 1 + \tilde{\eta}, \tag{4.24}$$

where $\tilde{\eta} = \frac{g^2\kappa}{\gamma|\tilde{\kappa}|^2}$. For zero detuning, this reduces to $\eta = \frac{4g^2}{\kappa\gamma}$, which we call here the Purcell factor. This constant is one the standard figures of merit for describing a cavity QED system. It is worth noting that there are a few different conventions for defining this factor depending on whether you pick energy or field decay rates for κ and γ. In the context of systems that are lifetime broadened (e.g. atomic systems), this same constant is also referred to as the cooperativity. In the case of excess dephasing, one needs to distinguish between the Purcell factor in which the excited state decay rate is the relevant parameter and cooperativity in which the dephasing rate is the relevant parameter. We will define the cooperativity as $\eta_d = 2g^2/\kappa\gamma_d$, where $\gamma_d = \gamma/2 + \gamma_{deph}$. We see that for $\eta_d = \eta$ for the case of no added dephasing[3].

To enable efficient detection of single rare-earth ions, we want to achieve large Purcell factors to enhance the emission rate of the ions and squeeze out more photons per second. We can get a better intuition on how to achieve this regime by writing this in terms of the physical parameters of the cavity. One can get the standard expression for the Purcell factor by plugging in the expressions for g and γ. The

[2] Here we have assumed that the free space decay rate is not modified in the presence of the cavity, which is a reasonable assumption if the cavity does not take up a large solid angle of the atomic emission [108].

[3] Note that some authors use a slightly different convention in which the total dephasing rate is defined as $\gamma_d/2$ such that the expression for the cooperativity more closely resembles that in the lifetime-limited case. This then boils down to the choice of whether the full-width at half-max (FWHM) of the transition is defined as γ_d or $2\gamma_d$. Overall, caution is advised in comparing systems based on values from different papers without first checking for pesky factors of two based on the convention used by the authors.

emission rate in free space is given by [4]

$$\gamma = \frac{2}{3}\frac{\omega^3}{hc^3\epsilon_0} n|\mu|^2, \tag{4.25}$$

where g was defined in Eq. (4.1), and we can relate the cavity energy decay rate to the quality factor $Q = \omega_c/\kappa$. With these substitutions, we have

$$F_p = \frac{3}{4\pi^2}\frac{Q}{V}\left(\frac{\lambda}{n}\right)^3. \tag{4.26}$$

In this form, we see that the dipole moment drops out and the enhancement is determined entirely by physical parameters of the cavity. The experimental task for achieving large Purcell factors is then to build cavities with large quality factors and small mode volumes.

Typically, we are working with a multi-level system in which an ion in the excited state can decay via multiple paths. A slight complication arises when applying the above to a multi-level system, where it should be kept in mind that the enhancement above is the enhancement of the emission rate of the transition coupled and aligned to the cavity mode. For total excited state decay rate of γ_0, the free space decay rate on the transition of interest given by $\beta\gamma_0$, where β is the branching ratio for emission on that transition. The total decay rate of the ion in the cavity is then modified to

$$\gamma_c = (1-\beta)\gamma_0 + (1+F_p)\beta\gamma_0 = (1+\beta F_p)\gamma_0. \tag{4.27}$$

In the literature, both F_p and βF_p are often referred to as the Purcell factor of the system. In this work I will reserve F_p for describing the enhancement of the cavity-coupled transition rate. In this case, βF_p can be considered as the "effective Purcell" enhancement where $\beta F_p = \eta = 4g^2/\kappa\gamma$.

Enhancement of collection efficiency

The goal is to squeeze as many photons as possible out of the ion. In addition to just enhancing the emission rate, we also see that the Purcell effect helps funnel photons into a mode from which we can more readily collect them. The fraction of the ion emission that goes into the cavity mode is given by the ratio of emission into the cavity to the total emission rate:

$$P_{cav} = \frac{\beta F_p}{1+\beta F_p}. \tag{4.28}$$

[4] In working with rare-earth ions in solids, the expression for decay rate typically also includes a local-field correction (LFC) factor, χ. We will discuss this complication shortly, but the prescription for including a LFC in these expressions is $\mu \to \chi\mu$.

The total fraction of emission coupled out of the cavity into the collection mode is given by:

$$P_{out} = \frac{\kappa_{in}}{\kappa} \frac{\beta F_p}{1 + \beta F_p}. \tag{4.29}$$

We want $\kappa_{in}/\kappa \to 1$ and the Purcell factor to be much larger than one to collect as much light from the ions as possible.

Enhancement of cyclicity

An important consequence of Purcell enhancement in our system is that it can be used to enhance the cyclicity of the optical transitions. Cyclicity in this context refers to the probability that an excited ion will return to its original state upon emission of a photon. This will be especially important in the context of single-shot readout in which we want to be able to repeatedly excite the ion multiple times and determine its state by measuring the emitted photons before the ion relaxes to another state.

Let's apply this to the case of the zero-field ^{171}Yb:YVO_4 level structure presented in Chapter 3 and assume we excite the ion on a transition allowed for $E \parallel c$. Once in the excited state, the ion can decay via the 984 nm transition back to the same initial ground state with rate $\Gamma_\parallel$ or decay to another ground state with $\Gamma_\perp$. It can also decay through the other crystal field levels with rate Γ_{other}. We will be pessimistic and assume in this case that it always ends up in a different ground state. The total excited state decay rate Γ_0 is given by

$$\Gamma_0 = \Gamma_\parallel + \Gamma_\perp + \Gamma_{other}. \tag{4.30}$$

We define the branching ratio for decay via the 984 transition as $\beta_{980} = (\Gamma_\parallel + \Gamma_\perp)/\Gamma_0$. As presented in Chapter 3, we have determined $\beta_{980} \approx 0.45$. Similarly, we can extract the branching ratio within the 984 nm transition as $\beta_\parallel^{980} = \Gamma_\parallel / (\Gamma_\parallel + \Gamma_\perp) \approx 0.8$. The overall branching ratio (cyclicity) for the parallel transition is then $\beta_\parallel \approx 0.36$.

If we assume that we only Purcell enhance the transition $\Gamma_\parallel$, we get the total decay rate in the cavity:

$$\Gamma_{cav} = (1 + F_p)\beta_\parallel \Gamma_0 + (1 - \beta_\parallel)\Gamma_0. \tag{4.31}$$

The new branching ratio for this transition is then given by

$$\beta_\parallel^{cav} = \frac{(1 + F_p)\beta_\parallel \Gamma_0}{\Gamma_{cav}} = \frac{(1 + F_p)\beta_\parallel}{1 + F_p \beta_\parallel^{tot}}. \tag{4.32}$$

We then use $\Gamma_{cav} = (1 + F_p\beta_\parallel)\Gamma_0$ to eliminate F_p and get a form useful for the experimenter:

$$\beta_\parallel^{cav} = 1 - (1 - \beta_\parallel)\,\frac{T_1^{cav}}{T_1^{bulk}}. \tag{4.33}$$

For a realistically achievable cavity lifetime of $T_1^{cav} = 2\ \mu$s and bulk lifetime of $T_1^{bulk} = 267\ \mu$s, this gives $\beta_\parallel^{cav} = 0.9976$. This is a drastic improvement from the cyclicity observed in the bulk material and will start to make single-shot readout a possibility in our systems.

Increasing indistinguishability

Quantum networks based on photon interference require a source of indistinguishable photons. Purcell enhancement can be used to increase the indistinguishability of single photon emission from the cavity coupled ions. Let us assume that the optical transition is broadened by excess dephasing such that

$$\frac{1}{T_2} = \frac{1}{2T_1} + \gamma_{deph}. \tag{4.34}$$

We will assume that there is no additional spectral diffusion process ($T_2 = T_2^*$) such that the FWHM linewidth of this transition is given by $\Delta\nu = 1/\pi T_2$ (Hz). Letting $\gamma = 1/T_1$, the indistinguishability of photon emission is then given by [109] [5]:

$$I = \frac{T_2}{2T_1} = \frac{\gamma}{\gamma + 2\gamma_{deph}} = \frac{1}{1 + \frac{2\gamma_{deph}}{\gamma}}. \tag{4.35}$$

In this form we see that the indistinguishability can be improved by reducing the relative contribution of excess dephasing to the coherence time through Purcell enhancement of the excited state decay rate [112, 113].

4.4 Cavity reflection spectrum in the low excitation regime

Now that we have explored the effect of the cavity on the properties of the ion, we can also consider the effect of the ion on the reflection or transmission spectrum of the cavity. I will first approach this problem in the semi-classical limit with the assumption that the ion has no additional dephasing beyond the lifetime limit. I will then introduce dephasing and discuss a pitfall to avoid in this approach.

[5] In the case of spectral diffusion, the expression for indistinguishability becomes more complex and depends on the relative rates and amplitudes of the dephasing processes involved. A pessimistic lower bound can be extracted in that case using T_2^* in place of T_2. The interested reader is referred to [109] for a better estimate.

We assume the low-excitation limit such that the ion is almost always in the ground state ($\sigma_z \approx -1$), which corresponds to an input photon rate that is much less than one photon per cavity-enhanced lifetime [104]. The HLEs (Eq. (4.3) and Eq. (4.4)) are then simplified to

$$\dot{\hat{a}} = -ig\hat{\sigma}_- - \tilde{\kappa}\hat{a} - \sqrt{\kappa_{in}}\hat{a}_{in} \tag{4.36}$$

$$\dot{\sigma}_- = -ig\hat{a} - \tilde{\gamma}\hat{\sigma}_-, \tag{4.37}$$

where $\tilde{\kappa} = \kappa/2 + i\Delta_c$ and $\tilde{\gamma} = \gamma/2 + i\Delta_a$. As before, we can obtain semi-classical expressions by taking the expectation values of these equations and treating the field as a well-defined classical amplitude. We again use the adiabatic approximation that the input field is slowly varying compared to all the time scales in the system (essentially solving for the system in the steady state) to get the following equations:

$$0 = -ig\langle\hat{\sigma}_-\rangle - \tilde{\kappa}\langle\hat{a}\rangle - \sqrt{\kappa_{in}}\langle\hat{a}_{in}\rangle \tag{4.38}$$

$$0 = -ig\langle\hat{a}\rangle - \tilde{\gamma}\langle\hat{\sigma}_-\rangle. \tag{4.39}$$

These can be solved to give

$$\langle\hat{a}\rangle = -\frac{\sqrt{\kappa_{in}}}{\tilde{\kappa}\left(1 + \frac{g^2}{\tilde{\gamma}\tilde{\kappa}}\right)}\langle\hat{a}_{in}\rangle \tag{4.40}$$

$$\langle\hat{\sigma}_-\rangle = \frac{ig\sqrt{\kappa_{in}}}{\tilde{\gamma}\tilde{\kappa}\left(1 + \frac{g^2}{\tilde{\gamma}\tilde{\kappa}}\right)}\langle\hat{a}_{in}\rangle. \tag{4.41}$$

Plugging these into the input-output relation (Eq. (4.6)), we get the following expression for the field reflected from the cavity:

$$r(\Delta_c, \Delta_a) = \frac{\langle\hat{a}_{out}\rangle}{\langle\hat{a}_{in}\rangle} = \frac{1 + \tilde{\eta} - \kappa_{in}/\tilde{\kappa}}{1 + \tilde{\eta}}. \tag{4.42}$$

On resonance we have $\tilde{\kappa} = \kappa/2$ and $\tilde{\eta} = \eta = 4g^2/\kappa\gamma$, so this reduces to

$$\frac{\langle\hat{a}_{out}\rangle}{\langle\hat{a}_{in}\rangle} = \frac{1 + \eta - 2\kappa_{in}/\kappa}{1 + \eta}. \tag{4.43}$$

We see that the presence of the ion in the cavity modifies the reflection spectrum for the cavity. For a perfectly one-sided cavity ($\kappa_{in} = \kappa$), this becomes

$$\frac{\langle\hat{a}_{out}\rangle}{\langle\hat{a}_{in}\rangle} = \frac{\eta - 1}{\eta + 1}. \tag{4.44}$$

So we see that in the high cooperativity limit ($\eta \gg 1$) there is a π phase difference in the reflected field between the presence and absence of an atom ($\hat{a}_{out} = \pm\hat{a}_{in}$). This conditional phase shift of reflected photons on the presence or absence of the cavity-coupled emitter has been demonstrated for instance in nanophotonic platforms with quantum dots [114] and neutral atoms [104]. We are also interested in measuring the reflected power spectrum of the cavity, which is given from this treatment as

$$|r(\omega)|^2 = \left|\frac{1 + \tilde{\eta} - \kappa_{in}/\tilde{\kappa}}{1 + \tilde{\eta}}\right|^2. \tag{4.45}$$

Adding dephasing in the low excitation limit

The above treatment is assuming that the dephasing of the atom is lifetime-limited. This is a good assumption for many atomic systems, but is often not the case for solid-state emitters. We next explore how to adequately introduce dephasing in the low-excitation regime.

In the presence of additional dephasing, we can introduce dephasing into semi-classical Bloch equations such that the total dephasing rate is $\gamma_d = \gamma/2 + \gamma_{deph}$ (and similarly, $\tilde{\gamma}_d = \gamma_d + i\Delta_a$). This excess dephasing is only added into the evolution of the coherences, such that the expression for σ_- now becomes

$$\dot{\sigma}_- = ig\hat{a}\hat{\sigma}_z - \left(\frac{\gamma}{2} + \gamma_{deph} + i\Delta_a\right)\hat{\sigma}_- \tag{4.46}$$

$$= ig\hat{a}\hat{\sigma}_z - (\gamma_d + i\Delta_a)\,\hat{\sigma}_-. \tag{4.47}$$

Working through the preceding sections for the low-excitation regime reflection spectrum, we arrive at the same equations as above with the replacement $\tilde{\eta} \to \tilde{\eta}_d = 2g^2/\kappa\tilde{\gamma}_d$:

$$|r(\omega)|^2 = \left|\frac{1 + \tilde{\eta}_d - \kappa_{in}/\tilde{\kappa}}{1 + \tilde{\eta}_d}\right|^2. \tag{4.48}$$

Experimentally, we are interested in extracting the cooperativity (η_d) by measuring the change in the power reflection spectrum of the cavity due to the presence of the ion. We can compare the predictions of this expression to a simulation of the system based on the master equation formalism [6] for parameters achievable in our devices. This is shown in Fig. 4.2. We see that above results from the low excitation approximation do not adequately treat dephasing when calculating the power reflection spectrum. While the prediction is fairly close in the case of an undercoupled

[6] Simulations done in QuTIP (Quantum Toolbox in Python) [115].The tutorials included with the QuTIP documentation are a good to place to start, but it is worth having a look at [108] or [107] for a more thorough introduction on the master equation formalism.

cavity, the discrepancy becomes more pronounced as κ_{in}/κ increases. It is worth noting that the discrepancy between the semiclassical expression and simulation is especially strong in regimes where $\eta_d \ll \eta$, which is typical for the rare-earth ion system. In general, this means that we will not accurately extract the cooperativity from the reflection spectra using the current semiclassical formula. While we can always resort to full simulations, we want to try to fix this semi-classical expression to more readily extract the cooperativity from the measured reflection if we can.

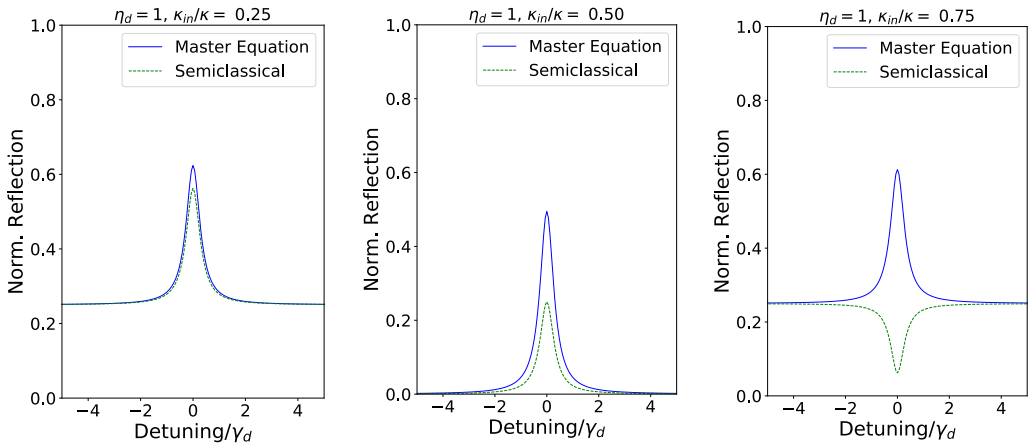

Figure 4.2: Comparison of semi-classical expressions for the reflection spectrum in the presence of dephasing predicted by Eq. (4.48) to master equation simulations done in QuTIP. For this simulation, we are using parameters achievable in the Yb:YVO system: $g = 2\pi \times 20$ MHZ, $\kappa = 2\pi \times 30$ GHz, $1/\gamma = 267\mu$s, and $\eta_d = 1$ for three different cavity input coupling rates

To reconcile this and generate a corrected semi-classical expression, I will follow the treatment of Waks in [105]. Waks encounters a similar problem in analyzing a metal nanoparticle-emitter system and presents a nice description of why this fails. In the semiclassical treatment we are assuming that the field is quantified by a fixed amplitude. We are treating the dipole as a linear scatterer and the field as a coherent field. If we introduce dephasing, the field inside the cavity must now be considered as an ensemble of coherent field amplitudes with different phases rather than a single coherent field. We then need to be more careful and average out the photon number operator rather than the field amplitude! Basically, we took the expectation value too early in the above derivation. When we introduce dephasing, we need to solve for the desired photon number expression (e.g. cavity power reflection) and then take the expectation value.

We can more easily show where exactly the above derivation fails by looking at the number of photons in the cavity. Starting from the HLE, we take the adiabatic approximation and get the solution for the cavity field as

$$\hat{a} = \frac{-ig\hat{\sigma}_- - \sqrt{\kappa_{in}}\hat{a}_{in}}{\tilde{\kappa}}. \tag{4.49}$$

The expected number of photons in the cavity is then

$$n_{corr} = \langle \hat{a}^\dagger \hat{a} \rangle = \frac{\kappa_{in}|\hat{a}_{in}|^2 + g^2\langle \hat{\sigma}_+\hat{\sigma}_- \rangle + 2g\sqrt{\kappa_{in}}\,\mathrm{Im}\{\langle \hat{\sigma}_- \rangle\}\langle \hat{a}_{in} \rangle}{|\tilde{\kappa}|^2}. \tag{4.50}$$

This expression has not made any low excitation assumptions yet. We can compare this to the case where we make the semiclassical approximation first as done in the preceding section:

$$n_{semi} = |\langle \hat{a} \rangle|^2 = \left| \frac{-ig\langle \hat{\sigma}_- \rangle - \sqrt{\kappa_{in}}\langle \hat{a}_{in} \rangle}{\tilde{\kappa}} \right|^2 \tag{4.51}$$

$$= \frac{\kappa_{in}|\hat{a}_{in}|^2 + g^2|\langle \hat{\sigma}_- \rangle|^2 + 2g\sqrt{\kappa_{in}}\,\mathrm{Im}\{\langle \hat{\sigma}_- \rangle\}\langle \hat{a}_{in} \rangle}{|\tilde{\kappa}|^2}. \tag{4.52}$$

The crucial difference between these two is that in the corrected expression, we have a dependency on the population of the excited state $\langle \hat{\sigma}_+\hat{\sigma}_- \rangle = \rho_{22}$ while in the second we are using the phase term $|\langle \hat{\sigma}_- \rangle|^2$. These are equal for the case of weak driving in the case of no dephasing (where $|\rho_{21}|^2 = \rho_{11}\rho_{22} \approx \rho_{22}$ when $\rho_{11} \approx 1$). The introduction of dephasing will reduce $|\langle \hat{\sigma}_- \rangle|^2$, but will not have an effect on the population term ρ_{22}.

To evaluate the corrected expression, we still need solutions for $\langle \hat{\sigma}_+\hat{\sigma}_- \rangle = \rho_{22}$ and $\langle \hat{\sigma}_- \rangle$. We can obtain these from the results presented earlier, where the population in the bad cavity limit was

$$\dot{\sigma}_z = -\tilde{\gamma}_c\,(\hat{\sigma}_z + 1) + 2ig\sqrt{\kappa_{in}}\left(\frac{\hat{\sigma}_+\hat{a}_{in}}{\tilde{\kappa}} - \frac{\hat{\sigma}_-\hat{a}_{in}^\dagger}{\tilde{\kappa}^\dagger} \right). \tag{4.53}$$

In steady-state, we then have

$$\langle \hat{\sigma}_z \rangle = -1 + \frac{2ig\sqrt{\kappa_{in}}}{\gamma_c}\left(\frac{\langle \hat{\sigma}_+ \rangle\langle \hat{a}_{in} \rangle}{\tilde{\kappa}} - \frac{\langle \hat{\sigma}_- \rangle\langle \hat{a}_{in}^\dagger \rangle}{\tilde{\kappa}^\dagger} \right). \tag{4.54}$$

We relate this to ρ_{22} using $\rho_{22} = (\langle \hat{\sigma}_z \rangle + 1)/2$. For $\langle \hat{\sigma}_- \rangle$, we use the expression from the low-field limit ($\langle \hat{\sigma}_z \rangle = -1$) found earlier with the corresponding introduction of dephasing

$$\langle \hat{\sigma}_- \rangle = \frac{ig\sqrt{\kappa_{in}}}{\tilde{\gamma}_d\tilde{\kappa}\left(1 + \frac{g^2}{\tilde{\gamma}_d\tilde{\kappa}}\right)}\langle \hat{a}_{in} \rangle. \tag{4.55}$$

We can follow a similar set of steps for the reflection spectrum. For simplicity, we will consider the case where we are on-resonance ($\Delta_c = \Delta_a = 0$). The cavity field in this case is given by

$$\hat{a} = \frac{-ig\hat{\sigma}_- - \sqrt{\kappa_{in}}\hat{a}_{in}}{\kappa/2} \tag{4.56}$$

so that

$$\hat{a}_{out} = \hat{a}_{in} + \frac{-ig\hat{\sigma}_- - \sqrt{\kappa_{in}}\hat{a}_{in}}{\kappa/2}. \tag{4.57}$$

The reflected power on resonance is then

$$|r(0)|^2 = \langle \hat{a}^\dagger_{out}\hat{a}_{out}\rangle = \left|\hat{a}_{in} + \frac{-ig\hat{\sigma}_- - \sqrt{\kappa_{in}}\hat{a}_{in}}{\kappa/2}\right|^2 \tag{4.58}$$

$$= |\hat{a}_{in}|^2\left(1 - 2\frac{\kappa_{in}}{\kappa}\right)^2 + 4\frac{\hat{a}_{in}}{\kappa}g\sqrt{\kappa_{in}}\,\mathrm{Im}\{\rho_{21}\} \tag{4.59}$$

$$+ \frac{4\kappa_{in}}{\kappa^2}\left(g^2\rho_{22} - 2\sqrt{\kappa_{in}}\hat{a}_{in}g\,\mathrm{Im}\{\rho_{21}\}\right).$$

It is then left as an exercise to the reader [7] to show that this can be written as

$$|r(0)|^2 = \frac{(1+\eta_d)(1+\eta_s) - 4(1+\eta_s)\kappa_{in}/\kappa + (1+\eta_s-\eta_d)(2\kappa_{in}/\kappa)^2}{(1+\eta_d)\,(1+\eta_s)}, \tag{4.60}$$

where $\eta_d = 2g^2/\gamma_d\kappa$ and $\eta_s = 4g^2/\gamma\kappa$. We see that in the case of no atom ($\eta_d = \eta_s = 0$), this reduces to the expected expression for the empty cavity. We also see that for the case of no excess dephasing $\eta_d = \eta_s$, we recover the original expression as the initial treatment in Eq. (4.45).

We plot the predictions of the reconciled semi-classical formula against the simulations of the system using the master equation formalism for achievable system parameters. This is shown in Fig. 4.3, where we see excellent agreement between the simulated spectrum and the corrected semi-classical prediction.

It is worth restating that these corrected expressions are all in the low-excitation limit. Once we move out of this limit, the calculations become substantially more involved as we cannot make the same nice approximations (e.g. separating the expectation values of field and atom). The atom behaves as expected under saturation, but the photon statistics of the reflected and transmitted signal (i.e. the cavity field)

[7] Substitute Eq. (4.55) and Eq. (4.55) into Eq. (4.59) and simplify. The use of Mathematica is allowed and encouraged.

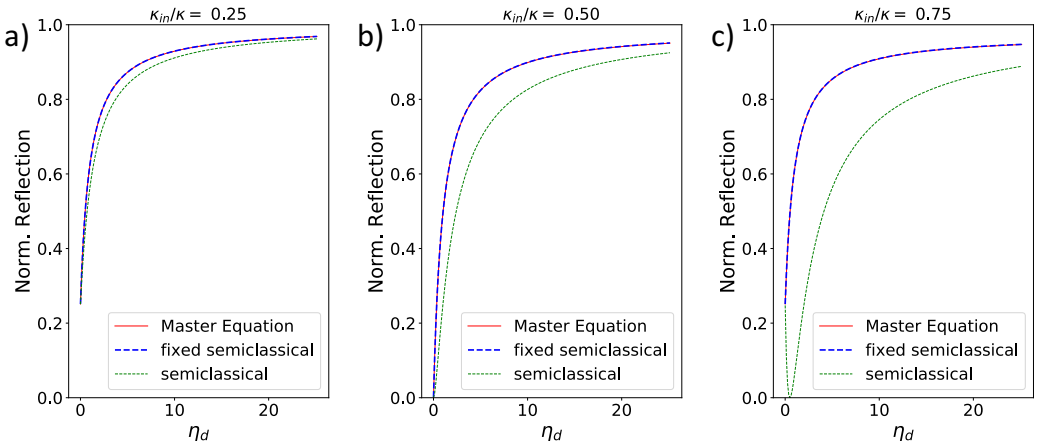

Figure 4.3: The reflection spectrum on resonance ($|r(0)|^2$) as a function of η_d for the corrected semi-classical expression Eq. (4.60) compared to results of master equation simulation and original semiclassical expression Eq. (4.45). Here I am using the same parameters as in Fig. 4.2: $g = 2\pi \times 20$ MHZ, $\kappa = 2\pi \times 30$ GHz, $1/\gamma = 267\mu$s, for three different cavity input coupling rates.

must be treated more rigorously. Analytic expressions can be derived in this regime (e.g. [106] or the supplementary material of [14]), but numerical approaches to this problem become an especially attractive option (especially in the presence of excess dephasing).

4.5 What do we expect to be able to achieve?

Let us then look at what we expect to achieve in ^{171}Yb:YVO_4 with typical nanobeam devices. First, we consider the single photon Rabi frequency:

$$g = \frac{\mu}{\hbar}\sqrt{\frac{\hbar\omega}{2\epsilon_0 n^2 V}}. \tag{4.61}$$

The value of the dipole moment can be extracted from the absorption measurements in Chapter 3 (see e.g. [89]). One potential sticky point here is that in going from the measured absorption to the dipole moment there is a choice of which (if any) local field correction (LFC) factor to use. In addition to the macroscopic correction to the electric field in the medium (n), this correction accounts for the change in the electric field felt by the emitter due to its microscopic environment. Within the rare-earth literature [22, 89], the standard LFC is the Lorentz or virtual cavity model $\chi_{vc} = (n^2+2)/3$. As discussed in [116], this has been observed to be a good correction factor in pure systems with one type of atom or molecule. An alternative

LFC is the empty-cavity or real cavity correction factor $\chi_{rc} = (3n^2)/(2n^2+1)$. This correction factor has been suggested by [116, 117] to in fact be the better choice for substitutional impurity atoms in dielectric hosts (e.g. rare-earths in crystal hosts). In addition to the question of which local field correction to use, there is also the question of whether g should be modified to include such a local-field correction (i.e.$\mu \rightarrow \mu\chi$). The work of [118] would suggest that it should not be included, but it is not clear whether this reading is correct at the present time.

In the end, the choice of local field correction will result in differing values for the dipole moment and the resulting Rabi frequency used in the above formula. It should be noted that a result of excluding the LFC in the definition for g while including it in the expression for the spontaneous emission rate γ is that the expression for the Purcell factor in Eq. (4.26) should then be multiplied by $1/\chi^2$. I will not try to resolve this LFC problem here, but will present the predictions of these different approaches and show they all give roughly the same results.

For now, I will take the approach of including the local field correction factor in the definition of g. In a sense this is equivalent to disregarding the LFC factor from the beginning as the choice of LFC in calculating the dipole moment from the absorption measurement will cancel out in the expression for the Purcell factor. In this case, the dipole moment extracted from the absorption measurements is $\mu = 14.4 \times 10^{-32}$Cm. The mode volume of the nanobeam resonator extracted from FDTD simulations is $0.095\mu\text{m}^3 \approx 1(\lambda/n)^3$, where here $n = 2.17$ is the refractive index of YVO for $E \parallel c$. This corresponds to $g = 2\pi \times 34.6$ MHz for the maximally coupled ion. Assuming a cavity with $Q = 10^4$, the corresponding Purcell enhancement is $4g^2/\kappa\gamma = \beta F_p = 263$. Here, $\beta = 0.36$ is the branching ratio for the transition with $E \parallel c$ out of all possible transitions. The corresponding cavity enhanced lifetime is then $T_1 = 1\ \mu s$ and the emission fraction into the cavity mode is $P_{cav} = \beta F_p/(1 + \beta F_p) = 0.996$.

In Table 4.1, I summarize the predicted values for the different choices of local field correction used to calculate the dipole moment assuming a cavity with $Q = 10^4$. These are the predictions given if the LFC is not included in the definition of g Eq. (4.61). If the LFC is included in the definition of g, then all choices of LFC will give the same values as the "No LFC" case for the observables g, F_p, T_1, and P_{cav}.

Table 4.1: Table of expected system parameters for the Yb:YVO system assuming $Q = 10^4$ and $V \approx 1(\lambda/n)^3$ as described in text assuming different local field correction factors in extracting the dipole moment from the absorption measurements. These predictions are the best case scenario in which we assume an ion maximally coupled and aligned to the cavity mode.

	No LFC	Real Cavity	Virtual Cavity	Units
f_{21}	8.8	4.8	1.8	10^{-6}
μ	14.4	10.6	6.4	10^{-32} C m
$g/(2\pi)$	34.6	25.5	15.4	MHz
βF_p ($Q = 10^4$)	263	143	53	
T_1^{cav} ($Q = 10^4$)	1.0	1.9	5.0	μs
P_{cav}	0.996	0.993	0.981	

Chapter 5

EXPERIMENTAL SETUP FOR SINGLE ION WORK

The experimental setup in the Faraon Lab has rapidly evolved in size and complexity since its inception in 2012, but it can be distilled to a few basic ingredients.

First, we need an ion and host material. For the measurements in the next two chapters, we will work with ytterbium doped in the YVO host crystal. The properties of this material were discussed in Chapter 3. My initial work in the group focused primarily on neodymium doped in YSO and YVO hosts, which provided the foundation for current measurements in ytterbium. There is also ongoing research in the Faraon group pursuing a similar set of goals with materials doped with erbium, which have optical transitions in the telecom range. These experiments all rely on a similar apparatus, with the main difference being the frequencies of the lasers involved and the corresponding changes to the optical components used.

We couple the ions to nanophotonic resonators to enhance their emission rate and probe the physics described in the previous chapters. The measurements presented here use the triangular nanobeam photonic crystal resonators described in the introduction.

These devices must be cooled to cryogenic temperatures (<4 K) to enhance the coherence properties of the ions. Generally speaking, the colder the better. The experiments are carried out in cryostats and dilution refrigerators that allow us to cool the devices to temperatures of < 50 mK.

We address and readout the optical transitions of the ions using narrowband lasers. These lasers are coupled to the device in the dilution refrigerator through a fiber optic network. Photons leaving the cavity are measured using high-efficiency, low-dark-count single photon detectors. We address electron and nuclear spin transitions of the ions using a microwave waveguide fabricated next to the nanobeam device.

In this chapter, I will give an overview of these various components in their current form as used for detection and manipulation of single Yb ions coupled to nanocavity. This setup represents the culmination of efforts to date and as such most of the earlier measurements in the lab have involved some subset of or variation on the described configuration.

5.1 Sample

For measurements involving single ions, we generally want the lowest concentration of ions possible to minimize ion-ion interactions that can have a detrimental effect on the coherence lifetimes [94]. The caveat is that we want to make sure this concentration is high enough to ensure a high probability of having well-coupled ions in the cavity. We do not have spatial selectivity of ions in the cavity, and thus we rely on natural inhomogeneous broadening of transition frequencies within the crystal host to isolate single ions in frequency space. To find an isolated single ion in higher doping samples, we move to the tails of the inhomogeneous distribution until the ion density becomes less than a single ion per homogeneous linewidth.

The measurements described in the following two chapters were performed in a nominally undoped sample of YVO cut from a boule custom grown by Gamdan Optics. We had samples cut and polished from this boule by Brand Laser Optics. For device fabrication, we typically work with 2.5 x 2.5 x 0.5 mm c-cut samples. An initial measure of the Yb concentration in this boule was done using secondary ion mass spectrometry (SIMS) alongside the work described in Chapter 3, which we were fortunate enough to be able to do with the assistance of Dr. Yunbin Guan at the Caltech Microanalysis Center. From these measurements, we estimate an upperbound on the total concentration of Yb in this device to be 15 ppm. Assuming natural isotopic abundance, this corresponds to a Yb-171 concentration of 2 ppm. In contrast, the concentration of neodymium in this sample is estimated to be < 0.2 ppm. It is worth noting that SIMS measurements can lose accuracy at concentrations this low, so these numbers should be taken as an upperbound [50]. At this point, we are not sure why the residual level of ytterbium ions is so much higher in this crystal compared to other rare-earths as we do not have control or information on the full growth process. Absorption spectroscopy in large bulk crystals of this material is currently being revisited to verify this concentration, but we could also explore other methods that are more reliable than SIMS for small concentrations such as GDMS (glow discharge mass spectrometry) [50].

Following recommendations by Dr. Charles Thiel from MSU, we are currently investigating crystals from other sources in an effort to find samples with lower doping concentrations. Ultimately, if we can find ultra-pure samples, we might run into the issue of not being able to find ions in the device. One option in this case would be to pursue ion implantation techniques. This is used often in the diamond community [14, 119]. While this has not been pursued as of yet in the Faraon

group, a few groups have shown success with similar techniques with rare-earth ions [49, 120]. The open question here would be whether the the implanted ions retain the same coherence properties as the doped-as-grown ions.

5.2 Triangular nanobeam photonic crystal resonators in YVO

A set of triangular nanobeam photonic crystal resonators were fabricated in this sample using the focused ion beam (FIB) as described in the introduction. As I was primarily involved in the measurement of these devices and not the fabrication, I will refer the interested reader to [51, 53] for further details on how these devices are made. These devices were fabricated in a *c*-cut sample with a fundamental TM mode aligned with the c-axis of the crystal, which as described in Chapter 3 is the direction of the stronger optical transition. An added advantage of this configuration is that the strong transitions are not allowed for light incident perpendicular to the surface, which reduces background contributions from the bulk crystal.

Images of the cavity used for the measurements are shown in Fig. 5.1. A gold coplanar waveguide was fabricated next to the device to allow for microwave manipulation of the ions in the optical cavity. Launching microwaves through these devices gives rise to an oscillating magnetic field along the *c*-axis of the crystal, which is the desired configuration for driving the microwave transitions of the Yb-171 isotope at zero field. The center strip of this waveguide was 60 μm wide with a spacing of 30 μm to the ground plane. This relatively wide gap was chosen to

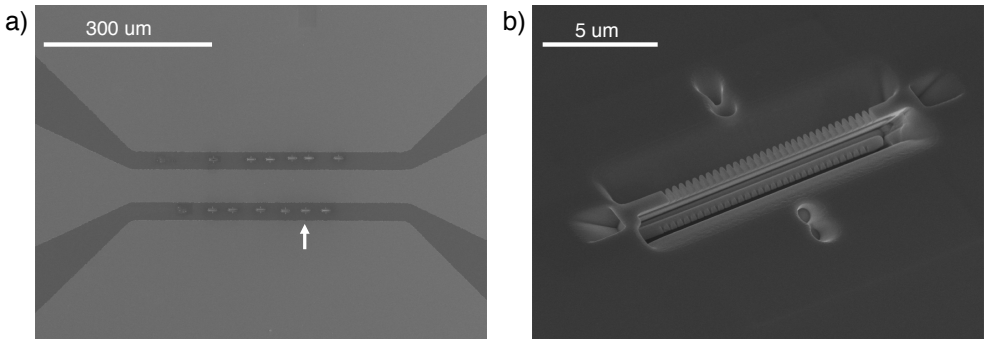

Figure 5.1: SEM images of device used for measurement. a) Large scale image of chip showing an array of nanobeam resonators fabricated in YVO surface. These cavities sit in the gap of a coplanar microwave waveguide, which is the light gray surface. Arrow points to the device used for these measurements. b) Higher resolution image of nanobeam used for the measurements.

ensure that it did not interfere with the fabrication of the nanobeams on this first set of devices, but future devices could reduce this spacing to achieve higher field strength. The microwave strip lines were fabricated from gold to offer the most flexibility with respect to magnetic field configurations, but future devices will explore the use of cavities and superconducting materials to reduce resistive heating.

A reflection spectrum for this device is shown in Fig. 5.2. We extract a linewidth (FWHM) of $\kappa = 2\pi\times30.7$ GHz, which corresponds to a quality factor for this cavity of $Q = \omega/\kappa = 9.9 \times 10^3$. This cavity was designed to be one-sided by reducing the number of cuts on the input mirror, but ended up being quite undercoupled with a measured $\kappa_{in}/\kappa \approx 0.12$. While this severely limits the attainable collection efficiencies, we tried to push the experiment as far as possible with this device. In previous devices, we have achieved up to $\kappa_{in}/\kappa \sim 0.4$ and have a promising set of new devices that look to be in this range.[1] Light is sent into and out of the device through total internal reflection by focusing onto 45 degree couplers milled on either side of the cavity. The coupling efficiency with this method is limited by the size of the focal spot we can achieve. For the configuration in the dilution refrigerator that will be described shortly, this mode-matching is limited to $\sim 24\%$. This value is determined by measuring the reflection of the cavity far from resonance.

These two coupling rates impose an upper-bound on the collection efficiency in this device of $\sim 3\%$. While this coupling efficiency was high enough to pursue initial demonstrations in this device, future measurements and more advanced demonstrations will benefit greatly from an increase in this efficiency by exploring other coupling methods or alternative device designs. One attractive option would be pursuing a hybrid fabrication platform similar to [50] to allow for direct fiber coupling to the devices. Early research in the group by Evan Miyazono pursued such a hybrid platform for devices at neodymium wavelengths [51] and we are in the process of reviving these efforts for ytterbium devices.

An aside on how to determine whether the device is over- or under-coupled

A common question that arises in the reflection spectrum measurements is whether the device is over ($\kappa_{in}/\kappa > 0.5$) or undercoupled ($\kappa_{in}/\kappa < 0.5$). We are measuring

[1] Indeed, on the same chip as the one used for the measurements presented here, there were originally a few other promising cavities that were destroyed due to an unfortunate accident caused by the author in mounting the sample.

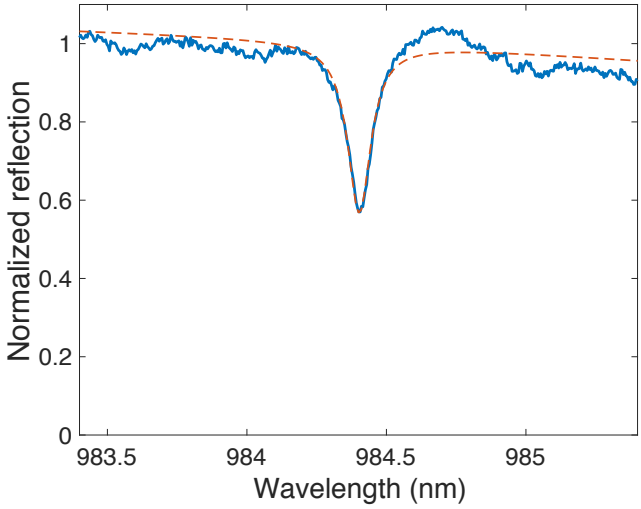

Figure 5.2: Reflection spectrum of device used for measurements presented in following chapters as measured on the spectrometer. Lorentzian fit gives FWHM of $\kappa = 2\pi.7$ GHz ($Q = 9.9 \times 10^3$) and $\kappa_{in}/\kappa = 0.12$.

the reflected power spectrum, which we saw earlier (see Ch. 4.2) takes the form :

$$|r(\Delta_c)|^2 = \frac{(\kappa_{in} - \kappa/2)^2 + \Delta_c^2}{(\kappa/2)^2 + \Delta_c^2}. \tag{5.1}$$

From this we see that we cannot distinguish between these two cases directly from the power measurement (e.g. $\kappa_{in}/\kappa = 0.1$ and $\kappa_{in}/\kappa = 0.9$ will give the same result). To distinguish between these two cases we can instead measure the phase response across the cavity, which will behave differently for over and undercoupled cavities. We opted to measure this phase using a polarization interferometer similar to the setup described in [104].[2] In contrast to the setup described there, we performed this measurement in free-space by incorporating the necessary interferometer optics into the confocal microscope setup. Because we do not have a laser that can quickly scan over the entire range of the cavity, we measured the reflection spectrum of the device on the spectrometer using a broadband source. We coupled the two output

[2]Another straightforward way to do this is by imposing sidebands on the probe laser with an electro-optic modulator and scanning this sideband across the cavity resonance. By measuring the phase of this reflected sideband using a fast photodetector and vector network analyzer, one can then determine whether the cavity is over- or under-coupled (See e.g. [121]). The current cavities are wide compared to what is achievable with the network analyzers and mode-hop free scan range of the lasers available in our lab, so we did not pursue this approach in the current device. This method will be a simpler option for devices with narrower linewidths in the future.

paths of the interferometer into single mode fibers and quickly alternated between these two signals with a MEMS switch to achieve the differential signal necessary to extract κ_{in}/κ. From these measurements we determine the device is undercoupled with $\kappa_{in}/\kappa \approx 0.12$.

Sample mounting

The devices are mounted to a copper sample holder using silver paint (Pelco 16062). Early measurements in the group mounted the device with indium solder, but we find the silver paint to be a more convenient mounting technique with no noticeable differences in thermal properties. The device sits inside a microwave launch board (Rogers AD1000, fabricated by Hughes Circuits) with SMP connectors on both input and output. This launch board is wire-bonded to the gold stripline on the surface of the device with as many wirebonds as possible to give additional cooling through the surface. This sample holder was designed to enable straightforward exchange between measurements in the different cryostats without the added stress (primarily to the experimenter) involved in remounting the chip. Fig. 5.3 is a picture of the mounted sample inside the dilution fridge setup.

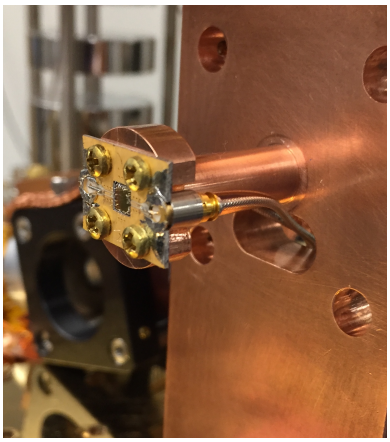

Figure 5.3: Image of sample mount used inside Bluefors dilution refrigerator. The sample is mounted to the copper holder with silver paint and wire-bonded to microwave launch board.

5.3 Montana Cryostat

Initial measurements and characterizations of this device were performed in a Montana Instruments Cryostation. This is a closed-cycle He^4 system with base temperature of ~ 3.6 K. We couple into the device using a home-built confocal microscope setup as shown in Fig. 5.4. We are using the castle option, which allows for op-

tical access of the device with a high-NA objective (Olympus LCPlan N 50x, NA = 0.65) and allows for high magnetic fields (~ 500 mT) at the device using large permanent magnets outside the cryostat. A nitrogen line was incorporated into the castle to allow for tuning of the device through gas condensation. This cryostat was the workhorse for much of the earlier work in neodymium before the acquisition of the Bluefors systems.

This system has a quick cooldown (<4 hours) and warmup (2 hours) cycle that allows for quick iteration and development without interrupting other experiments occurring in the dilution fridge. In contrast, the fully-loaded dilution fridge takes at least 24 hours to get to base and 12 hours to warm-up. While we need to go to lower temperatures than 4 K to achieve good coherence properties from these ions, the elevated temperature served as an advantage for initial measurements in that it ensured that we were not optically pumping ions to other spin states. This simplifies the experimental apparatus substantially and allowed us to find single ions and develop confidence with the measurements before moving to the Bluefors setup.

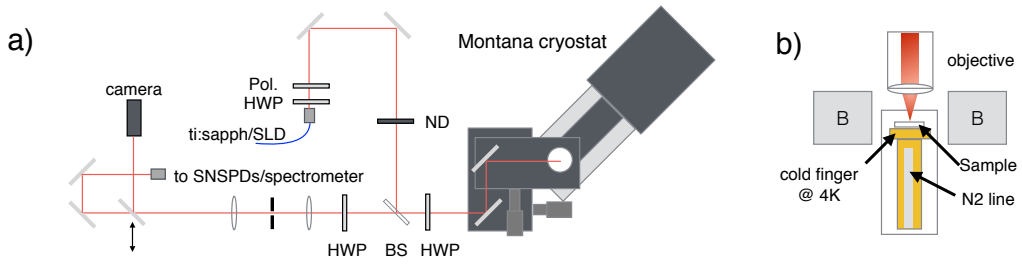

Figure 5.4: a) Simplified optical schematic of confocal microscope setup used with Montana cryostat. b) Layout of measurement inside the castle option of the Montana cryostat.

5.4 Bluefors Dilution Refrigerator

After initial measurements in the Montana, the device was moved to the Bluefors LD-250 dilution refrigerator, often referred to within the lab as “Bluefors 1.0". This system was originally installed near the end of 2015 as a He^3 fridge, which allowed for measurements down to ~ 400 mK. In the summer of 2017, this was upgraded to a full dilution fridge with a base temperature of ~ 10 mK completely empty. Since this upgrade, the fridge has been moved into a new lab alongside a second new dilution fridge, which we have creatively named "Bluefors 2.0". This fridge has a

larger pulse tube to give the cooling power necessary to a incorporate a 6/1/1 vector magnet into this system (at the time of writing this thesis, we had just received this magnet and have yet to install it). A simplified schematic of the current measurement setup for the singles experiment inside Bluefors 1.0 is shown in Fig. 5.5. In this section, I will highlight the salient details of this configuration.

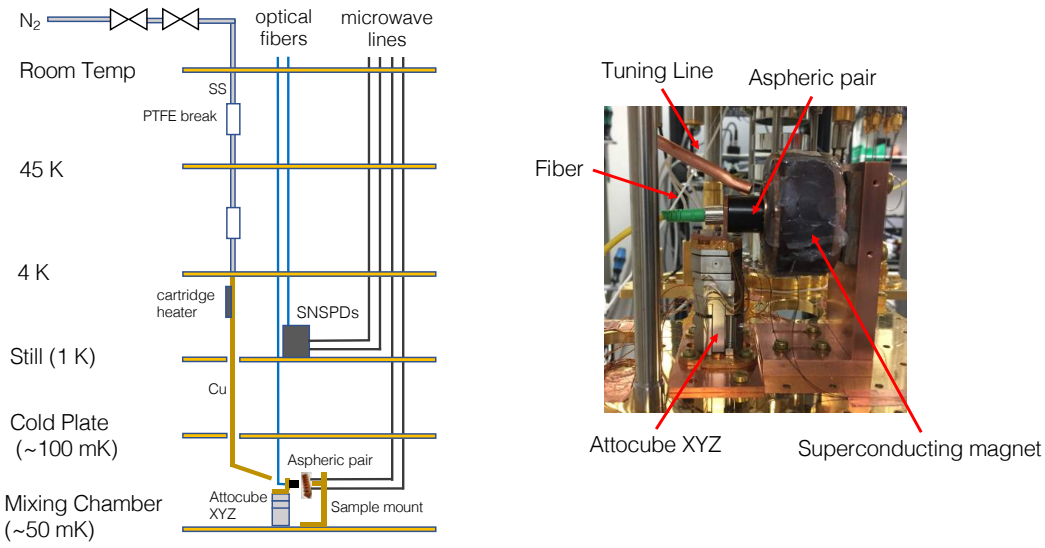

Figure 5.5: a) Layout of singles experiment in the Bluefors showing configuration of tuning line (silver and brown), optical fibers (blue), and coaxial lines (black). b) Image of setup used to couple to devices inside the Bluefors with relevant components labeled.

To run optical experiments inside the fridge, we route optical fibers through a home-built epoxy feedthrough at the top of the fridge. Details of this construction are included in [51].[3] For experiments at neodymium and ytterbium wavelengths, we find the 780 HP fiber to be a convenient choice. Depending on the experiment, these fibers are then spliced to connectors (typically anti-reflection coated FC/APC connectors) inside the fridge before being launched into free space and coupled to the device. Initially, the fibers are all connectorized on the outside of the fridge to enable flexibility in measurements. After experiments are up and running in a

[3] In Bluefors 1.0, we were perhaps overly ambitious and started with 40 fibers inside the fridge for measurements at a variety of wavelengths in different materials. While quite cumbersome in terms of organization, this allows us to run many different experiments during a given cooldown and the extra fibers have proven to be useful as spares whenever a fiber breaks. For Bluefors 2.0, we were slightly less ambitious and cut back to a more modest 24 fibers.

dedicated measurement setup, these fibers connections are instead spliced to avoid additional losses and reflections inherent to fiber-fiber interfaces.

Measurements of the devices take place on the mixing chamber plate. The current setup for optical coupling to the Yb devices is shown in Fig. 5.5b. We couple light from fiber to the device using an aspheric lens doublet mounted on an Attocube XYZ stack (ANPx101 for the X and Y axes, ANPz102 for the Z axis). These allow for $\sim$ 5 mm of travel with fine resolution, which we can use to align to the device that is held stationary on the copper mount shown in Fig. 5.3. Coarse alignment is most easily accomplished by sending in a red laser (a fiber fault checker is a useful tool for this) and visually checking we are centered on the part of the chip containing the devices. We then measure the reflected power from the chip and scan the Attocubes to focus on the surface. We can scan along the surface to create a map of the devices and compare to the room-temperature images of the chip. The gold striplines on the surface serve as useful alignment references for this task. Once the devices are identified, we then focus on the couplers and maximize the alignment and optical polarization from the measured reflection spectrum on the spectrometer. The Attocubes are typically quite sluggish at cryogenic temperatures, so this initial alignment is most readily accomplished at room temperature and then monitored and adjusted during the cooldown. Before condensing the helium mixture, we turn off the resistive readout of the Attocube position to avoid heating the fridge (leaving the resistive readout on typically heats up the MXC plate to $\sim$ 100 mK) and perform further alignment in the dark based on the reflection spectrum.

Electrical and RF wiring

Bluefors 1.0 currently has 4 coaxial lines running from room temperature to various stages within the fridge. In the current configuration, two of these are used for the input and output of the microwave stripline and two are used to bias and readout superconducting nanowire single photon detectors mounted on the 1 K plate. These coaxial lines are the standard installation set from Bluefors. The inner conductor of these lines are thermalized at each stage cryogenic attenuators, which range from 0 dB to 20 dB depending on the goal of the experiment (see Fig. 5.8). In addition to the coaxial lines, we currently have two sets of 24 DC lines to drive the Attocubes, which are the standard wiring harness for this task from Bluefors. This allows us to run two independent experiments coupling to nanodevices in Bluefors 1.0, with one Attocube devoted to Yb measurements and the other devoted to Er measurements. An additional set of DC lines runs to the heaters used for the gas tuning.

Gas tuning of devices

Devices are tuned onto resonance with the ion transition of interest by nitrogen deposition [54]. To implement this in the Bluefors, we run a gas line from room temperature down to the mixing chamber. This gas line consists of stainless steel tubing from room temperature to 4 K with the tubing thermalized at each stage and isolated between stages by a PTFE break. The tuning line is then clamped to the 4 K plate. From 4 K to the mixing chamber plate, the tuning line consists of a free-hanging copper tube that is thermally isolated from the components below 4 K. The output of this line is directed onto the sample on the mixing chamber plate. A resistive heater is attached to the tuning line near the 4 K stage to allow us to warm up the line enough such that gas flows through the line without freezing.

The current recipe for tuning is as follows: we start with room temperature input line pressurized to 2 Bar with ultra-pure nitrogen. We next pressurize a small chamber formed between two input valves, and release this volume into the tuning line in the fridge. We repeat this for a total of two chambers of gas. This gas will freeze in the line upon entry and will not lead to any noticeable tuning. With the fridge at 4 K (before condensing the helium mixture), we then heat up the tuning line while monitoring the temperature of the plates in the fridge. For initial installation, we did not have an extra temperature sensor available for these measurements, but this would be useful for future experimenters. As the tuning line is warmed up with a resistive heater ($\sim$ 5 W), the frozen nitrogen in the line thaws and begins to flow and deposit onto the device. The resulting tuning of device typically starts to become noticeable when the 4 K plate gets to around 14 K. By careful adjustment of the heater power to maintain this temperature, one can reliably get the tuning rate down to < 0.1 nm/minute. After turning off the heater, the gas line then cools back down to 4 K such that the nitrogen refreezes in the line and stops the tuning. Tuning at such slow rates takes a lot of patience to get it exactly on resonance this way, especially allowing for the time it takes for the tuning line to cooldown after turning off the heater. Instead we usually intentionally overtune the device by around 0.5 nm and tune back onto resonance by boiling off some of the frozen nitrogen through optical heating of the device. Sending in laser powers around 100 uW on resonance with the device will heat the device and detune until the cavity is back out of resonance with the laser. By monitoring the cavity reflection on the spectrometer as we step the laser in into resonance with the cavity, we can then tune the cavity to the desired frequency.

Magnetic fields

We apply magnetic fields to the device in the fridge using a set of homebuilt superconducting magnets. These are made by winding superconducting wire (SC-T48B-M-0.254mm, Supercon Inc) onto various formers in the sizes and shapes necessary to achieve the desired field configuration for a given measurement. These magnets are driven by high-current magnet supplies from Oxford or American Magnetics. The magnet leads enter the fridge and go through high T_c superconducting leads between the 45 K and 4 K plate with the standard magnet wiring apparatus installed by Bluefors. We attach the homebuilt magnet leads at the 4 K and thermally lag these leads on the way down to the experiment on the mixing chamber plate.

At the time of writing, we have recently received a 6/1/1 magnet system from American Magnetics that will be incorporated into Bluefors 2.0. While not necessary for the low-field measurements in the current device, this will be useful for achieving high-stability magnetic fields in arbitrary directions. For Kramers ions, such as erbium and ytterbium, the high field regime is interesting because it allows us to freeze out electron spins which are typically a dominant source of decoherence. This technique has enabled long optical and nuclear spin coherence times in Kramers ions [65, 94]. At the moment the plan is for the erbium measurements to move into this magnet, but one could envision singles measurements moving into this magnet if the high-field regime proves to be a better option. At present time, we have also installed a set of room temperature magnet coils that sit outside the fridge for further nulling of earth's magnetic field without warming up the fridge to install another set of magnets. These are made using 12 AWG wire, which has a current handling capacity of 20 A. We can use these to achieve modest fields of a few Gauss at the devices.

During a cooldown, we typically run other experiments with bulk crystals on the 1 K stage of the fridge. These take various forms, but typically rely on a Thorlabs u-bench setup with various magnets integrated depending on the question to be answered in the measurements.

With all of this installed, we achieve base temperatures at the mixing chamber plate of around 40 mK (compared to the initial base temperature of 10 mK with the fridge completely empty). One big advantage of working in the dilution fridge is the stability of the tuning and optical alignment. With the described tuning technique, we do not notice any change in the tuning over the course of months of measurement. Optical alignment is also remarkably stable. This is in contrast to the optical alignment

of the Montana setup, which is currently at the mercy of temperature fluctuations in the room. We notice small drifts on the polarization alignment on the few week time scale, but typically the optical alignment does not need to be adjusted unless the Bluefors has been shaken (e.g. someone runs into it in the dark). For the low count rates in the system, this is essential to make sure that we can reliably collect data sets that might take hours to acquire. In this way, measurements can reliably be taken for weeks on end without much adjustment. The length of cooldowns is largely determined by the kindness and patience of other lab members waiting to run their own experiments, but also in part by the cruel hand of fate in the form of campus-wide power glitches or failures of the water chilling system.

5.5 Optical setup

A simplified diagram of the optical setup is shown in Fig. 5.6 In short, light from a variety of different sources goes through a variety of modulators and controllers before being sent to the sample inside the fridge via optical fiber. All these sources are combined through a network of fiber optic components to allow us to perform measurements on the devices. We add in appropriate amplitude and polarization control along the path with various pickoffs that allow us to monitor the input powers and pulses. The light reflected or emitted from the device is sent to a single photon detector for measurements of the ion emission or to a spectrometer for characterization and alignment of the cavity. In this section, I will provide details on the individual components of interest in this setup.

Ti:Sapphire

The workhorse laser for the ytterbium and neodymium measurements is a continuous-wave Ti:Sapphire laser (Solstis from M Squared). This laser is pumped by a 15 W 532 nm DPSS laser (Sprout from Lighthouse Photonics). The Ti:Sapph is broadly tunable from 700 nm to 1000 nm, so can be used for measurements in Nd (880 nm) and Yb (980 nm) materials without too much realigning or swapping of optics. Typically we run the pump at a power of 10 W, which gives around 500 mW at 984 nm. This is more than enough for measurements in the nanocavities (in which we are typically sending in less than a nW of power to the devices), but allows us to split the light off into many paths, insert a variety of optical components, and overcome other losses on the way to the device with plenty of power to spare. This extra power is also useful for measurements in bulk crystals, where achieving the

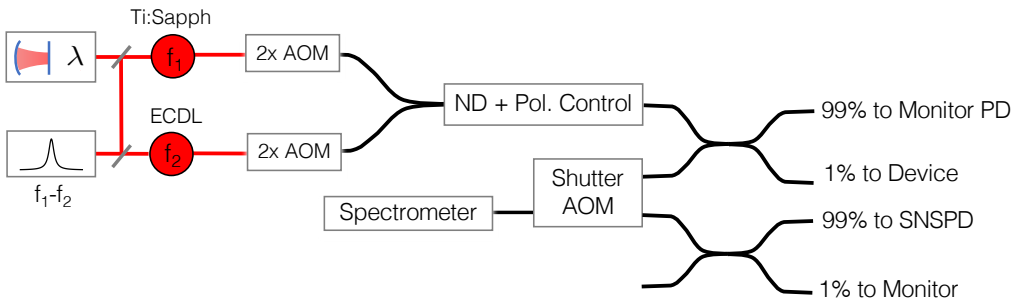

Figure 5.6: Schematic of optical network used for measurements of single ions. We use two lasers in the experiment. The Ti:Sapph is locked to the an external reference cavity and monitored with a wavemeter. The ECDL is offset-frequency locked to the Ti:Sapph. Both lasers go through two sets of double-pass AOMs before being coupled into fiber and combined by a 50/50 fiber splitter. They then travel through neutral density filters for power adjustment and a polarization controller before being sent to the device through a 1/99 fiber splitter. The light exiting the cavity goes through a free-space AOM that serves as a shutter before being coupled to SNSPD. A flip mirror allows the light reflected from the cavity to be sent to spectrometer for device tuning and characterization.

Rabi frequencies necessary to coherently drive the optical transitions requires substantially more power.

One advantage of this laser aside from the high output power and wide range tunability is that it is intrinsically quite stable in the sense of free-running linewidth and long-term drift. Our model of the Solstis has an in-built reference cavity designed to improve this stability further. The long-term drift of this cavity was stable enough for measurements early on in the lab when we were working with ensembles with inhomogeneous lines in the few to tens of GHz range. As we have moved to narrower inhomogeneous linewidths and now measurements of single ions, we require further stabilization to overcome the thermal drift of this reference cavity as will be detailed shortly.

The output of the Ti:Sapph is split into a few paths. On the "low power path", a small fraction of this light is sent through two sets of double-pass acousto-optic modulators (AOMs) before being coupled into fiber and sent to the experiment. For this purpose we use 200 MHz modulators (Isomet 1250c-1 and 1250c-2), which allows us to generate pulses with rise times down to around 15 ns. We typically get an extinction of around 60 dB per double-pass when things are well aligned and clean (reflections due to dust on optics can quickly kill this extinction). The 120

dB of total extinction all told helps ensure we are not limited by leakage counts on the measurements in the device. The AOMs have been driven with a variety of sources as the experiments have evolved. Most measurements now rely on the stability of the readout frequencies, so we use fixed frequency sources that go through switches and amplifers from Minicircuits (typically the ZASWA-50DR and a 2 W amplifier). The two AOMs can be most easily aligned in time to account for delays in the driving electronics by translating the AOMs perpendicular to the beam path. Indeed this is a more convenient way to account for the time difference compared to introducing additional electronic delays. The rest of the light is sent to the "high power path." This path is used for bulk measurements and used to heat the devices when we need to tune them back on resonance. A small fraction of light from this path is split off and coupled to fiber sent to a wavemeter and to the locking setups. This whole setup is enclosed in a nice big aluminum box (the current iteration was built by Andrei Ruskuc, our resident box expert) to keep the laser protected from the rest of the lab and vice versa.

Homebuilt ECDL

For initial investigations of Yb:YVO, we wanted to perform measurements in parallel to the measurements in progress at the time in Nd:YVO. We also did not want to swap back and forth between wavelengths from day to day. For this purpose, I built an external cavity diode laser based on the design presented in [82]. This is based on a unibody aluminum housing, which we had fabricated by the University of Oregon machine shop. This is based on a simple Littrow design using a Thorlabs 980 nm diode. It is not very powerful ($\sim$ 2 mW), but works pretty well for the purpose of basic spectroscopy. Detailed documentation on how to build such a laser can be found in [82] and references therein. The main modification to the design was redesigning the diode housing mount to access the Littrow angle necessary to reconcile the desired wavelength with the diffraction gratings available from Richardson gratings. We use a simple feed-forward circuit to feedback to the current control while the piezo is scanned, which allows for up to a 40 GHz mode-hop-free scan range. This wide scan range was especially useful for the magnetic field ramps presented in Chapter 3 without stitching together multiple scans.

This laser was used in conjunction with the Ti:Sapph for the initial two-laser experiments in the device. In this case, we lacked the optical power necessary to both lock the two lasers together and account for the losses in the double-pass AOM setups.

To overcome this, we introduced an optical amplifier into the path. While this gave plenty of power, the amplifier also introduced additional noise back into the laser that caused instability on the diode. For the most part, this was overcome with an additional fiber isolator and a narrowband optical filter in the path.

Toptica ECDL

After demonstrating that the two-tone experiments were worth pursuing further, we switched to using a TOPTICA DLpro for the second tone. This laser was originally purchased with an operating wavelength of 880 nm and was used for Nd:YVO measurements. After deciding that it would be useful for the Yb measurements, we sent it back and had the diode changed to allow for operation at 984 nm. This diode outputs more than 100 mW at 984 nm, which simplifies the experimental setup and is on the whole a much more user-friendly system than the home-built laser. The output of this laser is split into two paths. One path goes through two sets of double-pass AOMs before being coupled into fiber. It is then combined with the output of the low power path of the Ti:Sapph and sent to the device. The other path of the laser is sent to the offset-locking setup described below.

Laser stabilization

For the singles experiments, we want the absolute long-term drift of the laser to be as small as possible. The internal reference of the Ti:Sapph showed significant long term drift (100s of MHz over the course of a day) and as such is not stable enough for our purposes. As we are working with linewidths on the order of 100 kHz, this makes it difficult to reliably and repeatedly address a single ion.

For this purpose, we lock the Ti:Sapph to an external reference cavity made by Stable Laser Systems (SLS). This cavity has a FSR of 1.5 GHz, with mirror coatings that give a finesse of > 50 k at the design wavelength of 880 nm. While designed for the Nd measurements, we can still use this cavity at 980 nm where the finesse is reduced to around 1000.[4] The cavity is made of an ultra-low expansion mate-

[4] We are primarily focused on absolute stability, so this reduced finesse will effect the narrowest achievable linewidth in this system. At present time, we estimate this linewidth to be < 10 kHz. This linewidth is much lower than the Rabi frequency of the optical excitation pulses, so will not present a significant issue for many of the current pulsed measurements. However, if the linewidth is significantly worse than estimated, it could start have a detrimental effect on e.g. the Ramsey measurements of optical coherence. We now have another SLS cavity in the lab that has mirror coatings better suited for this wavelength that we could hope to use if or when this linewidth becomes and issue for us. Ultimately the achievable linewidths in the system will be limited to the kHz level due to the fiber network without active fiber noise compensation [122]. Future measurements will

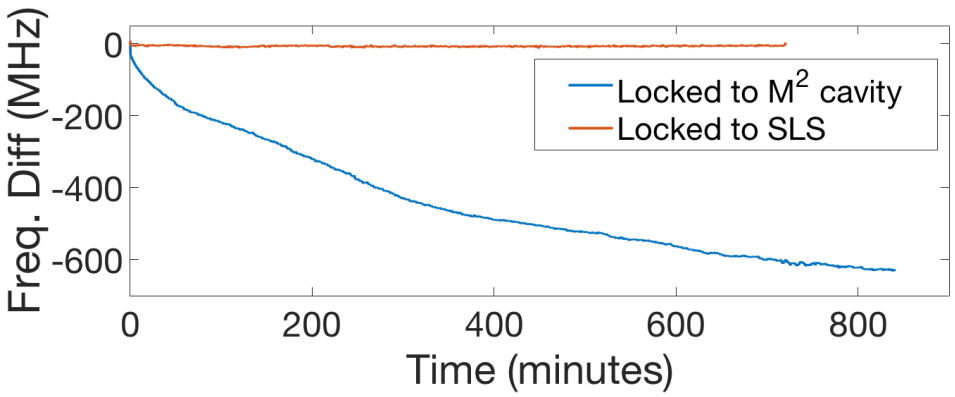

Figure 5.7: Comparison of measured drift for M^2 Ti:Sapph when locked to internal reference compared to when locked to the SLS cavity. Scans were taken on consecutive nights and measured with the Bristol wavemeter.

rial and operated at the zero-crossing of the thermal expansion inside a temperature stabilized vacuum chamber. Fig. 5.7 shows the drift of the laser locked and unlocked to the cavity on two overnight scans, where we see a drastic improvement on the long-term stability of the locked laser. These measurements are limited by the resolution and stability of the wavemeter used, but the expected long-term drift as quoted by SLS is $<$ 20 kHz per day. We do not have a better measure of long term stability at this time, but can reliably measure the same single ion for the order of a week without any noticeable drift.

We lock the laser to this reference cavity using the Pound-Drever-Hall (PDH) technique, which is a standard and elegant method for such a task [123, 124]. The PDH error signal is sent to a servo box (Vescent D2-125) that then feeds back to stabilize the Ti:Sapph frequency. With the laser etalon locked, we feedback to the Ti:Sapph resonator through a fast and slow piezo. The slow piezo is really slow (50 Hz), but has a tuning range of ±15 GHz. The fast piezo has a bandwidth of 100 kHz, but has a much smaller scan range of ±40 MHz. The main servo loop of the Vescent controller is used to feedback to the fast piezo. The auxiliary servo loop on the Vescent is used to feedback to the slow piezo to keep the output of the fast loop centered about zero. This slow loop adjusts for any drift in the Ti:Sapph relative to the reference cavity and allows for scanning of the laser while locked.

To enable scanning of the laser while still locked to the reference cavity, we insert an additional electro-optic phase modulator (EOSpace) on the locking path to gen-

get to the bottom of this as necessary.

erates frequency sidebands that we then lock to the reference cavity. By changing the frequency of the microwave source (Synth HD from Windfreak technologies) driving the EOM, the center frequency of the laser can be scanned while the sideband remains locked. This approach leads to small sections of the scans where the 0th and 1st order sidebands overlap that must be avoided when scanning. The corresponding blind spots in the scans are around 60 MHz, but we can access these areas as necessary by tuning the frequency source driving the downstream AOMs. With this method, we can reliably scan 3 GHz with accuracy determined by the frequency source. This is sufficient for most purposes, but could be extended as necessary for wider scans with the main limit being the tuning range of the piezo with the etalon locked and the frequency response of the EOM used for generating sidebands. We get the coarse wavelength of the laser using the wavemeter (Bristol 771), which allows us to reliably lock to the same cavity mode and access the same ions without additional searching. The Ti:Sapph is set up on an additional optical breadboard on top of the optical table that makes the system fairly insensitive to other experiments happening in the lab or the optical table. As a result, this lock is robust and reliable and the laser can stay locked to the same ion for up to weeks at a time.[5]

For two laser experiments, we use an offset frequency lock to maintain a fixed frequency separation between the ECDL and the stabilized Ti:Sapph. Outputs of these two lasers are mixed onto a high bandwidth detector and the resulting beat note is sent to a phase lock servo (Vescent D2-125), which turns this into an error signal and feedbacks to the current of the ECDL. The Toptica allows for direct current modulation of the laser head, which allows high bandwidth feedback and a tight lock. The locked beat note is much less than 10 kHz, which is much smaller than the Rabi frequency of the pulses we are using for the pumping sequence. To tune the ECDL lock, we tune an external frequency reference which is then multiplied by the Vescent controller to get the desired lock frequency. We use an additional slow feedback loop to the piezo voltage on the ECDL to keep the voltage on the current modulation around zero and extend this lock range. With this, we can achieve offset locks up to 9 GHz. The maximum frequency splitting at zero field for the 171 isotope is 6.8 GHz, so this is sufficient for us. To achieve larger offsets than this, one could add in another phase modulator in the path to extend the beat frequency or more simply lock the ECDL to a different mode of the reference cavity.

[5]The main limit again becomes the kindness and patience of other members in the lab that might want to use the laser.

Broadband light sources

While the Ti:Sapph is broadly tunable, it is not quite fast enough to be useful in aligning or tuning devices. For measuring the cavity reflection spectrum and other characterization, we typically use the a broadband light source such as a supercontinuum source (Fianiuum WhiteLase Micro) or a superluminescent diode in conjunction with the spectrometer described below.

SNSPDs

For photon counting measurements, we primarily use a set of WSi_2 superconducting nanowire single photon detectors (SNSPDs) made by Matt Shaw's group at JPL [125]. These are one of the most crucial parts of the measurement because these detectors have high efficiency ($\sim$ 75%) and low intrinsic dark counts (< Hz). With judicious time spent appropriately shielding the experiment, we can achieve total dark and leakage counts down <1 Hz counts (with the room lights on!). The SNSPDs live on the 100 mK stage of the fridge inside a mu-metal box that helps protect the detector from stray magnetic fields generated by the rest of the experiments. These detectors are biased with an isolated voltage source from SRS in conjunction with a precision resistor. The output of these detectors is amplified at room temperature and then sent to a time-tagging board. For these measurements, we use a SENSL HRM-TDC. Due to the limitations on the histogramming mode of this module, we use a custom executable to time tag events at full resolution and then histogram in post-processing. This has the advantage that we are taking all of the desired data we could ever want and can rebin as necessary, but care must be taken to not fill up the hard drive too quickly.

The SNSPDS are designed to be directly coupled to fiber, so are readily incorporated into the fiber network. We currently have an AOM before the SNSPDs which serves as a shutter to prevent latching of the detector from the excitation pulses used in the experiments. This gives a hit in overall detection efficiency (50%), but helps prevent spurious counts from reflections and after pulsing. [6]

Spectrometer

For characterizing and measuring devices, we typically use the broadband source described above with optical detection on the spectrometer (Princeton Instruments

[6] Other groups have had success in gating the SNSPDs directly [50], but we had some difficulty with this approach due to the fast gating time required for the short ion lifetimes in our system. Future measurements will benefit from an improved solution to this problem.

SP-2750 with PIXIS 2KB eXcelon). This is convenient for quickly measuring broadband spectra, with the limit being the resolution as limited by the diffraction grating ($\approx$ 3 GHz for our system at 980 nm). Once the device is found and aligned on the spectrometer, we perform finer resolution scans as necessary with the lasers described above.

Overall detection efficiency

The overall photon detection efficiency is determined by the losses in the many stages between an ion emitting a photon and the resulting "click" from the detector. First, we have the fraction of emission of the ion into the cavity mode, p_{cav}. Due to the Purcell enhancement achieved in our devices, $p_{cav} \approx 0.99$. The fraction of this that leaves the cavity into our desired waveguide mode is $p_{wg} = \kappa_{in}/\kappa$. For the device here, $p_{wg} \approx 0.12$. The coupling efficiency from waveguide to fiber is $p_f \approx 0.24$ as described above. The emitted light is coupled to the detection setup with a 99/1 fiber beam splitter ($p_{bs} \approx 0.95$). The light goes through an AOM shutter as described above with $\eta_{AOM} \approx 0.5$ and goes through another 99/1 beam splitter before being detected by the SNSPD with detection efficiency $p_d \approx 0.75$. The resulting total detection efficiency for this system is then $p_{tot} = p_{cav} p_{wg} p_f p_{bs}^2 p_{AOM} p_d \approx 1\%$.

The waveguide-cavity coupling and waveguide-fiber coupling are far and away the greatest source of loss in the system and should be the main focus for improving the performance of future devices. We have achieved devices in the past with $p_{wg} \approx 0.4$, which would then give a greater than 3-fold improvement in detection efficiency. Further improvements could be made with a new method for gating the SNSPDs rather than using the AOMs. Another small improvement could be made with slightly better SNSPD efficiency using commercially available detectors optimized for operation at 980 nm ($p_d \approx 0.9$ quoted for detectors from Photon Spot).

5.6 Microwave sources

While a relatively recent addition to the lab, the microwave infrastracture has rapidly expanded over the course of the last few months. A simplified schematic of the microwave setup for the current measurements in the Yb-171 singles devices is shown in Fig. 5.8. For microwave measurements in the Yb-171 ions, we use two tones to drive two separate microwave transitions in the ground and excited states. For this purpose, we use analog signal generators from Stanford Research Systems (SG380 with IQ modulation), with amplitude and phase controlled through IQ modulation by a fast arbitrary waveform generator (Tektronix AWG5204). All sources

are locked to a stabilized 10 MHz reference (SRS FS725). These microwave tones are then sent through additional switches and filters before being combined and amplified and sent to the device in the fridge. We wanted to ensure that we could achieve reasonable Rabi frequencies in the device with the amplifiers available in the lab, so used minimal attenuation inside the fridge on the microwave input for the initial configuration. In future, we will increase this attenuation to reduce any thermal noise contribution and reduce the effects of reflections at the various connections.

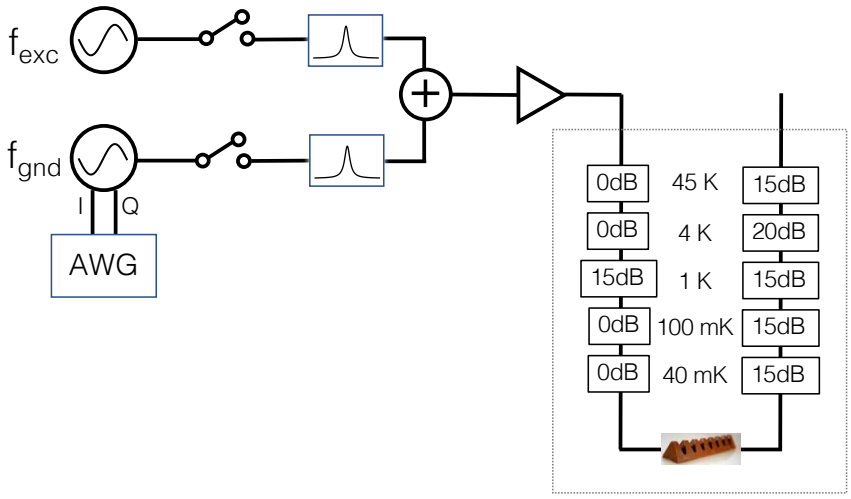

Figure 5.8: Simplified schematic of microwave setup. Two analog signal generators (SRS SG380) are used to generate tones to drive the ground- and excited-state transitions of ^{171}Yb:YVO_4 . The ground-state source is IQ-modulated by a fast arbitrary waveform generator (Tektronix AWG5204). Both sources pass through a switch (Minicircuits ZASWA-2-50DR+) and filter (Minicircuits ZABP-670-s+ on ground-state line and VBFZ-3590-S+ on excited-state line) before being combined, amplified (ZHL-5W-422+), and sent to the device in the dilution fridge. The microwave lines are thermalized at each stage with the attenuators shown and the output is terminated with a 50 ohm load.

Computer control

Experiments are all computer controlled via Matlab. To generate the pulse sequences necessary to drive the optical side of the experiment, we use a set of two two-channel 30 MHz arbitrary waveform generators (Agilent 33522b) and a delay generator (SRS DG345). While this has been a reliable setup for the past few years, it is now close to the limit of what we need in terms of speed and temporal reso-

lution. As the requirements get faster and expand to more complex measurements with multiple ions, more of this control will migrate to the Tektronix AWG5204 currently used to control the microwave side of the experiment.

Chapter 6

MEASUREMENTS OF A SINGLE YB ION IN YVO

In the next two chapters, I will describe the detection and coherent manipulation of single ytterbium ions coupled to a nanophotonic resonator. This chapter will focus on the measurements of an ion that we determine to be an isotope of ytterbium with zero nuclear spin (ZNS). While the 171-isotope is expected to have superior coherence properties, the simpler structure of the ZNS isotope allowed us to develop the techniques and experimental setup necessary to probe single ions before tackling the more complicated level structure of Yb-171. With this in mind, I will use this chapter to introduce the measurements used to probe single ions and provide representative results from the zero-spin isotope. In the next chapter, we will extend these techniques to enable measurements on Yb-171 ions.

This chapter starts by introducing our most fundamental measurement, which is the detection of cavity-coupled ions through resonant photoluminescence excitation spectroscopy. Building on this basic measurements, we identify a potential single ion and bound the optical coherence properties and long-term spectral diffusion of this ion. We then perform second-order photon correlation or $g^{(2)}$ measurements to measure the statistics of the emitted photons and verify that we have correctly identified a single ion. We determine the isotope of this ion by observing how the optical transitions behave in a magnetic field. We see a Zeeman splitting that corresponds to the expected behavior of a zero nuclear spin isotope and further verify this structure through cross-correlation measurements on the emission from the two observed optical transitions. From here, we optically initialize the ion into a single electronic spin state and demonstrate coherent microwave control of the electron spin.

6.1 Detection of single ions

After cooling down the device and tuning it onto resonance with the center of the Yb^{3+}:YVO_4 optical transition at 304505 GHz, the first experimental task is to identify single ions coupled to the cavity. In the current system, the most straightforward way to do this is through resonant photoluminescence excitation (PLE) spec-

troscopy[1]. For these measurements, we repeatedly send a narrowband excitation pulse into the cavity and measure the resulting photon emission as a function of laser frequency. Because we are measuring through the cavity mode, we do not have spatial isolation of single ions and are instead looking for ions that are isolated in frequency space.

Expected count rates

Let us first get an idea of the detection requirements of the PLE experiment. As a quick and optimistic estimation, we assume the case of continuous excitation of the ion in which we can get at most half a photon per ion lifetime [108]. The photon count rate due to the ion in this case is given by $R_{ion} \approx p_{tot}/2T_1$, where T_1 is the ion lifetime and p_{tot} is the total system detection efficiency (i.e. probability that a photon emitted by an ion inside the cavity gives rise to click on the detector). We will ignore for now that we cannot distinguish between the reflected excitation laser and ion emission with continuous excitation in the current experimental setup. The signal-to-noise ratio (SNR) of this measurement then depends on the ion emission rate compared to the rate of counts on the detector from other sources such as leakage of the excitation laser, dark counts of the detector, or fluorescence from other ions in the background. We lump these background contributions together and assign them a mean count rate R_{bg}. If we let the experiment run for some time T_{tot}, the total number of counts measured on the detector will be $N_{sig} = N_{ion} + N_{bg}$, where $N_{ion} = R_{ion}T_{tot}$ and $N_{bg} = R_{bg}T_{tot}$. The signal-to-noise ratio is given by

$$SNR = \frac{N_{ion}}{\sqrt{N_{ion} + 2N_{bg}}} = \sqrt{T_{tot}}\frac{R_{ion}}{\sqrt{R_{ion} + 2R_{bg}}}. \tag{6.1}$$

The question for the experimenter then becomes: how long will I have to integrate to get a decent signal and is this measurement realistic? To get a sense of what might be reasonable, the integration time that would be required to achieve a SNR of 20 as a function of ion count rate for different background count rates is plotted in Fig. 6.1. For the cavity we are working with, it is reasonable to expect lifetimes for a decently well-coupled ion of at least 5 μs. As described in the preceding chapter, we are operating at a total detection efficiency of $p_{tot} \approx 1\%$. In the best

[1] Another option to explore in the future would be measuring the change in the cavity transmission or reflection due to the presence of the ion [10]. One disadvantage of this techniques for an initial detection of ions is that it requires high cooperativity and requires the use of powers well below saturation. The linewidth of the reflected signal would thus be <100 kHz, which puts stricter requirements on the stability of the laser used for readout and would require a significantly finer scan to find an isolated ion within the inhomogeneous distribution.

case, we can then expect count rates of $\sim$ 1 kcps (thousand counts per second). We want to work in the regime where we are limited by the counting noise on these detection events rather than the background counts. This means we need the background count rate to be much smaller than the photon count rate. For reference, 1 aW of power is roughly 5×10^3 photons per second at this wavelength, so great care must be taken to make sure that there is no extraneous light leaking into the experiment. By using detectors with very low intrinsic dark counts, carefully shielding the experiment, and maximizing the extinction on the excitation path, we are able to get such spurious counts to the level of 1 cps such that the signal-to-noise in the experiment is limited by the ion count rate itself.

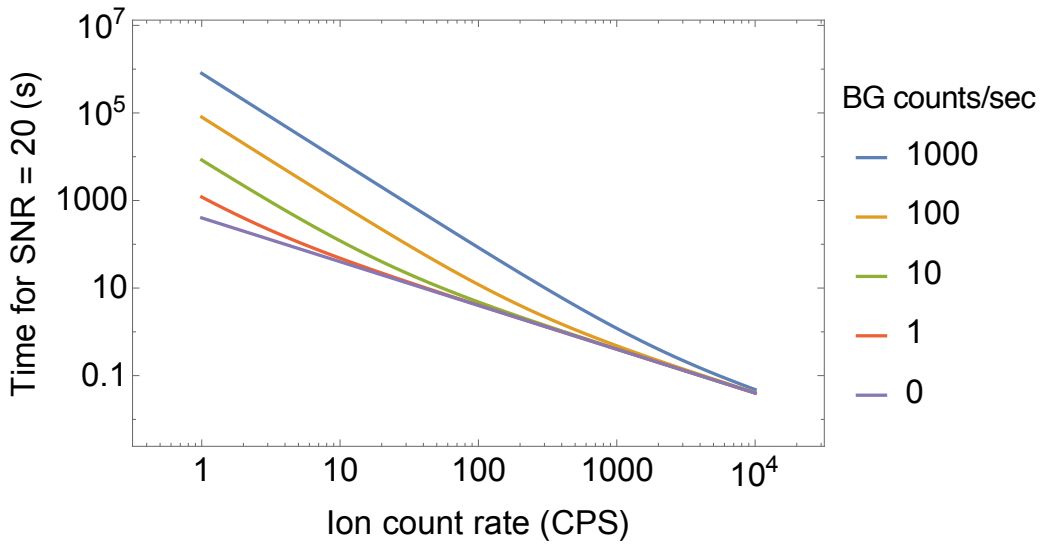

Figure 6.1: Integration time required to achieve a SNR of 20 as a function of detected count rate due to ion emission for increasing background count rates (in counts per second).

In the current experiment, we distinguish between excitation laser and resulting ion emission by using pulsed excitation such that these photons are separated in time. As a result, the overall count rate will be reduced from this maximum depending on the duty cycle of the experiment [2]. In this device, even if this corresponds to a factor of 10 reduction in overall count rates, we can still expect to achieve a decent SNR with a few seconds of integration per point. This is not an unreasonable place

[2] See e.g. John Bartholomew's thesis [126] for how one can go about optimizing this duty cycle.

to start for a patient grad student who's never worked with a brighter emitter and doesn't know any better.

This picture assumes that emission rate from the single ion is constant in time. In this case, the measured count rate can be mapped directly to the coupling strength of the ion to the cavity (See Chapter 4). In the presence of an additional long-lived ground state, an ion that is repeatedly excited can be optically pumped away to this state and the measured PL counts will underrepresent the coupling strength to the ion to the cavity. This effect arises with the ZNS ions in an applied magnetic field as we will see in the upcoming section. Similar complications arise with the non-zero nuclear spin isotopes (Yb-171 and Yb-173), which have multiple shelving states at zero field. We explore the implications of optical pumping on photon count statistics further in the context of single-shot readout in the next chapter. Essentially, without further work (e.g. reinitializing these ions), we will get fewer counts out per second than we would expect from the lifetime.

Experiment

In practice, measurements are typically performed at a repetition rate a few times slower than the lifetime (50-100 kHz) to enable us to gain additional information about the lifetime of the ions as we scan. A discrepancy between the observed photon count rate and ion lifetime in the absence of an applied magnetic field indicates a shelving effect and that the ion is mostly likely one with non-zero nuclear spin.

We typically start with a coarse, "high-power" sweep using pulses that give rise to a mean cavity photon number greater than one, which corresponds to $\sim$ 100 nW incident on the cavity. This gives rise to large enough Rabi frequencies to significantly power broaden the ion linewidth measured in PLE. The enables identification of potential isolated ions on a coarse scan (e.g. steps of 15 MHz) over the full span of the Yb-171 transitions. Running this high power readout at a fast repetition rate also leads to a noticeable heating of the device, which shortens the spin lifetime of the non-zero nuclear spin ions. This is actually quite useful for measurements in the Bluefors at dilution temperatures where otherwise the ion is pumped away at a rate faster than we can detect it and is then essentially invisible on the PLE scan without additional work. For these scans, we use pulses long enough to drive the ion to saturation (a few T_2) to make sure that we are not accidentally at an unfortunate pulse length (e.g. 2π pulse) and allow for direct comparison of ions with varying coupling strengths.

Fig. 6.2 shows a representative PLE scan over 12 GHz centered around the Yb:YVO_4 optical transition at 984.5 nm at zero applied magnetic field in the Bluefors. From this scan, we can identify clusters of ions that correspond to the different isotopes of ytterbium. The large distribution in the center (off the scale of the plot) corresponds to the optical transition of the zero-nuclear spin (ZNS) isotope of Yb. The cluster down near -5 GHz highlighted with a green box in corresponds to the Yb-171 transition that does not overlap with transitions of the other isotopes. We will look in more detail at this transition in the next chapter. On this coarse scan, we see a few well isolated peaks that we identify as potential single ions. For the rest of the chapter, we will look at the brightest of the bunch near 5.5 GHz (marked on the figure with an arrow). In exploring the properties of this ion, we will find that it is an isotope with zero nuclear spin. As such, I will refer to this ion throughout the text as the ZNS ion or ion Z.

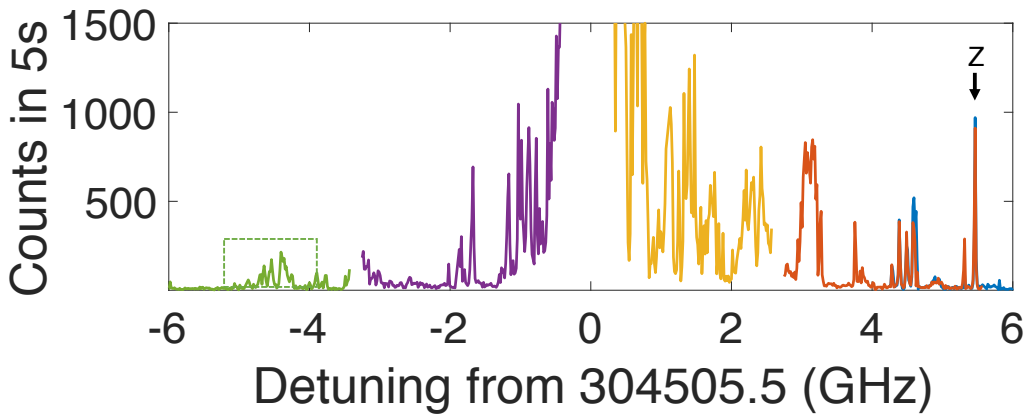

Figure 6.2: Resonant photoluminescence excitation (PLE) scan around the Yb:YVO optical transition. Measured in the Bluefors with nominal temperature of 50 mK and zero applied magnetic field. Scan performed with 50 kHz excitation rate and 5 s integration per point. Scans are performed with the laser offset-locked to the reference cavity and each color represents a different scan. The arrow points to "ion Z", which is the focus of this chapter. The green box marks the isolated Yb-171 transition that will be explored in the next chapter.

6.2 Line scans and spectral diffusion

Once we have identified a potential single ion, we then narrow the scan range and try to get a bound on the optical linewidth. To avoid power-broadening of the optical transition in this measurement, the optical power used for the scan is reduced until there is not further reduction in observed linewidth. Fig. 6.3 shows three scans

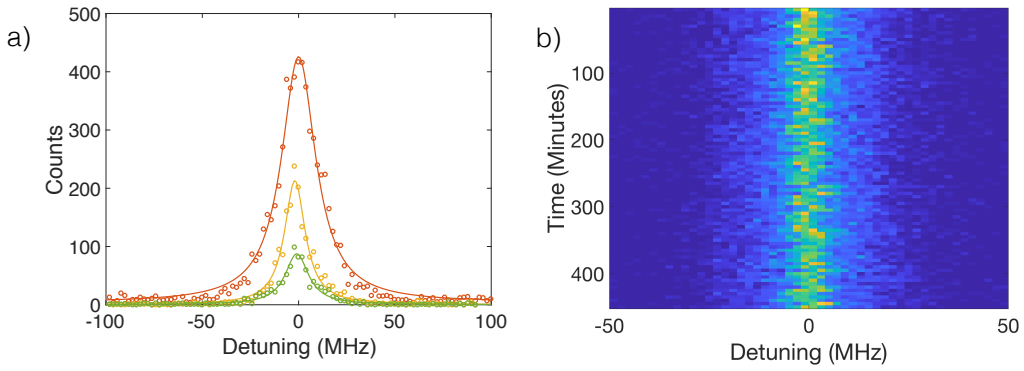

Figure 6.3: a) Fine PLE scans over ion Z as the optical power is reduced. At the lowest power (green scan), we extract a linewidth of 11 MHz (FWHM). b) Repeated scans of ion Z over 7.5 hours to measure long-term spectral diffusion.

over ion Z as the optical power is reduced. At the lowest powers used, we find the linewidth saturates to $\sim$ 11 MHz (FWHM). This bounds the coherence time to $T_2^* \geq 30$ ns. This coherence time is not unreasonable for what we expect for a zero-spin isotope in zero applied field. It should be noted that this scan requires many seconds of integration at each point, so is sensitive to low-frequency noise or spectral diffusion on that time scale. We should thus consider this as the time-averaged "inhomogeneous" or T_2^* linewidth of the ion. We will try to extract the "intrinsic" linewidth T_2 using coherent measurements in the upcoming sections.

We are also interested in spectral diffusion of this ion on much longer time scales. Fluctuating electric and magnetic fields can cause the transition frequency to change with time, which can be a significant issue in solid-state systems. For example, NV centers in diamond are highly sensitive to local electric field fluctuations and suffer from spectral diffusion when embedded in nanostructures [13]. For this system to be useful in the context of a quantum network that relies on interfering photons from two separate emitters, we want these fluctuations to be as small as possible. The site symmetry of Yb in YVO does not allow a first-order DC stark shift [127], which we expect will help reduce the sensitivity of the transition to fluctuating electric fields.

Fig. 6.3b shows a measurement of long-term spectral diffusion where the ion is repeatedly scanned over the course of 7.5 hours. The integration of this long-term scan has a linewidth of 13 MHz, which is a similar linewidth to the single scan linewidth. This indicates that the ion in the nanocavity is stable on these long time scales.

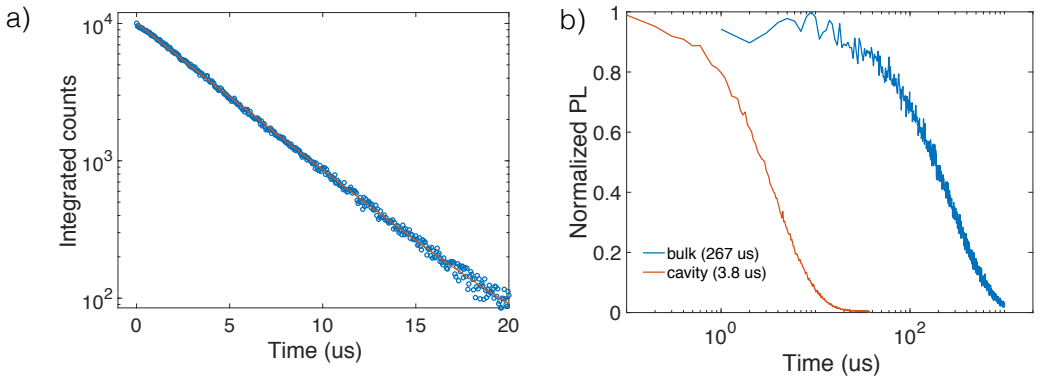

Figure 6.4: a) Time-resolved PL decay in the cavity, which gives lifetime of 3.8 μs. b) Normalized PL decay plotted on log-x scale for comparison to the lifetime measured in the bulk material.

6.3 Determining coupling rate to cavity

We next want to determine g, the coupling rate of the ion to the cavity. We extract this by measuring the Purcell-enhanced lifetime in a straightforward extension of the above. We tune the laser on resonance, repeatedly excite the ion, and histogram the resulting time-resolved photon detection events.

Fig. 6.4 shows the results of a lifetime measurement for ion Z when the cavity is maximally tuned on resonance with the cavity. We extract a lifetime of $1/\gamma_{cav} = 3.8\ \mu s$, which corresponds to a factor of ~ 70 reduction from the bulk lifetime. We determine the coupling rate g from (See Chapter 4.5)

$$\beta F_p = \frac{4g^2}{\kappa\gamma_0} = \frac{\gamma_{cav}}{\gamma_0} - 1, \tag{6.2}$$

where we use the cavity energy decay rate $\kappa = 2\pi \times 30.7$ GHz and the ion decay rate in bulk $\gamma_0 = 1/(267\ \mu s)$. This gives a single photon counting rate $g = 2\pi \times 17.8$ MHz. This is in the range of the values we predicted in Chapter 4 since we cannot assume that this ion is at the field maximum within the cavity mode. Based on this lifetime, the fraction of the ion emission into the cavity mode is $\eta_{cav} = \beta F_p/(1 + \beta F_p) = 0.986$.

6.4 Verifying that we have a single ion

The results on this ion look quite promising, but we want to ensure that we are indeed working with a single ion. Put simply, a single ion should only emit one photon at a time. As such, if we monitor the emission from a suspected single

ion, we should get at most one click on the detector per excitation (assuming that there are no counts on the detector from other sources). This can be quantified through the second order correlation or $g^{(2)}$ function. The $g^{(2)}$ is a standard way to characterize light sources [109] and the interested reader is referred to [110] for a pleasant introduction and history of this measurement. In short, it answers the question: given that the ion has a emitted a photon at time $t = 0$, what's the probability that it will emit another photon at time t?

We will work with a pulsed version of this measurement in which we repeatedly excite the ion at a repetition rate much slower than the excited state decay rate and count the number of photons detected after each pulse. The normalized photon correlation at time delay $t = 0$ for this scheme can be written as [128]

$$g^{(2)}[0] = \frac{\langle n(n-1)\rangle}{\langle n\rangle^2}, \tag{6.3}$$

where n is the total number of photons in a pulse. We see a perfect single photon source with $n = 1$ gives $g^{(2)}[0] = 0$ while a source with two photons gives $g^2 = 0.5$. The next experimental goal is then to measure $g^{(2)}$ for the photons emitted by the suspected single ion and verify that we observe $g^{(2)}[0] < 0.5$. The above definition can be extended to nonzero time delays as [128]

$$g^{(2)}[kt_r] = \frac{\langle n[0]n[kt_r]\rangle}{\langle n[0]^2\rangle} \text{ for } k > 0, \tag{6.4}$$

where t_r is the repetition time of the pulsed excitation and k is an integer greater than zero.

Using a perfect detector with photon number resolution, one could directly calculate the $g^{(2)}$ from the stream of photon detection events. In reality, most single photon detectors can only measure one photon at a time and will have some dead time after each detection event (typically 10s of nanoseconds) during which they cannot detect a second photon. This means for systems with optical lifetimes of a similar order to the detector deadtime that one cannot accurately measure the $g^{(2)}$ in this way because there is a high probability of missing two photon events due to this deadtime. For this reason, most $g^{(2)}$ measurements are typically done using a Hanbury Brown-Twiss (HBT) setup [109]. In the HBT measurement, the incoming light source goes through a beam splitter and the two outputs of the beam splitter are sent to two single photon detectors. With appropriate considerations to the overall photon rate, this allows one to avoid the problem of finite detector deadtime

and extract the $g^{(2)}$ from the time correlations of the detection events on the two detectors.

In our system, the lifetime of the ion in the cavity (4 μs) is much greater than the deadtime of the detection setup (50 ns). This allows us to detect multiple photon events during the ion lifetime and thus have something akin to photon number resolution over the integration window. As is the case with HBT measurements, we still need to ensure the overall rate of photon detection events is much less than the deadtime of the detector.

As a check that this is a reasonable assumption, we can calculate the probability of two photons arriving within the detector deadtime given the lifetime of the ion in the cavity. Let's say we have two emitters with the same lifetime T_1. Assuming an exponential decay of the photon wavepacket, the probability of emission by time τ is $p_{em}(\tau) = 1 - e^{-\tau/T_1}$. For $\tau << T_1$ this is approximately $p_{em}(\tau) \approx \tau/T_1$ and the probability of two emitters emitting in the deadtime τ_d will be at maximum $p_2 \approx (\tau_d/T_1)^2$. In our system, the resulting probability for missing two-photon emission due to the dead time is $\approx 10^{-4}$. In contrast, for a system with with $T_1 \sim \tau_d$, the probability of two events in the detection window would be $p_2 = (1-e^{-\tau/T_1})^2 \approx 0.4$. (See Charles Santori's thesis [129] for a thorough discussion on deadtime limits and implications for g^2 measurements in the context of quantum dot experiments.)

For the measurements here, we calculate the $g^{(2)}[0]$ by exciting the ion repeatedly, counting the number of photons after each excitation, and running an autocorrelation on these events. An advantage of this method for us is that it only requires one detector, which significantly simplifies the measurement and helps with overall detection rates. Calculating the full autocorrelation in this way also allows us to extract information about correlations on long time scales as will be explored in the upcoming sections. For measurements in the not-so-distant future with better cavities and faster emission rates, this measurement may eventually need to move to a HBT setup (but in that case we would be happy to have higher count rates!).

Measurement

Fig. 6.5 shows the results of a typical $g^{(2)}$ measurement on ion Z at zero applied magnetic field. We extract $g^{(2)}[0] = 0.058 \pm 0.006$, which indicates with high certainty that this is indeed emission from a single ion.

Assuming a perfect single photon source, the minimum attainable $g^{(2)}[0]$ will be

determined by the count rates from other sources (e.g. excitation leakage, emission from other ions, and dark counts) that can give rise to false coincidences on the detector. We can first compare the measured $g^{(2)}[0]$ to the lower-bound due to the observed background count level. Let n_{ion} be the number of counts from the ion and n_{bg} be the background counts from all other sources such that the total number of counts on the detector is $n_{tot} = n_{ion} + n_{bg}$. The minimum $g^{(2)}[0]$ assuming that the ion is a perfect single emitter and that the background emission is Poissonian can then be written as

$$g^{(2)}_{min}[0] = \frac{\langle n_{tot}(n_{tot}-1)\rangle}{\langle n_{tot}\rangle^2} \tag{6.5}$$

$$= \frac{\langle n_{ion}(n_{ion}-1)\rangle + \langle n_{bg}(n_{bg}-1)\rangle + 2\langle n_{ion}\rangle\langle n_{bg}\rangle}{\langle n_{ion}+n_{bg}\rangle^2} \tag{6.6}$$

$$= \frac{\langle n_{bg}\rangle^2 + 2\langle n_{ion}\rangle\langle n_{bg}\rangle}{\langle n_{ion}+n_{bg}\rangle^2} \tag{6.7}$$

$$= \frac{2A+1}{(A+1)^2}. \tag{6.8}$$

Here we have used $\langle n_{ion}(n_{ion}-1)\rangle = 0$ for the perfect single emitter, $\langle n_{bg}(n_{bg}-1)\rangle = \langle n_{bg}\rangle^2$ for a Poissonian background, and have defined $A = \langle n_{ion}\rangle/\langle n_{bg}\rangle$. Fig. 6.5b shows a PLE scan over the ion in the same conditions used for the $g^{(2)}$ measurements. We estimate the background contribution from the number of photons detected with the laser detuned by 100 MHz from the center of the transition. We extract $A = 50 \pm 16$, which corresponds to a minimum observable $g^{(2)}_{min}[0] = 0.039 \pm 0.012$. The measured $g^{(2)}[0]$ is slightly higher than the minimum expected if we were limited by background counts.

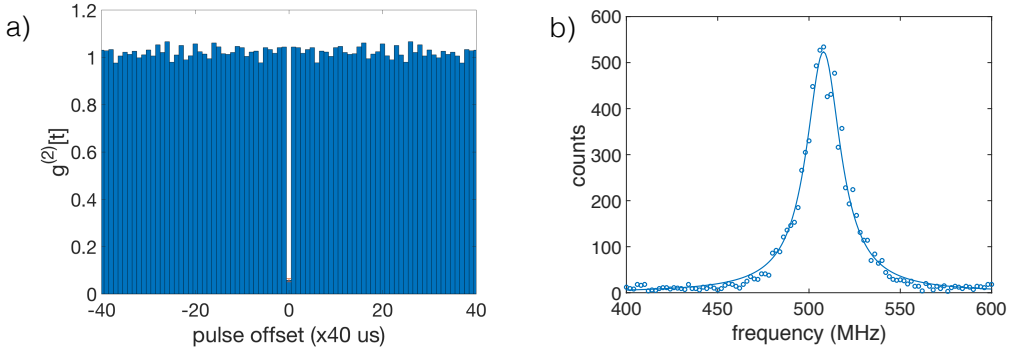

Figure 6.5: a) $g^{(2)}$ measurement on ion Z, which gives $g^{(2)}[0] = 0.058 \pm 0.006$. b) PLE scan at the same conditions as the $g^{(2)}$ measurement, used to extract signal-to-background for obtaining the background count limit to the $g^{(2)}[0]$.

One explanation for this behavior could be related to duration of the excitation pulse used for these measurements. In the two-level system with a finite excitation pulse length, there is some probability that the ion will emit a photon during the excitation pulse and then be re-excited and emit a second photon. This places fundamental limits on the minimum $g^{(2)}[0]$ for a two-level emitter as a function of the lifetime of the emitter relative to the length of the optical excitation pulse. This has been explored theoretically in detail in [128] and demonstrated experimentally in the context of quantum dot single photon sources in [130]. For Gaussian pulses of full width τ_{FWHM} and an emitter with lifetime γ, the simulated minimum $g^{(2)}[0]$ for a two-level system is given by [128] to be $g^{(2)}_{TLE}[0] = 0.4\tau_{FWHM}\gamma \pm 0.003$. For the $g^{(2)}$ measurements presented here, the length of the excitation pulse used was 500 ns long. This would then predict a minimum $g^{(2)}_{TLE} = 0.053 \pm 0.003$, which is close to the observed value. Further investigations of $g^{(2)}[0]$ with excitation pulse length will be necessary to confirm whether this is a plausible explanation. This will be of interest for future measurements as it will have similar implications for the visibility of experiments to observe two-photon interference [128].

In the context of this work, the observed $g^{(2)}[0]$ is satisfactory to show that we are indeed detecting emission from a single emitter. It is also worth pointing out that $g^{(2)}[t]$ is constant for $t > 0$, which indicates that any pulse-wise correlations have disappeared after one repetition of the experiment. This will be explored further in upcoming sections, but is a first indication that we are not shelving population with zero applied magnetic field and is further evidence that we are working with a zero-nuclear-spin isotope.

6.5 Zeeman splitting in an applied magnetic field

We can look at the behavior of the optical transition in an applied magnetic field to further confirm the isotope of the ion. For an isotope of Yb with zero-nuclear spin, we expect both the ground and excited states to have a linear Zeeman splitting with magnetic fields applied along the symmetry axes of the crystal. Fig. 6.6 shows 2D plots of PLE scans across the ion as magnetic field is applied parallel (Fig. 6.6a) and perpendicular (Fig. 6.6b) to the c-axis of the crystal. The observed behavior with applied magnetic field agrees with the splitting predicted from the spin Hamiltonian in Chapter 3. Note that the observed discontinuities in Fig. 6.6a are attributed to fussiness of the magnet power supply used in that measurement as it goes through zero current. Fig. 6.6b was performed with a newer magnet power supply that does

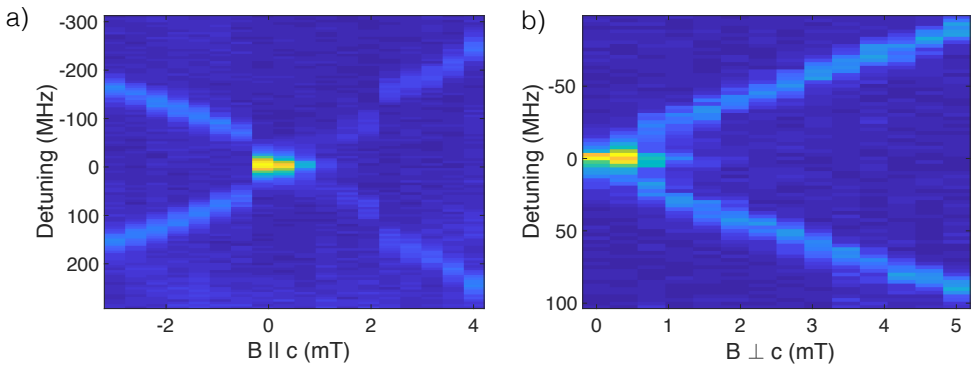

Figure 6.6: a) Map of PLE scans as varying magnetic field is applied along the c-axis. Brighter areas correspond to more counts. The observed discontinuities are resulting from the magnet power supply. b) Map of PLE scans as varying magnetic field is applied along the a-axis.

not suffer from this problem.

Fig. 6.7 shows the corresponding line scans extracted from Fig. 6.6a at three different magnetic fields to illustrate the splitting as magnetic field is applied. The two observed transitions correspond to the highest and lowest frequency transitions drawn in Fig. 6.7b, which are the transitions allowed for light with polarization aligned to the cavity mode. We see that in an applied magnetic field the measured count rate drops significantly from that observed at zero field. In the case of fast spin-relaxation between the two levels, we expect this count rate to be half of what is observed at zero field. The observed reduction in counts then gives evidence for optical pumping into a long-lived spin state.

6.6 Optical pumping with single ions

In this section, we further explore the optical pumping dynamics in the pulsed excitation measurements. The goal is to introduce the definitions and assumptions necessary for understanding the temporal dynamics observed in the pulsed photon correlation measurements. The interested reader is referred to e.g. [131] or [132] for further investigation into photon correlation dynamics in continuous measurements.

We start with the four-level system shown in Fig. 6.7c and consider the case where we excite the two cavity-coupled transitions with rates R^o_{12} and R^o_{34}. From state $|2\rangle$, the ion decays at a rate $1/T_1$ and decays to state $|1\rangle$ with probability β_{21} and decays

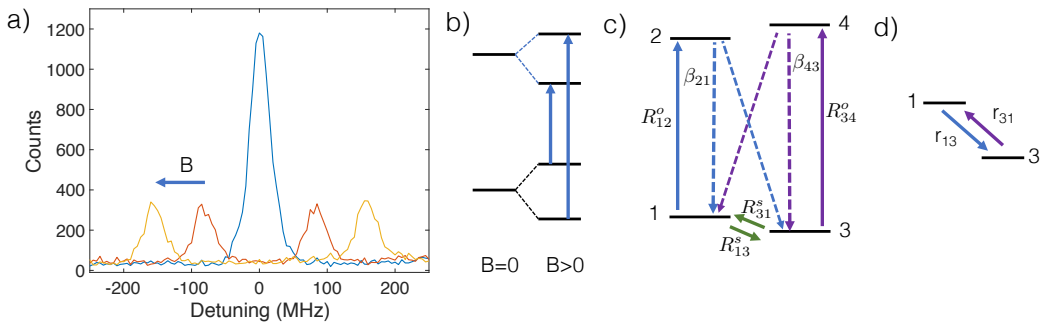

Figure 6.7: a) Representative PLE scans as magnetic field is applied along the c-axis extracted from Fig. 6.6. b) Corresponding optical transitions for the ZNS isotope. The ground and excited states are Zeeman split in an applied magnetic field. The transitions labeled are those aligned with the cavity mode ($E \parallel c$). c) Optical pumping scheme on four-level system with rates described in text. d) Effective two-level system for rate-equations described in text.

to state $|3\rangle$ with probability $1 - \beta_{21}$. Similarly, we define β_{43} for decay from state $|4\rangle$. We introduce spin relaxation from $|i\rangle$ to $|j\rangle$ as R^s_{ij}.

We assume pulsed excitation with a repetition time much slower than the excited state lifetime. We can then gain intuition and further simplify this picture by treating the 4-level system as an effective 2-level system. Because we are primarily interested in the number of photons after a given readout pulse, we are approaching this problem in a discrete time sense and this should be kept in mind in the following discussions. In this case, $R^o_{ij} = p_{exc} R^{rep}_{ij}$ is the effective excitation rate on the transition $|i\rangle \rightarrow |j\rangle$ where R^{rep}_{ij} is the repetition rate of pulsed excitation and p_{exc} is the excitation probability per pulse. We can define an effective optically-induced spin flip rate on $|1\rangle \rightarrow |3\rangle$ as

$$R^o_{13} = R^o_{12}(1 - \beta_{21}) \tag{6.9}$$

and similarly for R_{31}. The resulting effective decay rates between the two spin states are

$$r_{13} = R^o_{13} + R^s_{13} \tag{6.10}$$

$$r_{31} = R^o_{31} + R^s_{31}. \tag{6.11}$$

The rate equations for the populations in states $|1\rangle$ and $|3\rangle$ are then simply

$$\dot{p}_1 = -r_{13} p_1 + r_{31} p_3 \tag{6.12}$$

$$\dot{p}_3 = -r_{31} p_3 + r_{13} p_1, \tag{6.13}$$

where again the populations and time derivative should be interpreted in the discrete time sense of the pulsed measurements. These are readily solved to obtain the steady state populations ($\dot{p}_1 = \dot{p}_3 = 0$) in the two spin states:

$$p_1^{ss} = \frac{r_{31}}{r_{13} + r_{31}} \tag{6.14}$$

and

$$p_3^{ss} = \frac{r_{13}}{r_{13} + r_{31}}. \tag{6.15}$$

6.7 Cross-correlation measurements

We can apply this straightforward approximation to understand the expected dynamics of the $g^{(2)}$ measurements in the case of optical pumping. We consider the case where we only detect the photons resulting from excitation on the $|1\rangle \rightarrow |2\rangle$ transition such that the number of detected photons is proportional to the population in state $|1\rangle$. In practice we measure this by alternating the excitations on the two transitions and time-resolving the detection events due to each pulse. In principle, this could also be done with narrowband optical filtering. For the pulsed excitation scheme, we can write the time behavior of $g^{(2)}[t]$ for $t > 0$ as

$$g^{(2)}[t] = \frac{p_1[0;t]}{p_1[0;\infty]}, \tag{6.16}$$

where $p_1[0;t]$ is the probability of being in state 0 at time t (i.e. we detect a photon after exciting the ion at time t) given it was in state 0 at time $t = 0$. We normalize this to the probability of detecting an event as t goes to infinity given a detection at time $t = 0$.

The rate equations from the previous section are readily solved to give

$$p_1[0;t] = \frac{r_{13}e^{-(r_{13}+r_{31})t} + r_{31}}{r_{13} + r_{31}} \tag{6.17}$$

and

$$p_1[0;\infty] = \frac{r_{31}}{r_{13} + r_{31}}. \tag{6.18}$$

The correlation of counts detected after excitation on a single transition is given by

$$g^{(2)}[t] = 1 + \frac{r_{13}}{r_{31}}e^{-(r_{13}+r_{31})t} \text{ for } t > 0. \tag{6.19}$$

For the $g^{(2)}$ measurements on the four-level system, we expect to see bunching behavior for $t > 0$. This makes sense as we expect that at short times we will be

more likely to detect a second photon until the ion decays into a different state. The amplitude of this bunching will be determined by the relative size of the spin and optical flip rates on the two transitions. The decay constant of the $g^{(2)}$ will correspond to an effective spin lifetime as determined by the sum of optical pumping and spin relaxation rates. If we have knowledge of the the optical pumping rates (excitation probability, repetition, and branching ratio), we can use the $g^{(2)}$ measurement to extract information about the spin relaxation rate. If the excitation probability and optical branching ratio are not well known, one can in principle perform these measurements with varying powers and repetition rates to extract these parameters. For the fairly long spin lifetimes and low photon rates observed in this system, this method would be impractical at present time due to the integration times necessary to acquire adequate data. As such, we primarily use the observed dynamics to bound the spin lifetimes and check for self-consistency with the system parameters (e.g. spin lifetime and optical branching ratio) measured via more time-efficient measurements.

We can extend this analysis to the case where we measure the emitted photons on both transitions $|1\rangle \rightarrow |2\rangle$ and $|3\rangle \rightarrow |4\rangle$. We define this normalized cross-correlation as

$$g_{cc}[t] = \frac{p_3[p_1(t=0)=1, t]}{p_3[p_1(t=0)=1; \infty]}. \tag{6.20}$$

This will tell us the probability of detecting the ion in the state $|3\rangle$ at time t given we measured it in state $|1\rangle$ at time $t = 0$. From the rate equations above, this takes the form

$$g_{cc}[t] = 1 - e^{-(r_{13}+r_{31})t}. \tag{6.21}$$

The cross-correlation has the same decay constant as the $g^{(2)}$ measurement, but will be a rising exponential rather than a decaying exponential. This agrees with the expectation that if we measure the ion to be in state $|1\rangle$ at time 0, we will not find it in $|3\rangle$ until it has decayed to $|3\rangle$ through the optical or spin transition. This analysis can be extended in a straightforward manner to a system with more than two ground states with a similar rate-equation analysis. In that case, we would expect the $g^{(2)}$ and cross-correlation measurements to display more complex multi-exponential behavior. For instance, if we introduce an additional long-lived shelving state, we could expect an additional bunching behavior in the cross-correlation measurement.

It is worth noting that this type of bunching behavior in the $g^{(2)}$ could also be attributed to a spectral diffusion process. In this case, a similar formalism can be

used with the decay of the correlation now corresponding to the rate that the emitter diffuses out of the bandwidth of the excitation pulse. See [133] for a nice demonstration of this in which varying excitation and filter bandwidths were used to extract information about the spectral diffusion rates of quantum dots. By running the cross-correlation in addition to the $g^{(2)}$, we can then distinguish the bunching behavior in the $g^{(2)}$ due to spectral diffusion and spin relaxation.

A measurement of the cross-correlation then complements the $g^{(2)}$ measurement and allows us to verify that the two observed transitions in an applied magnetic field are from one and the same ion.

Experiment

We implement the correlation measurements on the ion in an applied magnetic field by alternately exciting the two cavity-enhanced transitions as labeled in Fig. 6.8a. For this measurement, the applied magnetic field along c led to a 80 MHz frequency difference between the two optical transitions ($B \parallel c = 6.5$ G). This splitting was chosen such that the two transitions could be excited with a single laser by switching the drive frequency of the acousto-optic modulator used to generate the pulses. We bin the number of photons detected after each pulse and calculate an auto and cross-correlation as described above. The results of this measurement are shown in Fig. 6.8c. For this measurement, we are using the same excitation powers and rates on p_1 and p_2 and the $g^{(2)}$ is calculated from the average of the $g^{(2)}$ measured on transitions 1 and 2. In this case, $g^{(2)}[t]$ takes the form

$$g^{(2)}_{Ptot}[t] = 1 + e^{-(r_{13}+r_{31})t}. \tag{6.22}$$

The auto and cross-correlation are well fit by exponentials with a decay constant of 950 μs. If we assume that the optically-induced spin flip rate is much smaller than the direct spin relaxation rate, we can assign a pessimistic lower bound on the spin state lifetime to ≥ 950 μs. A small set of measurements similar to those shown in Fig. 6.8c at different pulse repetition rates indicate that the decay observed in the correlations is largely dominated by optical pumping rather than spin relaxation. If we instead assume that the spin relaxation is negligible, we can obtain an estimate of the optical branching ratio. For this measurement, the repetition rate on each transition is 25 kHz and the ions are driven to saturation ($p_{exc} \approx 0.5$). The observed decay then corresponds to a lower bound on the optical branching ratio of $\beta_{21} \approx 0.96$. We will explore a more time efficient way to measure the spin lifetime in the

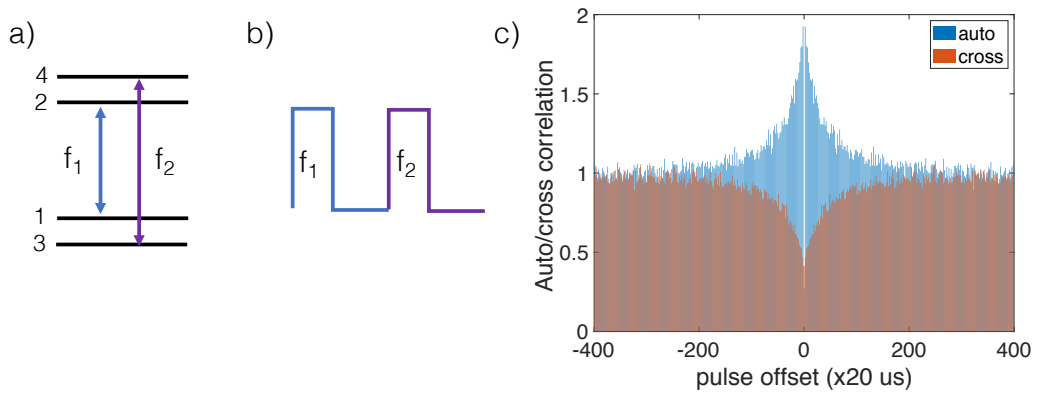

Figure 6.8: Correlation measurements on zero-spin isotope. a) Four-level system corresponding to Zeeman split levels of ZNS isotope with $B||c$. Optical transitions correspond to the cavity coupled transitions allowed for $E \parallel c$. Here, $|f_1 - f_2| =$ 80 MHz. The optical transitions in (a) are excited in an alternating fashion as shown in (b). The corresponding auto- and cross-correlation (blue and red, respectively) of the observed photon counts after each pulse.

next section. A more direct measure of the optical branching ratio will be performed in the next chapter.

While many extensions to these measurements could be used to gain more insight into the system, for our purposes these results show that these two transitions observed in a magnetic field are from the same ion. The behavior of the observed cross-correlations provide more evidence that we are working with a zero-spin isotope of Yb with the corresponding four-level system shown in Fig. 6.7.

6.8 Spin initialization

After verifying that we are moving population between two ground states of the ion in the cross-correlation measurements, we want to initialize population into a single ground state. For the measurements in the previous section, we were reading out the population by exciting both of the cavity-enhanced optical transitions. Because these transitions are fairly cyclic, this is not an efficient way to optically pump out of a given state. We can instead tune the frequency of the pumping laser such that we excite on the cross transition that is allowed for the orthogonal polarization. Once excited, the ion will then have a high probability of decaying via the cavity-enhanced transition and flipping the spin in the process. In this way, we can efficiently prepare the ion into the desired spin state.

The amount of improvement in the pumping rate can be seen in the following way. Using the level structure in Fig. 6.7c, let's say we want to initialize into state $|1\rangle$. For resonant driving on $|3\rangle \rightarrow |4\rangle$, we have the optically induced spin flip rate from $|3\rangle$ to $|1\rangle$ as

$$R^o_{31} = R^o_{34}(1 - \beta_{43}). \tag{6.23}$$

If instead we implement cross transition pumping on $|3\rangle \rightarrow |2\rangle$, we have

$$R^o_{31} = R^o_{32}\beta_{21}. \tag{6.24}$$

For this system, the branching ratios will be symmetric with $\beta_{21} = \beta_{43}$. So if we achieve a similar pumping rate on R_{34} and R_{32} (i.e. can drive both transitions to saturation in the pulsed scheme), we have enhanced the pumping by $\beta_{21}/(1 - \beta_{21})$. From the lower bound on the branching ratio described above $\beta = 0.96$, this corresponds to a 25 times increase in pumping rate.

Fig. 6.9a shows a 2D map of the PLE as we scan the frequency of the readout pulse with different detunings of the repump pulse. We see that when the optical pumping frequency hits the lambda transition we get a large increase in counts, which indicates that we are efficiently moving population back into the readout state. Fig. 6.9b shows the corresponding PLE scans with and without preparation. We compare this to the observed count rate at zero applied magnetic field and estimate a spin initialization of 95%.

This measurement can then be extended in a straightforward manner to directly measure the spin lifetime. We initialize the ion, wait, and then readout the population. The decay of population as a function of wait time gives the spin state lifetime. Fig. 6.10 shows one such measurement in which we observe a lifetime of 9 ms at a ground state splitting of 80 MHz. We do not currently have bulk measurements of the zero-spin isotopes in a similar regime, but expect that this lifetime is limited by flip-flop interactions between Yb ions rather than spin-lattice relaxation [134]. This could be explored as a function of the size and direction of the applied magnetic field to further elucidate the underlying relaxation mechanisms.

6.9 Optical coherence measurements

We can start to further investigate the coherence properties of the optical transition by turning up the power on the optical readout pulse until we see coherent Rabi oscillations of the population between the ground and excited state. Fig. 6.11 shows

the results of one such measurement in which we initialize the ion and measure the resulting PL as a function of readout pulse length. In Fig. 6.11a, we see coherent oscillations with Rabi frequency $\Omega_r = 2\pi \times 8.6\,\text{MHz}$. The Rabi frequency is related to the mean cavity photon number $\bar{n}$ by $\Omega_r = 2g\sqrt{\bar{n}}$. Using $g = 2\pi \times 17.8\,\text{MHz}$ obtained from the lifetime measurement, this corresponds to a mean cavity photon

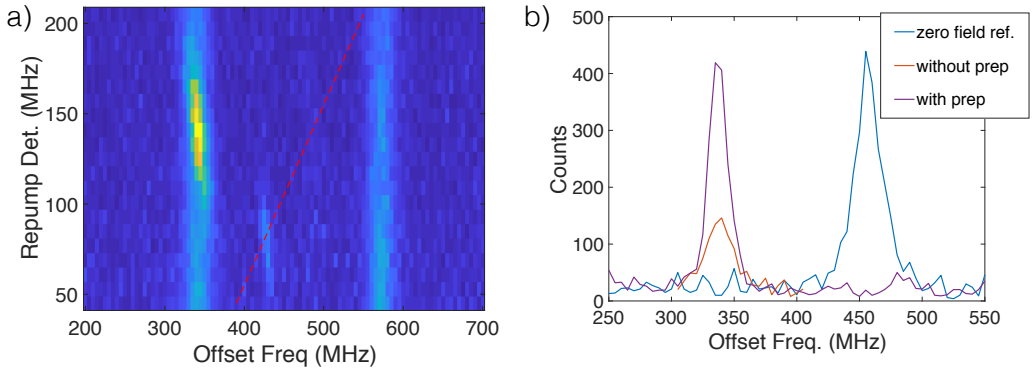

Figure 6.9: Spin initialization of the ZNS isotope. a) Map of PLE scans as the frequency of the pumping pulse is tuned across the lambda system. The red dashed red line is a guide to the eye for the detuning of the repump laser with the readout pulse at $\sim$ 340 MHz. b) Corresponding PLE scans at optimal detuning of pumping pulse. The measured counts with and without preparation are compared to the count rate observed at zero applied magnetic field. This gives an initialization fidelity of 95%.

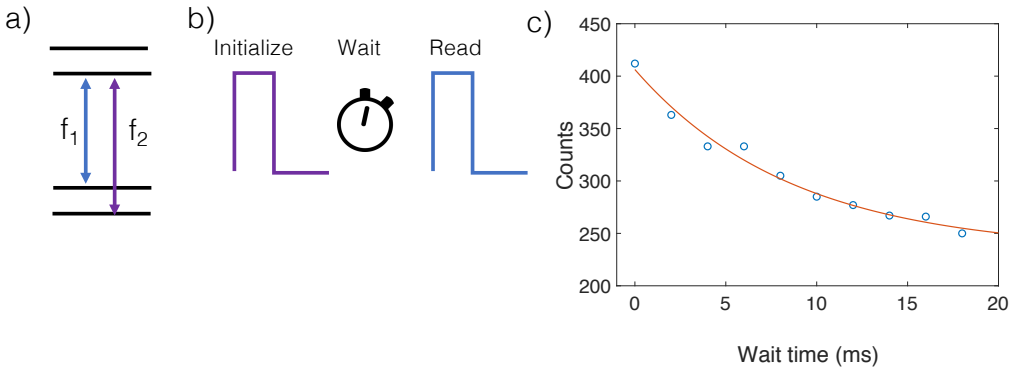

Figure 6.10: Spin lifetime measurement on ZNS isotope. a) Level-structure and optical transitions used. The four states correspond to the Zeeman split excited and ground states. Here, we make use of the lambda system using a transition allowed for light polarized $E \perp c$. b) Sequence for spin-lifetime measurement. c) Population measured by reading out on f_1 as a function of wait time. Exponential fit gives lifetime of 9 ms.

number of $\bar{n} = 0.06$. This correspond to $\approx 5\,\mathrm{nW}$ incident on the cavity. Such measurements provide a good way to double-check system efficiencies and we find good agreement between the expected and measured values. Fig. 6.11b shows another example of a similar scan at a higher Rabi frequency as a function of laser detuning.

The Rabi oscillations in Fig. 6.11a decay exponentially with a decay time of 400 ns. This data was taken with $B \perp c = 80$ mT. In general, the decay of the driven Rabi oscillations can be quite complex and will have a dependence on the strength of the driving term and the nature of the source of dephasing in the system [135, 136]. With those caveats in mind, we can still extract an estimate for the decoherence times from the simple optical Bloch equation picture. In this picture, this decay will be determined by the population decay rate $\gamma_0 = 1/T_1$ and any additional dephasing of the ion denoted as γ_{deph}. The coherence time T_2 is then given by

$$\frac{1}{T_2} = \frac{\gamma_0}{2} + \gamma_{deph}. \tag{6.25}$$

On resonance, the Rabi oscillations will decay with rate [137]

$$\gamma_{rabi} = \frac{3\gamma_0 + 2\gamma_{deph}}{4}. \tag{6.26}$$

For Fig. 6.11a, we extract an excess dephasing rate of $\gamma_{deph} = 2\pi \times 730$ kHz and a coherence time of $T_2 = 210$ ns. While these measurements give an idea of the coherence time, they more importantly allow us to identify the π and $\pi/2$ pulse lengths necessary to perform further measures of the optical coherence.

We spent some time exploring optical Ramsey measurements on this ion with limited success. Measurements proved to be difficult with the limited rise time and time resolution of the setup available at the time of these measurements, but these results indicated that $T_2^* < 50$ ns. This is in rough agreement with the minimum linewidth observed in the PLE scans. We had slightly better success with the optical echo measurement. Fig. 6.12 shows the results of an optical echo experiment in which we measure $T_2 = 130$ ns. This measurement was taken with $B||c = 6.5\ G$. Further investigations are required to explore the magnetic field dependence of the optical coherence times in this ion.

These optical coherence times are short compared to the optical lifetime, but the expectations for the zero-spin isotope were low. The large g-factor of the ground

and excited states makes them quite susceptible to magnetic field fluctuations. The measured values are similar to what is measured on the zero-spin isotopes in bulk. While the observed coherence on this ion is far from the lifetime limit in the current device, the ability to coherently drive the optical transition provides the foundation for more efficient pulsed readout and all-optical manipulation of the spin state.

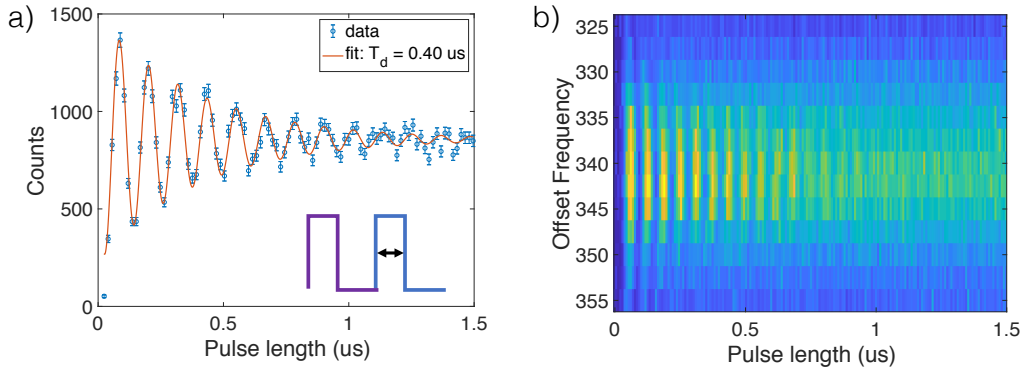

Figure 6.11: Optical Rabi oscillations on the ZNS isotope. The ion is initialized into a single spin state and then excited with a variable length readout pulse. The resulting PL is plotted as a function of readout pulse length. a) Example with Rabi frequency of 8.6 MHz and decay time of 400 ns. Here, $B \perp c = 80$ mT. b) Optical Rabi oscillations as the excitation frequency is moved across the resonance. Note that the frequency is referenced to the cavity-lock frequency and not the detuning from the center of the ion.

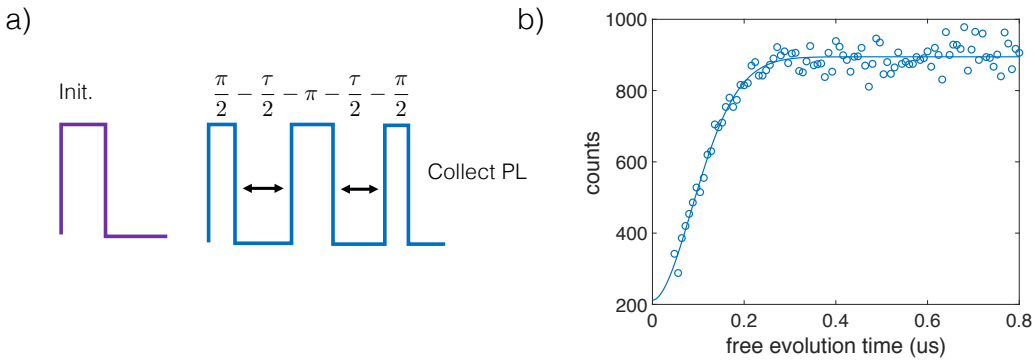

Figure 6.12: Optical echo on the ZNS isotope. a) Sequence used for optical echo measurements. b) Optical echo signal as a function of free evolution time τ. Fit gives $T_2 = 130$ ns. This data was taken with $B||c = 6.5$ G.

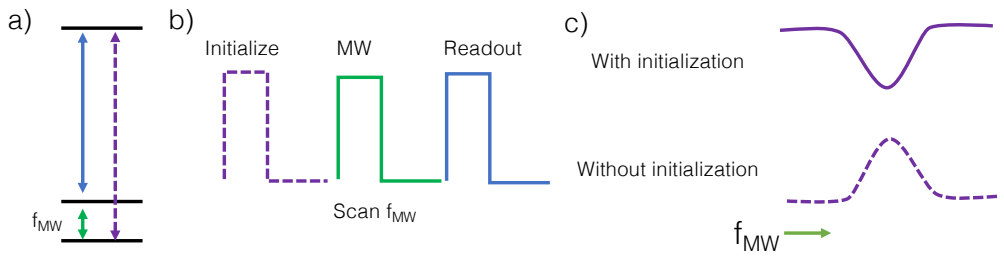

Figure 6.13: Optically detected magnetic resonance measurements. a) Energy level structure and corresponding optical and microwave frequencies used. b) Sequence used for ODMR. c) Expected signals with and without optical initialization.

6.10 Optically detected magnetic resonance

After exploring the optical measurements, we now want to introduce microwave driving on the electron spin transition. The most basic spin measurement we can do is an optically detected magnetic resonance (ODMR) measurement. In short, we send in a microwave pulse and optically readout the resulting change in the spin population as a function of applied microwave frequency. When the microwave pulse is on resonance with the spin transition, it will transfer population between the two ground states. If we start with the population initialized into the readout state, we will see a decrease in count rates when the microwave pulse is resonant with the ground state transition. This measurement can also be performed without an optical initialization pulse. In this case, the repeated optical readout pulse serves to pump population out of the readout state. Tuning the microwave drive into resonance with the ground state transition then leads to an increase in population in the readout state and a peak in ODMR.

Fig. 6.14 shows examples of two such measurements. As the oscillating magnetic field due to the microwave CPW is along the c-axis, these measurements are performed with a static magnetic field perpendicular to the c-axis. On the left, we show an ODMR measurement in a small magnetic field (7 mT) where we have initialized into the readout state. On the right, we show in a larger applied magnetic field (157 mT) in which we do not initialize before the sequence. In both cases, we reduce the microwave power until there is no noticeable change in the linewidth of the ODMR signal. The width of this ODMR peak bounds the spin coherence time. We measure full-widths of $\approx$ 12 MHz in both cases, which is similar to what is observed on the optical transition. This is expected if the coherence is limited by

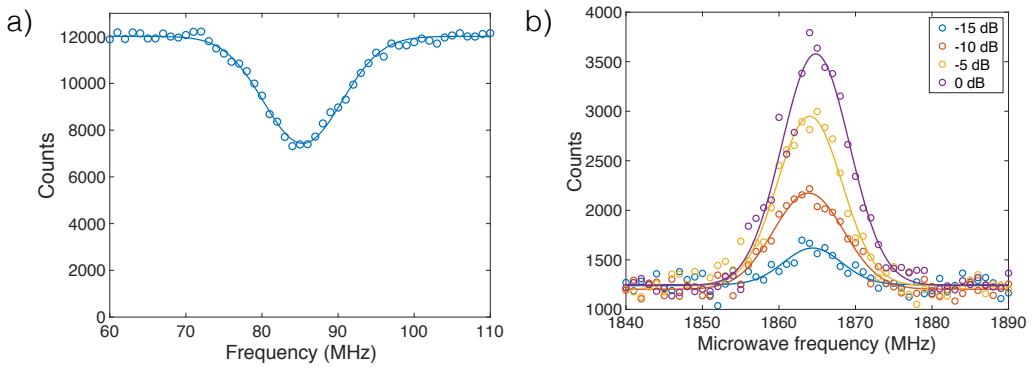

Figure 6.14: ODMR on the zero-spin isotope at two different magnetic fields. a) Low-field ODMR with optical initialization. $B \perp c \approx 7$ mT. b) ODMR at higher field for increasing attenuation of applied microwave pulse. $B \perp c \approx 157$ mT

the magnetic field sensitivities of these transitions.

6.11 Spin coherence measurements

After finding the spin transition in ODMR, we can then turn up the microwave power until we see coherent Rabi oscillations on the spin transition. For this measurement, the population is initialized into the readout state, a resonant microwave pulse of width τ is applied to the ground state transition, and an optical readout pulse maps the population of the ion to fluorescence. Repeating this sequence for a varying τ allows us to trace out the Rabi oscillations on the spin transition. Fig. 6.15 shows the results of one such measurement. We extract a Rabi frequency of 8.7 MHz and a decay constant of 530 ns. Using the spin lifetime measured earlier, this would correspond to $T_2 = 265$ ns.

Ramsey measurements in this configuration proved to be difficult in the current setup due to the short T_2^* and we again bound this to be less than 50 ns. We were able to perform a spin echo sequence as shown in Fig. 6.15b, which gives $T_2 = 84$ ns. As in the optical case, there is a significant discrepancy between the coherence time measured with echoes and that extracted from the Rabi oscillations. Further investigations into the decay of the Rabi oscillations with drive power might shed some light on this discrepancy.

While the spin coherence times are also quite short for the spin transition, the expectations were quite low for the zero-spin isotope. The importance for us is showing

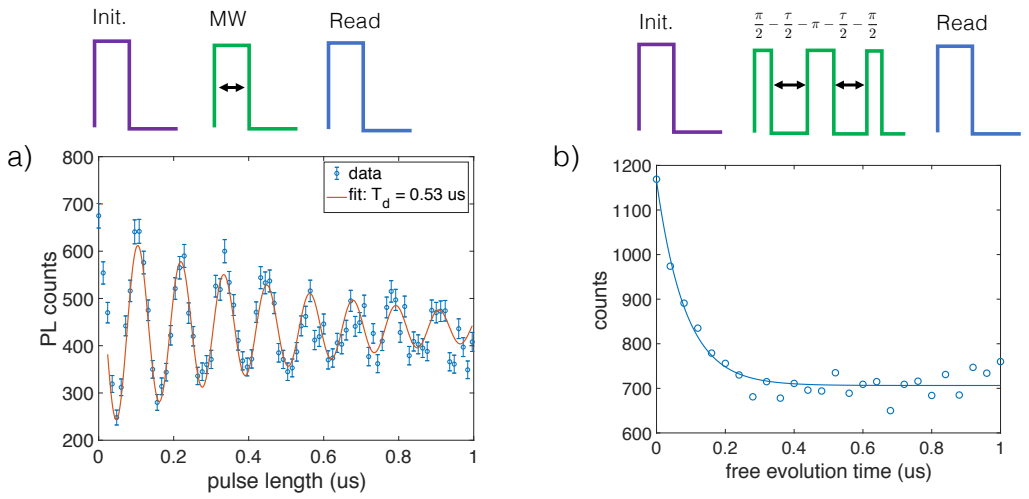

Figure 6.15: Coherent spin measurements on ZNS isotope. a) Rabi oscillations on the spin transition at a ground state splitting of 85 MHz ($B \perp c \approx 7$ mT). Fit gives Rabi frequency of $\Omega_r = 2\pi \times 8.7$ MHz and decay constant of 530 ns. b) Spin echo measurement as a function of free evolution time τ. Fit gives $T_2 = 84$ ns

that we can coherently drive the spin transition in this configuration with a fairly high Rabi frequency. This gave us confidence that we would be able to drive the ground state Yb-171 transition at zero-field since it will have the same transition strength as the ZNS ion.

6.12 Conclusion

In this chapter, I presented measurements on an ion that we determined to be an isotope of ytterbium with zero-nuclear spin. While there are many avenues for further exploration with this ion, the prospect for achieving long optical and spin coherences with these ions in this sample is low and we instead shifted focus to measurements on the Yb-171 isotope. The time spent on the zero-spin was significant for us in that it allowed us to develop the experiments and show that we coherently manipulate the electron spin of single rare-earth ions in this system. With these tools in hand and confidence in the measurements, we are then ready to tackle the more complicated level structure of the 171 ion.

Chapter 7

MEASUREMENTS OF SINGLE ^{171}YB:YVO_4 IONS

After whetting our appetite with measurements on the zero-spin ion, we then moved to the 171-isotope with the prospect of longer coherence times for both the optical and spin transitions. In this chapter, I present an initial set of measurements on ions we have determined to be of the Yb-171 isotope. I start by discussing the motivation for working at zero applied magnetic field rather than the high-field regime explored in the spectroscopy chapter. I then introduce the relevant optical and spin transitions for this work and describe how we can initialize the ion into one of the ground states. I then present measurements of the spin and optical coherence properties of single ytterbium-171 ions. I conclude with initial results showing single-shot readout of the spin state.

7.1 Why work at zero field?

For the initial work with single Yb-171 ions, we decided to explore the regime of zero magnetic field rather than the high magnetic field limit presented in the spectroscopy chapter. In this section, I will outline the two main considerations in this decision: the prospect of long coherence times at zero field and a significantly larger spin transition strength.

The primary reason for exploring this regime is the existence of spin and optical transitions that are first-order insensitive to applied magnetic fields. As discussed in the Chapter 3 and reproduced in Fig. 7.1, the hyperfine coupling in the uniaxial symmetry of YVO partially lifts the degeneracy of the energy levels at zero magnetic field and gives rise to energy eigenstates in the ground and excited state of the form: $|11\rangle = |\uparrow\Uparrow\rangle$, $|1,-1\rangle = |\downarrow\Uparrow\rangle$, $|10\rangle = \frac{1}{\sqrt{2}}(|\uparrow\Downarrow\rangle + |\downarrow\Uparrow\rangle)$, and $|00\rangle = \frac{1}{\sqrt{2}}(|\uparrow\Downarrow\rangle - |\downarrow\Uparrow\rangle)$. We see that states $|00\rangle$ and $|10\rangle$ are completely mixed states of both electronic and nuclear spin and thus have net zero total spin. As a result, theses energy levels are insensitive to first-order perturbations by the Zeeman interaction. Explicitly, for $|\psi\rangle = |10\rangle, |00\rangle$ we have for any perturbing magnetic field $\mathbf{B}$:

$$\langle\psi|\, \mu_B \mathbf{B}\cdot\mathbf{g}\cdot\mathbf{S} - \mu_n \mathbf{B}\cdot\mathbf{g_n}\cdot\mathbf{I}\,|\psi\rangle = 0. \tag{7.1}$$

Optical and spin transitions between states of this form will then have a reduced sen-

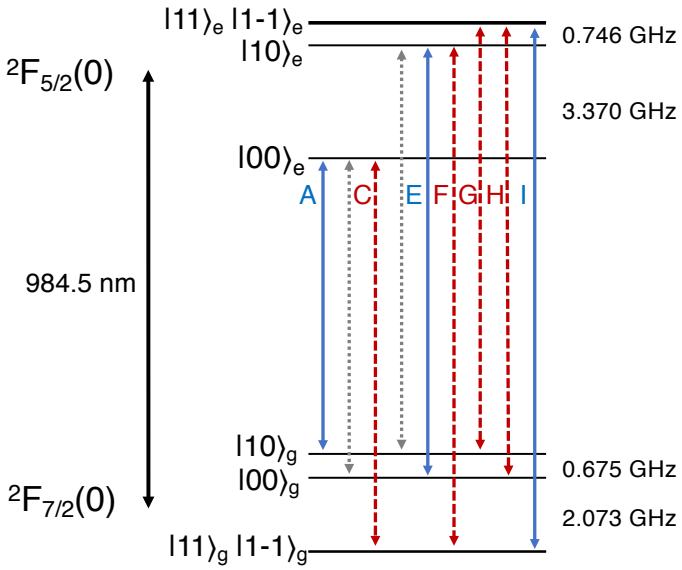

Figure 7.1: Zero-field energy level structure of ^{171}Yb:YVO$_4$ reproduced from Chapter 3 for reference. Transitions allowed for $E \parallel c$ ($E \perp$ c) are shown in solid blue (dashed red). The dotted grey lines correspond to transitions that are forbidden by symmetry.

sitivity to magnetic field fluctuations.[1] Such transitions in the context of rare-earth ions are typically referred to as ZEFOZ (ZEro-First Order Zeeman) transitions.[2] As fluctuating magnetic fields are suspected as the primary source of decoherence in this system, we then expect significant improvement in coherence times compared to the zero-spin isotope. An enhancement of coherence at zero-field ZEFOZ transitions has been demonstrated in ^{171}Yb:Y_2SiO_5 [74] and ^{167}Er:Y_2SiO_5 [98]. While this was not explored in the work presented in the Chapter 3, initial optical measurements in the 100 ppm Yb-171-doped crystal indicate optical coherence times > 25 μs on transition A at zero applied magnetic field.

Another reason for working at zero-field was ensuring that we could efficiently drive the microwave transition. Transitions between the ZEFOZ states $|10\rangle$ and $|00\rangle$ are

[1] The magnetic sensitivity of these transitions are then determined then by the second-order Zeeman interaction. See e.g. [138] for calculations of this contribution.

[2] Since this transition occurs at zero applied magnetic field in this context, one might even go as far as calling this a ZEFIZEFOZ (Zero-FIeld ZEro-First Order Zeeman) transition, but quite frankly I think that's just a little too silly. Transitions with zero first-order sensitivity to magnetic fields are found and desired in many areas of physics and go by different names in their respective fields, e.g. clock transitions in AMO physics or sweet spots and optimal working points in spin qubits.

allowed for oscillating magnetic fields $B_{\parallel}^{ac}$ parallel to the c-axis:

$$\langle 00|\, \mu_b B_{\parallel}^{ac} g_{\parallel} S_z \,|10\rangle = \frac{\mu_b B_{\parallel}^{ac} g_{\parallel}}{2}. \tag{7.2}$$

We see that the transition between these states is electron-spin like with a transition dipole of $\frac{\mu_b g_{\parallel}}{2h}$ = 42.5 GHz/T. In contrast, in the high-field limit we achieve long coherence times by freezing out the electron spin and working with states that are almost pure nuclear spin states. This results in transition dipole moments that are more than 2000 times smaller than the zero-field ZEFOZ transition dipole moment.

A related consideration is the required orientation of the crystal axis with respect to the applied static and oscillating magnet fields. For the microwave coplanar waveguide (CPW) on the current set of devices, the oscillating magnetic field we can apply to drive the spin transitions is almost entirely along the crystal $c-$axis. Unfortunately, the best orientation to achieve long coherence in the high field will also be with the magnetic field along c. In this case, the nuclear spin transitions are only allowed for oscillating magnetic fields perpendicular to c. We are then relying on a residual component of the oscillating magnetic field from the CPW along the a-axis, which leads to a further reduction of achievable driving strengths. We could in principle drive these transitions in this device by buying a larger microwave amplifier, but the requisite higher powers would also induce a significant additional heat load to the dilution fridge. Working at zero-field allows us to achieve higher Rabi frequencies at much lower powers in the current device and still maintain low temperatures in the fridge. This is ideal for the initial demonstrations with these ions.

Another more subtle consideration in the choice of working at zero field is making sure that we can find an isolated ion. At zero field, the Yb-171 isotope has an optical transition that does not overlap with transitions of the other isotopes (as shown in Fig. 7.1). In the high-field limit however, the optical transitions of the 171 isotope overlaps with those of the 173 isotopes. In the relatively high doping density of this sample, this makes the initial search process for an isolated ion substantially more difficult.

While not as readily accessible with the current device, the high-field limit offers the promise of longer optical and spin coherences and is of significant interest in future work. Modifications to the design of the optical and microwave cavities used should enable further exploration of that regime in the future.

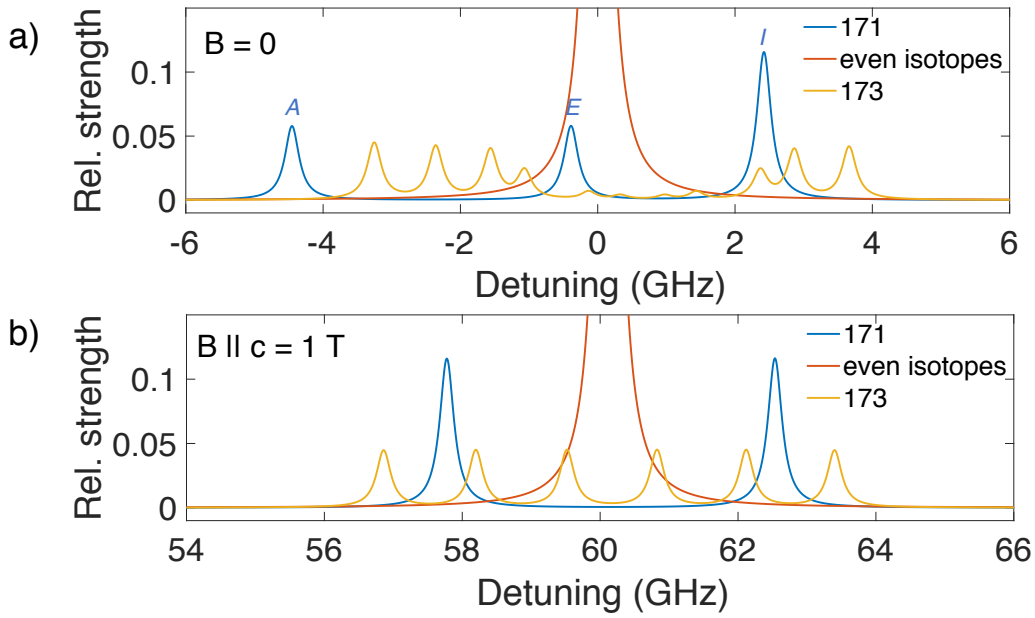

Figure 7.2: Allowed optical transitions for $E||c$ at a) zero applied magnetic field and b) $B||c = 1$ T for the different isotopes of 171. Transitions are scaled by the natural isotopic abundance. At zero applied magnetic field, we see that one of the 171-isotope transitions (transition A at -4.45 GHz) does not overlap with any transitions from the other isotopes.

7.2 Zero-field level structure and initialization

The energy level structure of Yb-171 at zero field and the corresponding optical and microwave transitions relevant to the following experiments are shown in Fig. 7.2. The ground-state spin transition of interest at zero field is the ZEFOZ transition introduced earlier between $|0\rangle_g = \frac{1}{\sqrt{2}}\left(|\uparrow\Downarrow\rangle_g - |\downarrow\Uparrow\rangle_g\right)$ and $|1\rangle_g = \frac{1}{\sqrt{2}}\left(|\uparrow\Downarrow\rangle_g + |\downarrow\Uparrow\rangle_g\right)$. This transition occurs at $\nu_g \approx 675$ MHz. I will refer to these two states in the rest of the text as the qubit subspace. Note that I have changed the naming convention slightly from that used in Chapter 3, where I referred to these as levels $|3\rangle$ and $|4\rangle$. I will refer to the lowest energy levels in the ground state as $|aux\rangle$. I have labeled the optical transitions with the same convention used previously, where the blue (red) transitions correspond to those allowed for light polarized parallel (perpendicular) to the c-axis of the crystal. The blue transitions are the Purcell-enhanced transitions aligned with the cavity mode.

We will use the lowest frequency optical transition (A) to readout the state of the ion. This is primarily chosen because this transition does not overlap with the in-

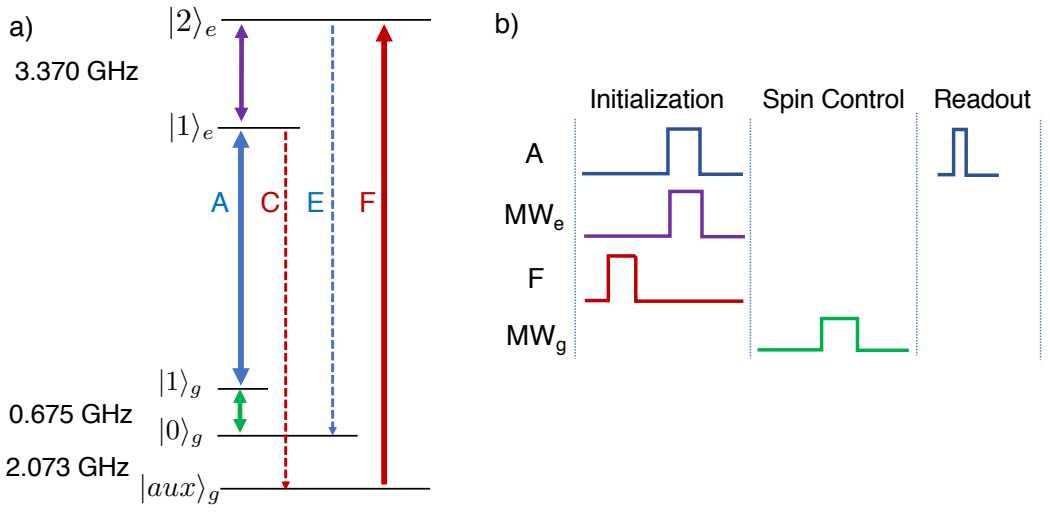

Figure 7.3: a) Level structure of ^{171}Yb:YVO_4 relevant to measurements of single ions. Transition A is used as the readout transition that measures the population in $|1\rangle_g$. Transition F is used to pump population from $|aux\rangle$ into the qubit subspace $\{|0\rangle_g, |1\rangle_g\}$ via cavity-enhanced decay on E. Microwave pulses are applied on the ground (green) and excited (purple) state ZEFOZ transitions. b) General sequence used for spin measurements. Spin is initialized into $|0\rangle_g$ through pumping on F and then simultaneous pumping on A and the excited state microwave transition. A spin control pulse or sequence is applied on the ground state spin transition and the population in $|1\rangle_g$ is readout optically in PL by pulsed excitation on transition A.

homogeneous distribution any optical transitions from other isotopes as discussed previously. The other cavity-coupled transition from this subspace (transition E) overlaps with the inhomogeneous distribution of the the zero-spin isotope. In the relatively high doping concentration in this device, this makes it difficult in practice to address this transition without exciting a large number of zero-spin ions. This is fine for optical pumping (we just need to make sure we wait long enough for these other ions to decay so we do not collect spurious photons from them), but is unacceptable for state readout. In samples with lower concentration, we will have a better chance of isolating this other transition and performing similar correlation measurements to those demonstrated on the ZNS ion.

The first experimental task is to initialize the ion into the $\{|0\rangle_g, |1\rangle_g\}$ subspace. We can do this by optically pumping out of $|aux\rangle$ on the transitions allowed for the orthogonal polarizations, either transition C or transition F in Fig. 7.2. The next task is to initialize the ion into $|0\rangle_g$ or $|1\rangle_g$. As a direct optical lambda system

is not allowed between these states, we need to use multiple transitions to make this happen. Here, we overcome this challenge by introducing a microwave tone to drive the $|1\rangle_e \rightarrow |2\rangle_e$ excited state transition while simultaneously pumping on the readout transition A. In this way, we can induce a transition from $|1\rangle_g \rightarrow |2\rangle_e$. Once in $|2\rangle_e$, the ion decays to $|0\rangle$ by the cavity-enhanced transition E. This enables efficient initialization of the ion into the $|0\rangle$ state. We then transfer the ion into $|1\rangle$ by applying a microwave pulse (e.g. π-pulse) on the $|0\rangle \rightarrow |1\rangle$ transition.

I will note that initialization could also be accomplished all-optically if desired or necessary by introducing another optical pumping frequency (e.g. pumping on transitions C and H). For our purposes, it was more straightforward experimentally to introduce a second microwave tone rather than a third optical frequency.

7.3 Identifying single 171 ions

The first experimental task is to find an isolated Yb-171 ion. We start with a fine PLE scan of the inhomogeneous distribution around the isolated Yb-171 transition (transition A). This corresponds to the region highlighted with a green box in the wide PLE scans presented in the previous chapter (See Fig. 6.2). Fig. 7.4 is an example of one such scan in which we identify a few isolated peaks corresponding to potential single Yb-171 ions. The inset shows a finer scan over the ion marked as **A**, where at the lowest power used for the measurement we extract a linewidth of 4.5 MHz. At the power used for this scan, we still observe a substantial contribution of power broadening to the observed linewidth. The reduction in SNR at lower powers due to decreased excitation probability and optical pumping discouraged us from spending more time pursuing measurements of the optical linewidth in this fashion. Later on, we will instead infer this linewidth from optical Ramsey measurements.

To determine whether a peak corresponds to a Yb-171 ion, the readout pulse is tuned on resonance with one of these peaks and a second laser is scanned across transitions C or F. If an observed peak corresponds to the A transition of a Yb-171 ion, population will move into the qubit subspace as the pump laser come into resonance with these transitions and result in an increase in counts after the readout pulse.

Fig. 7.5 shows examples of these scans performed on the three ions previously identified. In this case, the pumping laser is scanned over transition F. For ions **A** and **C**, a splitting of this transition is observed that is unexpected for the ion

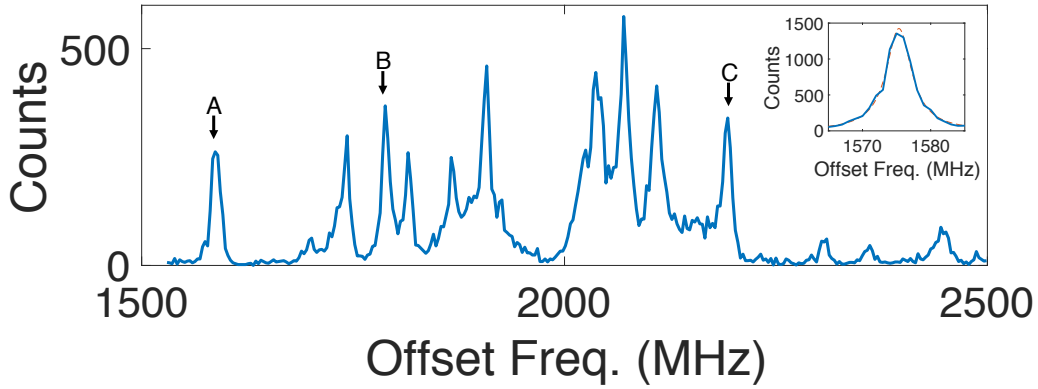

Figure 7.4: Fine PLE scan over the inhomogeneous distribution around transition *A*. Note that the frequency is referenced to the cavity offset lock. Ions identified as isolated Yb-171 ions studied here. Inset shows fine scan around ion **A** with power-broadened linewidth (FWHM) of 4.5 MHz.

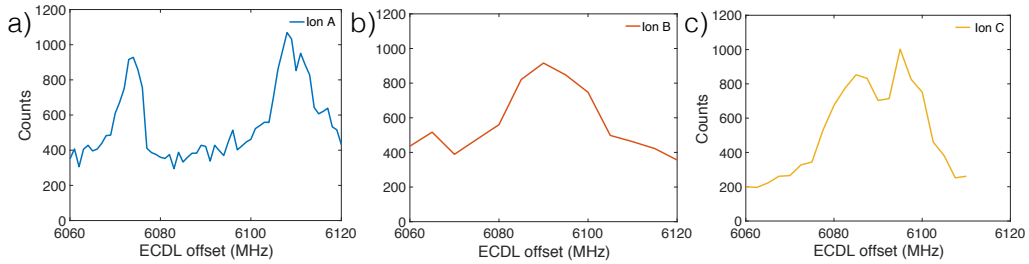

Figure 7.5: Verification that ions **A**, **B**, and **C** are Yb-171 ions. An initialization pulse is applied on transition F and followed by a microwave pulse on the ground state transition to move population into $|1\rangle_g$. The population in $|1\rangle_g$ is measured as a function of initialization pulse frequency offset. The splitting of transition F for ions **A** and **C** are currently attributed to strain as explained in the text.

at zero magnetic field. Similar results are observed when pumping on transition C. Further investigations into the behavior of this splitting in an applied magnetic field indicate that this is not due to a residual magnetic field at the ion. The current hypothesis is that this splitting is due to these ions occupying a strained or otherwise distorted sites. This is not unreasonable as we are in practice selecting for strained ions by working in the tails of the inhomogeneous distribution, which arises due to variations in the local environment within the crystal. A distortion to the local crystal lattice can lower the site symmetry of the ion and lead to a breaking of the degeneracy of the lowest energy levels. Further studies are necessary to understand the nature and cause of this strain and its consequences for the properties of the ion.

One interesting implication of this splitting is that these states are also then expected to be ZEFOZ states (similar to what is seen in the Yb:YSO [74]). An indication that this could be the case is the relatively narrow linewidth of the optical transition F for ions **A** and **C** compared to ion **B**. Depending on the resulting site symmetry of the ion, there is a chance that the ion would now possess a DC stark shift [127]. This would have negative implications for long-term spectral diffusion due to fluctuating electric fields, but would also open the door to tuning of the optical transition through applied DC electric fields. The main experimental consequence for now is that we must pump on both of these transitions to efficiently initialize the ion into the qubit subspace. Luckily, this splitting is small and we can readily address both transitions by frequency shifting with an AOM.

For the rest of the chapter, I will present results from ions **A** and **C** as these two are observed to be the most well-isolated ions. Although our sample size is small at this point, preliminary measurements have not shown any noticeable difference between the coherence properties of strained and unstrained ions.

7.4 Photon correlation measurements

After identifying potential Yb-171 ions, we can measure the $g^{(2)}[0]$ to further verify that these are indeed single ions. Fig. 7.6 shows the results of $g^{(2)}$ measurements on ion **A**. In Fig. 7.6 a, the $g^{(2)}$ is measured by alternating between a single initialization pulse on the C transition and a readout pulse on transition A. The pulse-wise correlation is calculated on the counts observed after exciting on transition A, which gives $g^{(2)}[0] = 0.147 \pm 0.011$. We note a bunching behavior similar to that observed with the ZNS isotope in an applied magnetic field. As discussed in the previous chapter, this bunching is expected for a multi-level emitter with long-lived ground states.

The amplitude of this bunching corresponds to the ratio of rates into and out of the read transition. We expect that this effect would not be observed with perfect initialization of the ion before each readout. To allow for a faster repetition rate, this experiment is performed using only a single optical pumping pulse. This is not sufficient to initialize the ion completely and leads to the observed bunching behavior.

We can demonstrate that this bunching behavior is related to a population effect by further modifying the optical pumping rates. Fig. 7.6a shows a $g^{(2)}$ measurement in which there is not any initialization sequence between read pulses. In this case,

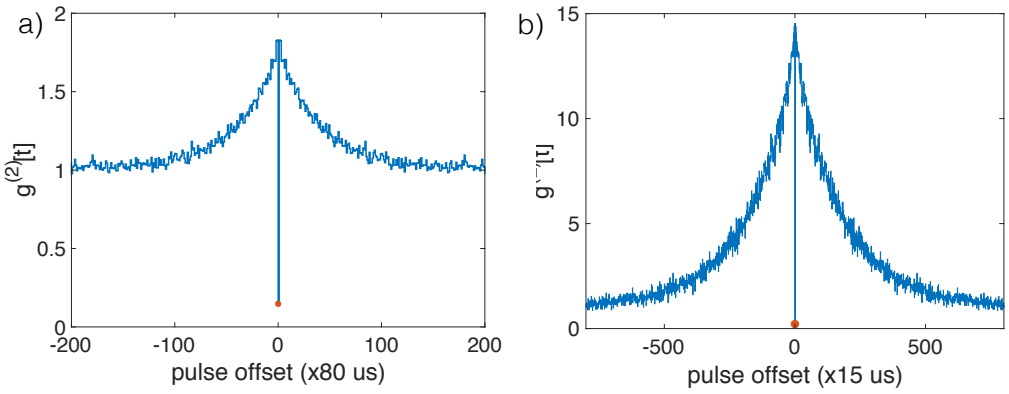

Figure 7.6: Second-order photon correlation measurements on ion A. a) $g^{(2)}$ performed with single initialization pulse before readout resulting in $g^{(2)}[0] = 0.147 \pm 0.011$. b) $g^{(2)}$ performed with no initialization pulse before readout showing increased bunching for $t > 0$ and $g^{(2)}[0] = 0.215 \pm 0.084$.

there is a much more pronounced bunching effect for $t > 0$ and we measure a $g^{(2)}[0] = 0.215 \pm 0.084$. Again, this increase in bunching as the pumping rate into $|1\rangle_g$ is reduced can be expected from the analysis presented in the previous chapter. Measurements on ion **C** show similar behavior and give $g^{(2)}[0] = 0.30 \pm 0.03$. These results indicate that we have correctly identified **A** and **C** as single ions.

7.5 Lifetime measurements

We can then measure the cavity-enhanced lifetimes of theses ions to determine their coupling to the cavity. Fig. 7.7 shows the results of lifetime measurements ions **A** and **C**, which give nearly identical optical lifetimes with $T_1 = 2.3\ \mu s$. This is a reduction from the bulk lifetime by $\beta F_p \approx 116$ and corresponds to a coupling of $g = 2\pi \times 22.8$ MHz. Identifying two similarly coupled ions in the cavity is an exciting prospect for future measurements of photon indistinguishability between two single rare-earths and perhaps even entanglement of two ions in the same cavity.

7.6 Spectral diffusion

We briefly investigate the long-term spectral diffusion of ion **A**. Fig. 7.8a shows repeated PLE scans over ion **A** over 6 hours. The integrated counts for this scan are shown Fig. 7.8b, which is well-fit to a Gaussian with FWHM of 5.2 MHz. We note the presence of an ion that is weakly coupled to the cavity about 10 MHz detuned from ion **A**. The long-term linewidth is similar to the single scan linewidth

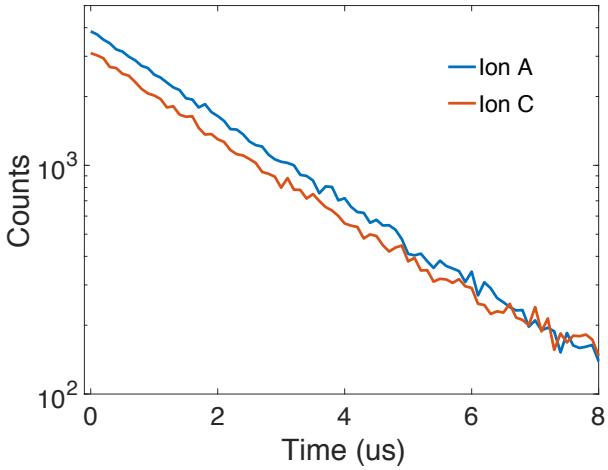

Figure 7.7: Optical lifetime measurements on ions A and C that give Purcell-enhanced lifetime of $T_1 = 2.3\ \mu s$.

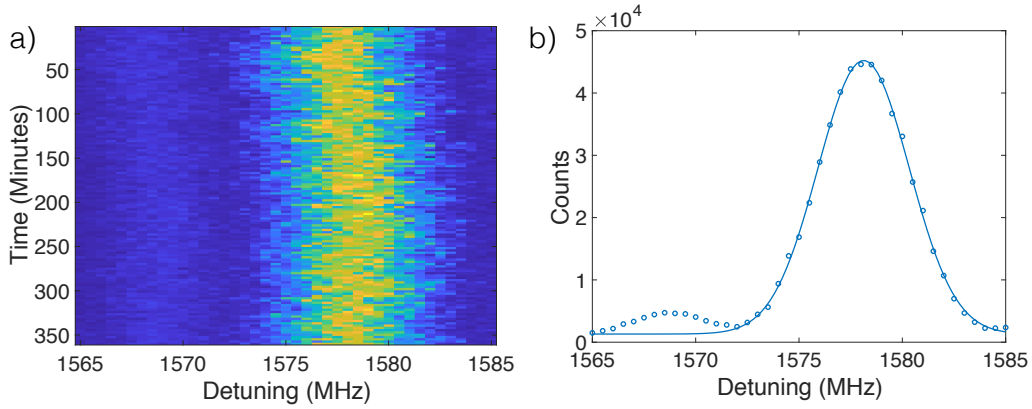

Figure 7.8: a) Repeated scans over ion **A** to investigate long-term spectral diffusion. b) Integrated counts from spectral diffusion scan fit to Gaussian with FWHM of 5.2 MHz.

measured at this optical power, which demonstrates that there is not significant long-term spectral diffusion. Further studies are necessary to determine the causes and limits of the observed broadening.

7.7 ODMR measurements

We then explore microwave manipulation of the Yb-171 spin states starting with optically detected magnetic resonance on the ground state. For this measurement, the ion is pumped into the qubit subspace on transition F, a microwave pulse is applied, and the population in state $|1\rangle_g$ is read out optically via transition A. When

the microwave pulse is off-resonance with the ground state transition, the repeated pumping on F and read-out on A will eventually move the population primarily into $|0\rangle_g$ in the steady state. When the microwave is on resonance with the ground state transition, this population is transferred to state $|1\rangle_e$ and will lead to a corresponding increase in the count rate of the optical readout.

Fig. 7.9 shows ODMR scans on the ground state ZEFOZ transition as the microwave drive power is reduced. We extract an ODMR linewidth of 175 kHz at the lowest powers used for this measurement. This is almost two orders of magnitude smaller than what was observed in ODMR for the zero-spin isotope and is a promising first sign for the coherence properties of the spin. At the lowest power scans performed, we still observed signs of power broadening on the microwave transition. Rather than pursue lower power ODMR measurements, we instead moved to coherent measurements that will be discussed in the upcoming sections. We note a slight asymmetry in the ODMR lineshape. Preliminary simulations by an undergraduate in our group, Yan-Qi Huan, indicate that this asymmetry agrees well with what is expected from the superhyperfine interaction with the nuclear spins of the host material (i.e. yttrium and vanadium).

We are also interested in driving the excited-state microwave transition to implement the proposed spin initialization scheme. To perform ODMR on the excited

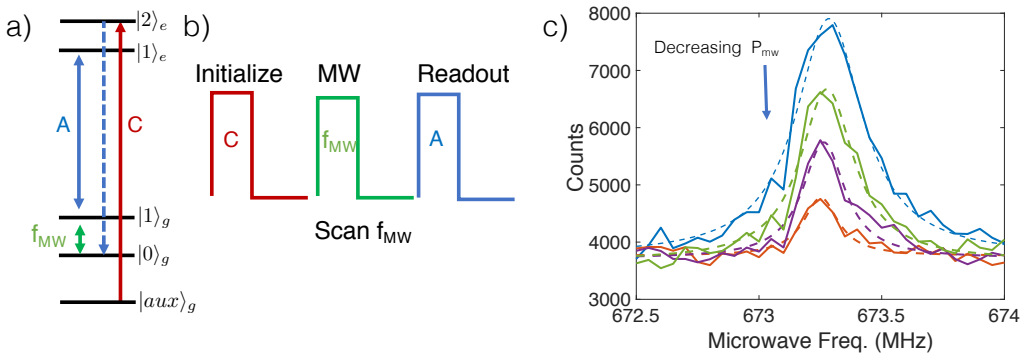

Figure 7.9: Ground-state ODMR. a) Energy level diagram with relevant optical and spin transitions. b) Sequence for measuring ground-state ODMR. The ion is optically pumped into $|0\rangle_g$ followed by a microwave pulse. The population in $|1\rangle_g$ is measured as a function of microwave frequency. c) Examples of ground-state ODMR with microwave power decreasing in steps of 5 dB. Lorentzian fit at the lowest power (red) gives a linewidth of 175 kHz (FWHM).

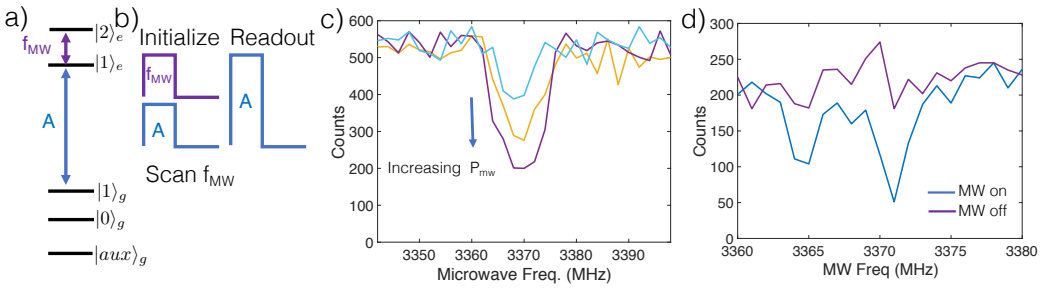

Figure 7.10: Excited state ODMR. a) Energy level diagram with relevant optical and spin transitions. b) Sequence for measuring excited state ODMR. To initialize, the ion is excited on A while simultaneously driving the excited-state microwave transition. The population in $|1\rangle_g$ is measured as a function of microwave frequency. c) Example of excited state ODMR for three different powers. d) Observation of Autler-Townes splitting on the optical transition observed for high initialization powers on transition A. Blue corresponds to microwave pulses on and purple is a background reference with the microwave pulses turned off.

state, optical pumping is performed by exciting on readout transition A while simultaneously driving the excited state microwave transition. On resonance, this will pump population out of state $|1\rangle_g$ and result in a corresponding drop in the count rate on the optical readout via transition A. Fig. 7.10b is an example of such an ODMR scan on the excited state. During this measurement, the microwave frequency was dithered to reduce the sensitivity of the ODMR signal to changes in the optical power on transition A. For optical Rabi frequencies greater than the transition linewidth, an Autler-Townes splitting of the excited-state transition can be observed with this ODMR measurement as shown in Fig. 7.10c.

7.8 Spin initialization

We then perform the full spin initialization sequence described earlier. To demonstrate and assess the quality of this initialization, the population in $|1\rangle_g$ is measured for varying lengths of the preparation sequences used to initialize the ion into $|1\rangle_g$ or $|0\rangle_g$

Fig. 7.11a shows initialization between the two levels of the qubit as the number of pulses on A is increase while holding the number of pulses on F fixed at 150. On transition A, this preparation consists of 2.5 μs pulses with a 200 kHz repetition rate. On transition F, the preparation pulse consists of two 2.5 μs pulses alternating between the two strain-split transitions observed earlier with a total repetition

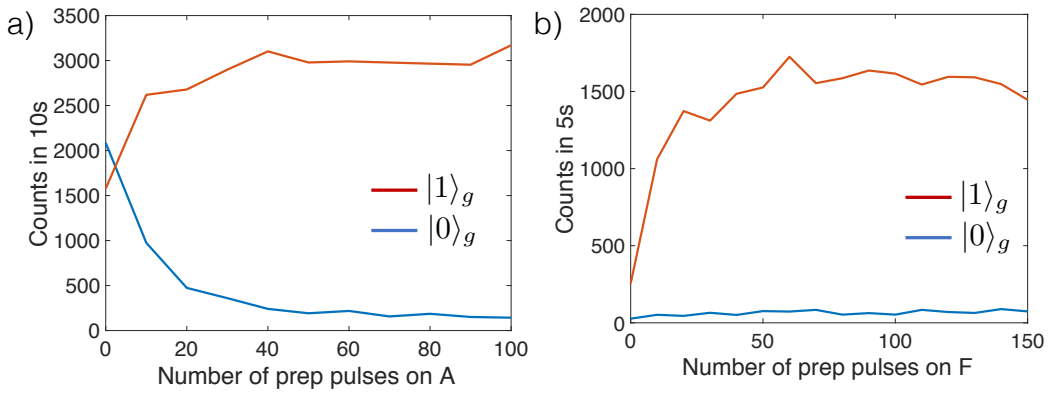

Figure 7.11: Example of spin initialization. Blue (red) scans correspond to preparation into $|0\rangle_g(|1\rangle_g)$. a) Increasing number of preparation pulses on transition A while holding number of preparation pulses on F fixed at 150. b) Increasing number of preparation pulses on transition F while holding number of preparation pulses on A fixed at 100.

rate of 100 kHz. The blue scans correspond to preparation into $|0\rangle_g$ and the red scans correspond to preparation into $|1\rangle_g$ by applying a microwave π pulse on the ground state transition after the optical initialization sequence. Without any subtraction of background count contributions, the observed contrast corresponds to an initialization of $> 91\%$ within the qubit subspace. This demonstrates that this pumping scheme allows for efficient initialization between these two spin states in under 500 μs

We demonstrate saturation of the optical pumping out of the $|aux\rangle$ state by performing the same measurement while keeping the number of initialization pulses on A fixed at 100 and varying the number of pulses on F. This is shown in Fig. 7.11b. Saturation of the initialization is observed for more than 100 pulses, which indicates that we are doing as well as we can for this pumping scheme. From the measured count rate and knowledge of the optical branching ratio and detection efficiency, the initialization into the qubit subspace is estimated to $> 95\%$. More direct measurements of this initialization are currently being explored, but we do not have a better estimate at the time of writing. We are working to improve both of these initialization fidelities. In an upcoming section, we will explore a readout sequence that will allows for post-selection to ensure the ion was in the qubit subspace at the time of measurement.

7.9 Coherent optical measurements

With the ion initialized into state $|1\rangle_g$, we turn to measurements of the optical coherence properties.

Fig. 7.12 shows optical Rabi oscillations on transition A at five different optical powers. Note that the plots are offset for clarity and the number of counts at zero pulse length is the same for each plot. Fig. 7.12 shows finer detail of an optical Rabi oscillation at the power typically used for the optical readout. An additional beating on these Rabi oscillations is observed and further revealed in an FFT of the signal. This is currently attributed to the superhyperfine interaction with neighboring vanadiums. Further investigations of the optical Rabi oscillations in different magnetic field configurations and different optical powers would be one way to extract more information about this coupling and the dynamics of the spin bath contributing to dephasing [136]. These measurements show that we can perform coherent manipulation on the optical transition. This allows for the identification of optical π-pulses that we then use to increase the efficiency of the readout of the ground state population. The ability to perform coherent control pulses on the optical transition also allows for further measurements of the optical coherence lifetimes. Fig. 7.13a shows the results of an optical Ramsey measurement on ion A. An exponential fit gives $T_2^* = 1.54$ μs, which corresponds to a linewidth (FWHM) of $2\gamma_d = 1/(\pi T_2^*) \approx 200$ kHz. Optical echo measurements were then performed to rephase slow frequency fluctuations of the ion (or laser) over the course of the measurement. Fig. 7.13a shows the results of an optical echo measurement with fit that gives $T_2 = 3.1$ μs. This is a significant improvement from the optical coherence times observed with the zero spin isotope, but is not quite at the desired lifetime limit ($T_2 = 2T_1$). Based on the analysis presented in chapter 4, this limit can in principle be attained through further reductions of the cavity-enhanced lifetime.

While the cavity brings the ions toward lifetime-limited coherence by reducing T_1, we must also keep in mind the overall reduction in the coherence time from this lifetime contribution. The total dephasing rate is the sum of contributions from both lifetime and excess dephasing processes:

$$\frac{1}{T_2} = \frac{1}{2T_1} + \gamma_{deph}. \tag{7.3}$$

Fig. 7.14 plots the corresponding bulk coherence time as a function of cavity T_2 for $T_{1,cav} = 2.3$ μs assuming that γ_{deph} remains constant. The corresponding bulk co-

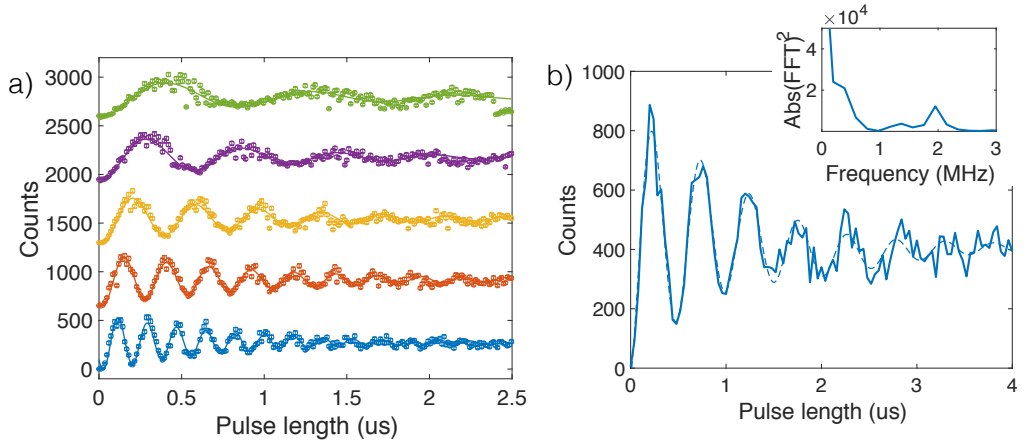

Figure 7.12: Optical Rabi oscillations on transition A. a) Examples of Rabi oscillations as the optical power is increased by 2x in each scan from top to bottom. Scans are offset for clarity and all start at 0 counts. b) Example of optical Rabi oscillation showing additional beat frequency with inset showing FFT of signal.

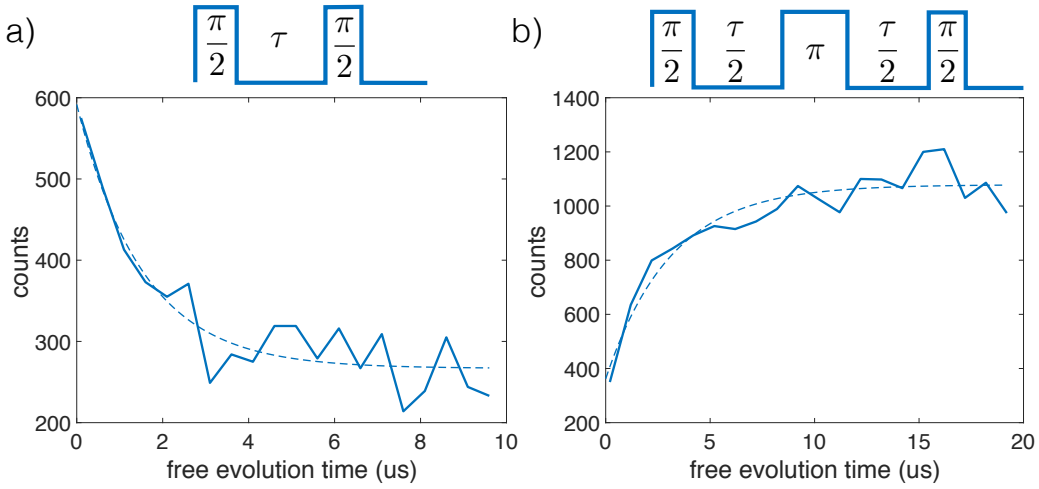

Figure 7.13: Optical coherence measurements on transition A. a) Optical Ramsey sequence and measurement for free evolution τ. Exponential fit gives $T_2^* = 1.54$ μs. b) Optical echo sequence and measurement for free evolution τ. Exponential fit gives $T_2 = 3.1$ μs.

herence time for the measured cavity T_2 is 9.3 μs. This is shorter than the coherence lifetime in preliminary measurements of the 100 ppm Yb-171 sample. A complementary measurement to do in the future would be measuring the optical coherence time of the ion as the cavity is detuned from resonance. This was explored in the context of the singles work in Nd:YVO and would give a better sense of lifetime

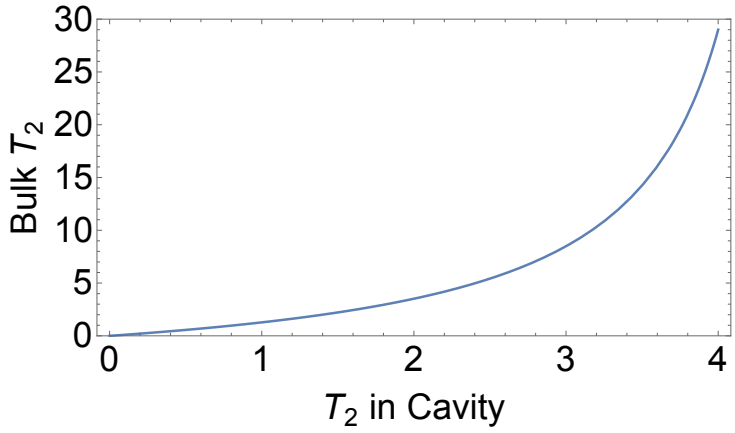

Figure 7.14: Plot of Eq. (7.3) to corresponding bulk T_2 from measured cavity T_2 with cavity-enhanced lifetime of $T_1 = 2.3$ μs.

contributions to the coherence. Ultimately, we are more concerned about the T_2^*, as this will impose the limit to the indistinguishability [109]. It should be noted that at the time of writing we have started to explore the optical coherence lifetimes of other ions in this cavity and see signs of variability on the measured values of T_2^* from ion to ion that indicate the average coherence lifetime might be lower than that measured above. Moving forward, it will be important to expand these measurements to multiple ions and different devices to build up the statistics required to better understand the observed variability.

At this point, there is not sufficient data to point to what might be limiting the optical coherence lifetimes in this sample. Further measurements in the bulk material will shed some light on this question. The key question at the moment is whether this coherence time is limited by magnetic field fluctuations, e.g. due to neighboring Yb spins or the nuclear spins of the host material, or through some other source of decoherence. If it is due to neighboring Yb spins, there is hope to improve this by moving to samples with lower doping concentrations. If it is due to host nuclei, then we need a way to better reduce the contribution from these ions. In either case, it is desirable to further reduce the sensitivity of the optical transition to magnetic field fluctuations if possible. We have not yet studied the behavior of this optical coherence extensively with magnetic field. There is perhaps room for improvement by more accurately reaching the ZEFOZ condition with better zeroing of the magnetic field along all the crystal axes.

An alternative route to suppressing these contributions if longer optical coherence

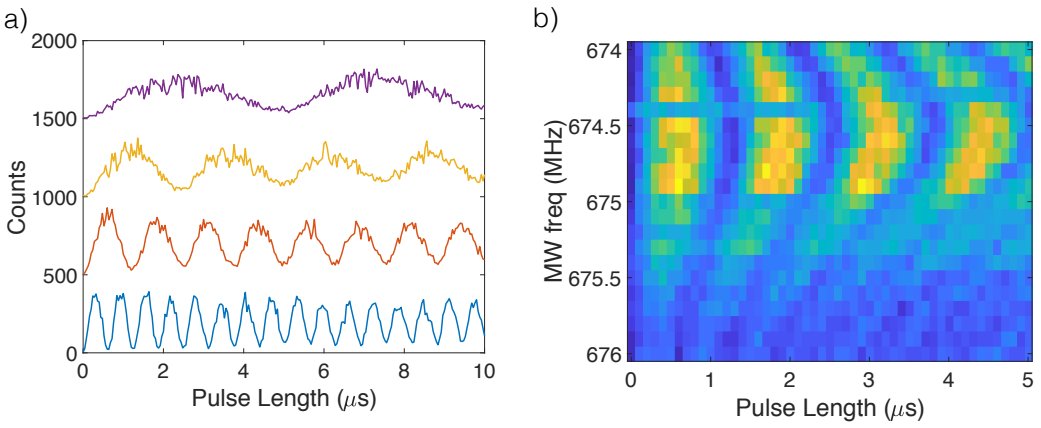

Figure 7.15: a) Rabi oscillations on the $|0\rangle_g \rightarrow |1\rangle_g$ transition as microwave power is increased in steps of 6 dB from top to bottom. b) 2D plot of Rabi oscillations as the microwave frequency is scanned.

times cannot be achieved at zero field will be to instead move to the high field limit. As mentioned, this will bring another set of experimental complications, but these should be readily overcome in the future. In either case, we can also hope to achieve better indistinguishability in the future through further reduction of the cavity-enhanced lifetime with improved device fabrication.

7.10 Coherent spin measurements

We then move to coherent measurements on the ground-state ZEFOZ transition ($|0\rangle_g \rightarrow |1\rangle_g$).

We start with Rabi oscillations by initializing the ion into $|0\rangle_g$ and then applying a microwave pulse on $|0\rangle_g \rightarrow |1\rangle_g$. The population in $|1\rangle_g$ is optically read out and recorded as a function of microwave pulse length. Fig. 7.15a shows examples of Rabi oscillations on the ground-state transition for four increasing microwave powers. We observe high-contrast Rabi oscillations out to pulse lengths greater than 10 μs. Fig. 7.15b shows a 2D plot of this measurement as a function of microwave frequency. These measurement demonstrate the ability to perform high-quality coherent manipulation on the ground-state transition of a single Yb-171 ion. Further, the measurements allow for the calibration of the π pulses necessary for further measurements of the coherence properties of this transition.

The spin T_2^* is measured using a Ramsey measurement as shown in Fig. 7.16a. In this measurement, the microwave frequency is detuned from the center of the

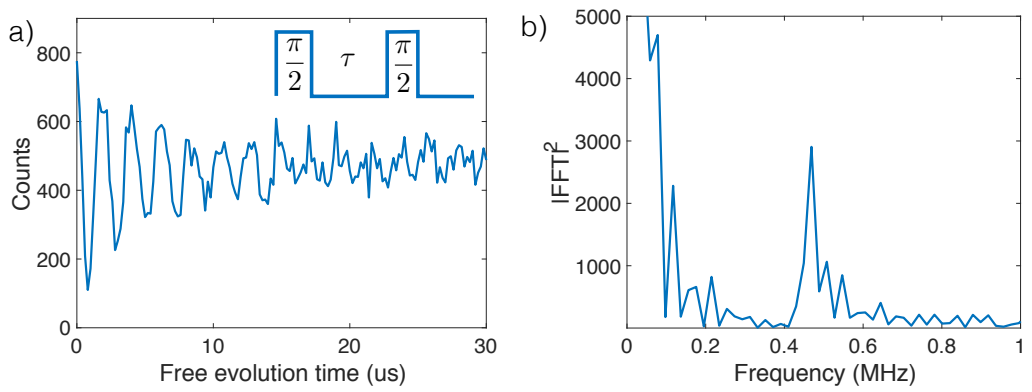

Figure 7.16: a) Spin Ramsey measurement at microwave detuning of ≈ 450 kHz. Single exponential fit gives a $1/e$ coherence time of $T_2^* = 8.2\ \mu s$. b) FFT of Ramsey measurement showing additional structure on oscillations.

transition by ≈ 450 kHz to give rise to fringes on the observed free induction decay. Fitting to a single exponential gives a $1/e$ coherence time of $T_2^* = 8.2\ \mu s$. We again notice a beating on these oscillations as revealed further by FFT (Fig. 7.16b). This is again attributed to the superhyperfine coupling with vanadiums in the host. Further studies of the decay and frequency composition of these fringes with magnetic field and detuning are needed to verify the nature of this interaction.

Spin echo measurements were performed to rephase quasi-static contributions to the dephasing and extract the spin T_2. Fig. 7.17a shows an example of one such spin echo measurement. We observe a non-exponential decay, which is characteristic of a spin coupled to a slowly-fluctuating dipolar spin-bath [139, 140]. Fitting this decay gives a $1/e$ decay of $T_2 = 43.5\ \mu s$. Fig. 7.17b shows the coherence time for a few values of magnetic field applied along the a-axis, where a drastic decrease in coherence time is observed as we move away from zero field. This provides confirmation that the coherence time is largely limited by magnetic field fluctuations as expected. The transitions move away from the ZEFOZ point as a external magnetic field is applied, which leads to an increase in the magnetic field sensitivity and results in a reduction in the coherence time. This indicates further zeroing of the magnetic field may lead to an enhancement of this coherence time. We currently do not have the ability to zero the magnet field along all axes simultaneously, but will have that capability on the next cooldown of this device.

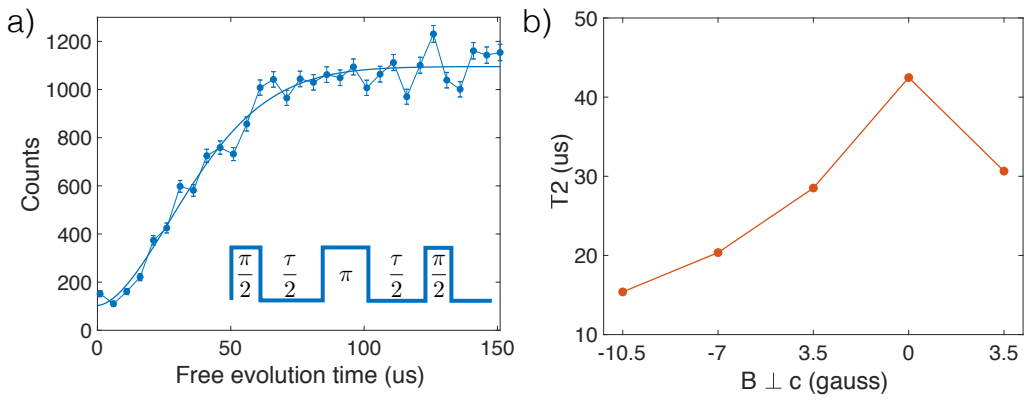

Figure 7.17: a) Spin echo measurement with fit to stretched exponential that gives $1/e$ decay of $T_2 = 43.5\ \mu s$. b) T_2 extracted from spin echo measurement as magnetic field is applied $\perp c$.

7.11 Extending the spin coherence

This coherence time is certainly acceptable for near term demonstrations in the lab setting e.g. establishing entanglement between two ions within the same lab [3], but the non-exponential decay of the echo amplitude suggests that we can hope to further extend this coherence time using dynamical decoupling (DD) sequences [141]. Measurements are ongoing as I write this thesis to understand and push the limits of the coherence time in this system. In this section, I will highlight some of our initial successes in extending the coherence time.

One straightforward DD sequence to implement is the Carr-Purcell-Meiboom-Gill (CPMG) sequence, which can be thought of as a multi-pulse extension of the spin echo measurement [141, 142]. This sequence takes the form:

$$\left(\frac{\pi}{2}\right)_x - \left(\frac{\tau}{2} - \pi_y - \frac{\tau}{2}\right)^N - \left(\frac{\pi}{2}\right)_x, \tag{7.4}$$

where N is the number of π pulses used in the sequence. The total free-evolution time in this system is then $\tau_{FE} = N\tau$.

Fig. 7.18a shows the results of CPMG measurements on ion **A**. For each scan, the number of π pulses is fixed and the pulse separation is scanned to extract a coherence time. The coherence time is extended with increasing number of π pulses, but pronounced oscillations are observed on the CPMG signal at high pulse numbers. This effect is indicative of coupling to other nuclei or noise sources in the crystal.

[3] For reference, it takes roughly 5 μs for light to travel a kilometer in fiber.

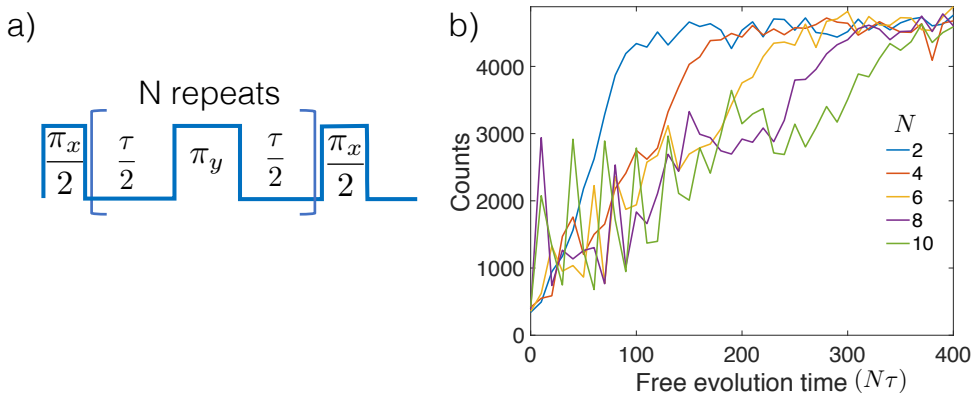

Figure 7.18: a) CPMG sequence. b) Initial CPMG measurements. For each scan, the number of π pulses is fixed and the pulse separation is scanned to extract $T_2^{(n)}$. The total free evolution time is given by τN. An increase in coherence time is measured with additional structure attributed to the superhyperfine interaction with host nuclei.

For instance, similar oscillations have been used to identify single ^{13}C nuclear spins coupled to nitrogen vacancies in diamond [143, 144].

Fig. 7.19 shows a finer scan over these oscillations for increasing numbers of π pulses. This data can be understood from the filtering function of the CPMG sequence [139, 142, 145]. Depending on the pulse separation, the filter function can act to suppress or amplify the contribution of a noise source at a given frequency. The coupling is maximally suppressed at π pulse separations of $\tau = 5.625$ μs. Further investigations are necessary to fully understand the nature of this coupling, but preliminary simulations of the superhyperfine interaction once again suggest this corresponds to coupling with the nearest neighbor vanadiums. Moving forward, such CPMG measurements would enable more detailed noise spectroscopy on the ion and its environment [145, 146]. One next step will be to expand on these measurements and fully reconstruct the noise spectrum as done in e.g. [146].

For our current investigation, we want to suppress this coupling and set the delay between π pulses to maximize the observed coherence. Fig. 7.20 shows the results of the CPMG scan where the separation between π pulses is fixed to 5.625μs and the coherence is measured by increasing the number of π pulses. Working at this optimal pulse separation gives rise to a spin coherence time of 18 ms, which is a

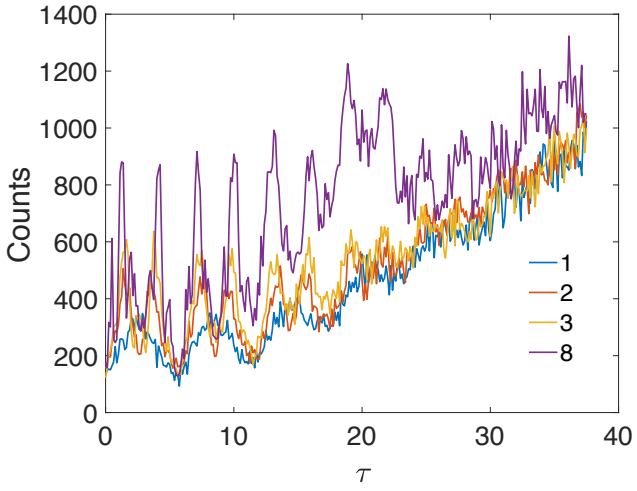

Figure 7.19: Finer CPMG scans for increasing number of π pulses. Plotted in terms of τ to allow for direct comparison between scans.

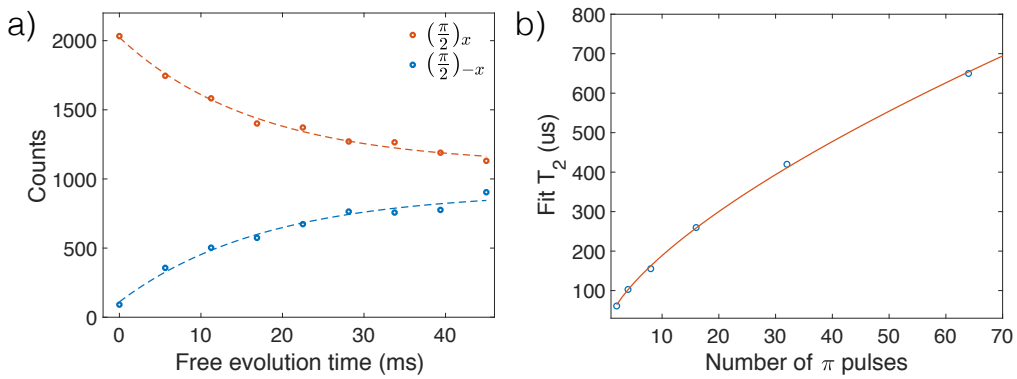

Figure 7.20: a) Measurement of CPMG coherence time with $\tau = 5.625\ \mu s$ for increasing numbers of π pulses. The phase of the final $\pi/2$ pulse is alternated between 0 (red) and 180° (blue) to generate a differential signal. Fit gives $T_2^{(n)} = 18$ ms. b) Scaling of $T_2^{(n)}$ with the number of π pulses using multiples of $\tau = 5.625\ \mu s$. Fit gives $N^{0.67}$ scaling.

significant improvement and a promising result for this system.

While the CPMG sequence is not capable of preserving arbitrary quantum states, measurements are underway investigating other DD sequences for this purpose [141]. For instance, preliminary measurements with XY8 sequences demonstrate coherence times longer than 4 ms. These sequences are less robust to pulse error, so with more optimization we are optimistic that this will improve further.

We can learn more about the nature of the source of dephasing from the scaling of the CPMG coherence lifetime with number of π pulses as shown in Fig. 7.20b. For this measurement, the number of π pulses is fixed and the interpulse separation is scanned as shown in Fig. 7.18. The π pulse separations are chosen to be multiples of 5.625 μs to extract the decay envelope. This scaling is well-fit to a power law $N^{0.67}$. This almost matches perfectly with the $N^{2/3}$ scaling expected for dephasing dominated by coupling to a dipolar spin bath [147, 148].

While we will not be limited by this coherence time in the near future, we are still working on understanding the upper limits to this coherence. A main question at this point is distinguishing the dephasing due to zero-spin Yb isotopes and nuclear spins. This will be best explored by looking at samples of varying concentrations. One limit to the performance of dynamical decoupling could be related to pulse errors. In this case, we could hope to improve with better calibration of the microwave π pulses and improvements to the amplitude stability of the microwave pulses. Another source of decoherence could be microwave heating from the large number of pulses required to reach those coherence times. In future, this could be overcome with the use of superconducting materials rather than a gold stripline to reduce ohmic heating.

7.12 Spin lifetime

Ultimately, the upper limit on the spin coherence will be determined by the spin state lifetime. Here a measurement of the spin lifetime is performed by initializing the ion into $|1\rangle_g$ or $|0\rangle_g$, letting the populations decay for time τ and then reading out the population of $|1\rangle_g$. Fig. 7.21 shows the result of one such lifetime measurement. We see two different decay rates, which is expected due to the presence of the $|aux\rangle$ state. Each curve is fit to a single exponential to extract the fastest decay time, which gives a decay time of 22 ms for the ion initialized in $|0\rangle$ and 34 ms for the ion initialized into $|1\rangle$. This then means the measured coherence times are approaching the lifetime limit (see [147] for a discussion of the lifetime limit in a multi-level system).

The natural question is then: why is this lifetime so dang short? We expect if the lifetime was limited by spin-lattice relaxation, the lifetime would be decreased as the temperature of the device is increased. Measurements of both the spin lifetime and spin coherence lifetime show no signs of degradation as the device was warmed up from 50 mK to $\sim$ 1 K . Further measurements past 1 K were not performed

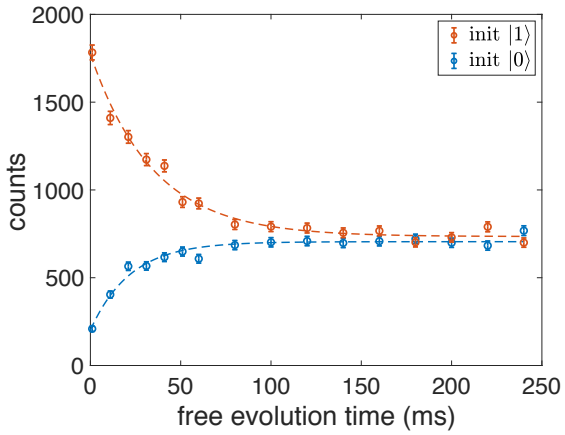

Figure 7.21: Measurement of spin lifetime. Ion is initialized into $|0\rangle$ (blue) or $|1\rangle$ (red) and population in $|1\rangle$ is measured as a function of free evolution time. Exponential fit to $|0\rangle$ ($|1\rangle$) trace gives 22 ms (34 ms).

as this is an awkward temperature range for the dilution fridge and we wanted to maintain low-noise operation of the SNSPDs that sit in the same fridge. Further studies are in progress to understand the limits of these spin coherence and lifetime times with temperature. The ability to achieve long coherence times in this system at temperatures higher than 1 K would be exciting in that it puts the system back in the range of He4 fridges.

The lack of temperature dependence would indicate that this lifetime is dominated by spin-spin relaxation in this regime. This is expected to be a dominant effect in this system due to the narrow inhomogeneous linewidths of the spin transition and the relatively high doping concentration. To further differentiate between the two mechanisms, more measurements are necessary in samples with different doping concentrations. Ultimately, we want to work with as low of doping concentration as possible to avoid these problems. Another path to reducing the spin-spin relaxation would be to intentionally try to broaden the spin inhomogeneous line further by codoping with other elements [149, 150].

7.13 Single-shot spin readout

For this system to be useful in a quantum network, we also need to demonstrate high-fidelity single-shot readout (SSRO) of the ion spin state. In this section, I present initial results demonstrating single-shot readout in this system.

For the first attempt at SSRO, the spin is initialized and read out optically with a

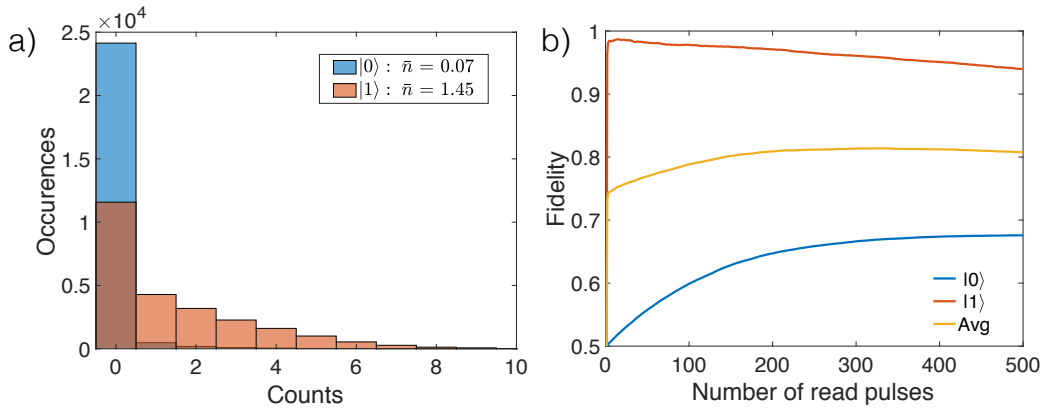

Figure 7.22: a) Distribution of readout counts for the ion initialized into state $|0\rangle$ (blue) and state $|1\rangle$ (red) for $N = 500$ readout pulses. b) Extracted readout fidelities for preparation into $|0\rangle$ (blue) and state $|1\rangle$ (red). The yellow trace shows the average fidelity. The maximum average fidelity for this measurement was $F_{avg} = (F_1 + F_0)/2 = 81.4\%$ with 322 read pulses.

series of read-out pulses on transition A. The goal is then to demonstrate that we can differentiate between the two states based on the number of photons measured in the readout sequence. We can assess this fidelity by looking at the distribution of counts observed when the ion is initialized into the two different ground states.

Fig. 7.22a shows the readout count distributions for the spin initialized into the state $|0\rangle$ (blue histogram) and state $|1\rangle$ (red histogram) for N = 500 read pulses. From this, we observe an average photon number of $\bar{n}_0 = 0.07$ when initialized into state $|0\rangle$ and $\bar{n}_1 = 1.45$ when initialized into state $|1\rangle$. We then choose a photon detection threshold of $n \geq 1$ to assign the ion to $|1\rangle$ and $n = 0$ to assign the ion $|0\rangle$. The readout fidelity F_i is extracted from this histogram and plotted in Fig. 7.22b as a function of the number of read pulses. The maximum average readout fidelity extracted from this data is $F_{avg} = (F_1 + F_0)/2 = 81.4\%$ with 322 read pulses. This is not a bad place to start, but we would like to improve upon this if possible.

First, we note that the histogram of counts observed for $|1\rangle$ follow a geometric distribution as expected for a finite branching ratio, but has an additional contribution at zero. This suggests that there is room for improvement in the initialization into state $|1\rangle$.

The ability to perform single-shot readout in this manner is currently limited by the photon collection efficiency and the cyclicity of the optical transition. As mentioned

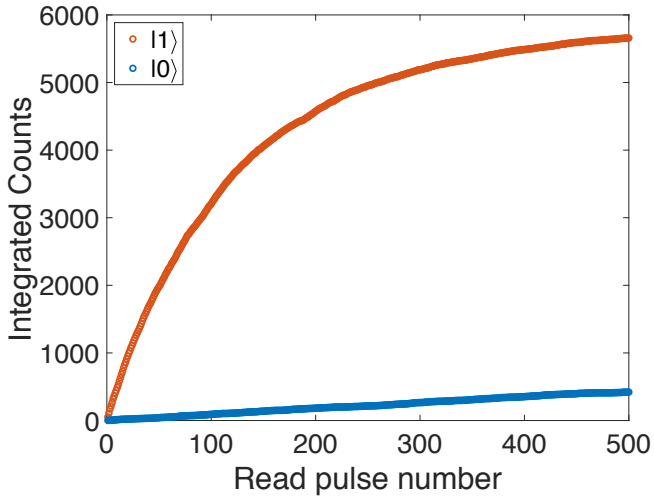

Figure 7.23: Measurement of optical branching ratio extracted from SSRO measurements. The ion is initialized into state $|0\rangle$ (blue) or state $|1\rangle$ (red) and the population in $|1\rangle$ is measured with a series of readout pulses The cumulative sum of the total counts measured in the experiment is plotted as function of the number of read pulses. Fit gives $\beta = 0.991$.

in the Chapter 4, Purcell enhancement can be used to enhance the branching ratio. The branching ratio can be extracted from the above measurement by summing the number of total counts observed as a function of number of read pulses. Fig. 7.23 plots the cumulative counts as a function of number of read pulses for the ion initialized into each of the two ground states. From this, we extract a branching ratio of 0.991, which is slightly lower than what is expected from the lifetime (0.994). Improvements to the branching ratio would allow for a greater number read pulses before the ion pumps away and would thus improve the readout fidelity. This can be achieved through higher Q devices that enable larger Purcell enhancement. Further improvements to the collection efficiency will also lead to significant gains in this readout fidelity.

We note that the current fidelity is largely limited by the ability to measure the ion when it is in state $|0\rangle$. A difficulty with a finite branching ratio is that the distribution of photon counts from the bright state will be geometric. This means that the fidelities measured in this way will always be skewed such that they are much better in detecting when the ion is in state $|1\rangle$ compared to state $|0\rangle$. Additionally, we must take into account the case of imperfect initialization where the ion is actually in the $|aux\rangle$ state at the time of measurement as this will also yield zero counts

upon readout and thus reduce the fidelity.

We are currently implementing a modification to the SSRO procedure to increase the readout fidelity of the ion in $|0\rangle$. This method essentially reads out the ion twice and takes advantage of the ability to measure population in $|1\rangle$ with high fidelity. Furthermore, this method verifies the ion was actually in the subspace of interest at the start of the measurement. This allows us to post-select and throwout the cases where the ion was in $|aux\rangle$ due to insufficient optical pumping. This will reduce the overall success rate (until we improve the initialization and detection efficiencies), but will lead to substantial improvements of the fidelity.

We can do this by taking advantage of the level structure and selection rules for the optical transitions in Yb-171. If we initialize the ion into $|1\rangle$ and readout for sufficiently long, the ion will be optically pumped out of the qubit subspace into the $|aux\rangle$ state as optical decay to $|0\rangle$ is forbidden. As shown previously, we can determine that the ion was in $|1\rangle$ with high fidelity. If we then apply a π pulse on the ground state transition and readout the state again, we expect to get zero counts as the ion will still be in the $|aux\rangle$ state. On the other hand, if we initialize the ion into $|0\rangle$ then we expect to get zero counts on the first readout cycle when reading out on transition A. This state is not optically pumped by excitation on A, so the ion will still be in $|0\rangle$ at the end of the first readout. If we then apply a π pulse on the ground state transition, the ion will be transferred into the $|1\rangle$ state. On the second readout cycled, we will then read this state out with high fidelity. If the ion starts in the $|aux\rangle$ state, then we will get zero counts on both rounds of the readout.

This scheme is summarized in Fig. 7.24. We readout with N pulses, apply a π pulse on the ground state transition, and then readout again with N pulses. Based on the state-detection threshold condition from the histogram above, we assign the state of the atom based on the number of photons observed during each of these sequences. Let a (b) be the state assigned in the first (second) sequence. If we measure $a = 1$ and $b = 0$, we then assign the ion to $|1\rangle$. If we measure $a = 0$ and $b = 1$, we then assign the ion to $|1\rangle$. In this way, we can then extract a post-selected single shot fidelity.

It is worth noting that this method relies on the pumping structure and the lack of an optical lambda system between the two ground states and the excited state we are using for readout. If the readout sequence moved population into $|0\rangle$ rather than $|aux\rangle$, we would not do any better than the initial single-shot readout attempt.

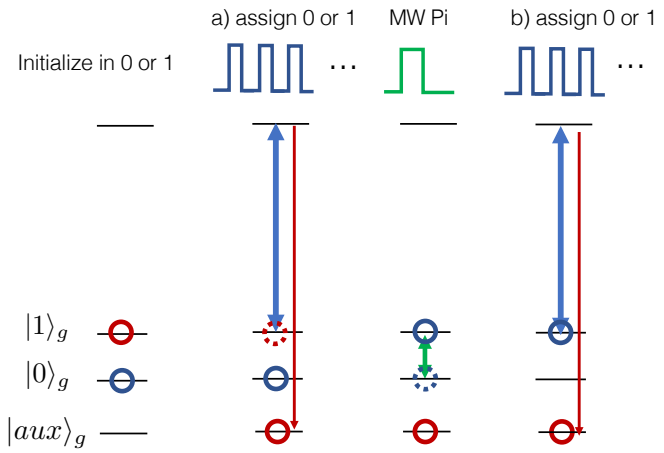

Figure 7.24: Improved single-shot readout scheme. Ion is initialized into $|0\rangle$ (blue) and $|1\rangle$ (red). After the readout sequence a, the population in $|0\rangle$ is unchanged while $|1\rangle$ is optically pumped to $|aux\rangle$. A microwave π pulse is applied, which transfers $|0\rangle$ to $|1\rangle$ while leaving the population in $|aux\rangle$ unchanged. This is followed by a second readout sequence b. This allows for a post-selected single-shot readout where the state is assigned to $|0\rangle$ if the outcome of the two rounds is $a = 0, b = 1$ and assigned to $|0\rangle$ if $a = 1, b = 0$.

Recent experiments show this to be a promising technique to achieve high-fidelity readout. Fig. 7.25 shows an example of this measurement. Fig. 7.25a shows photon count distributions measured for the two readout sequences with the ion initialized into each of the two ground states. Fig. 7.25b shows the average post-selected fidelity as described above for increasing number of read pulses compared to the average fidelity that would be extracted from just the first read sequence. In this measurement we see that this technique enables an increase in average readout fidelity from 78% to 96%. Further improvements to the single-read sequence fidelity through improvements to the branching ratio and detection efficiency will enable even higher fidelities with this method in the future.

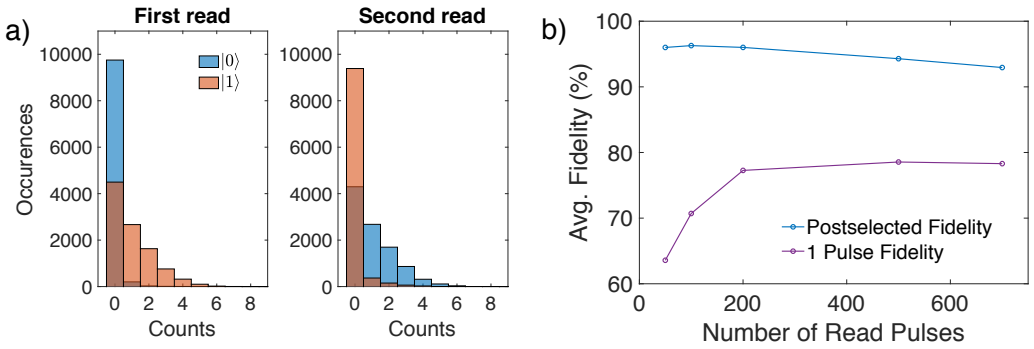

Figure 7.25: Implementation of improved single-shot readout scheme. a) Distribution of readout counts for the ion initialized into state $|0\rangle$ (blue) and state $|1\rangle$ (red) for the first and second readouts showing the expected behavior. b) Average fidelity for post-selected scheme compared to average fidelity extracted from only the first read sequence.

Chapter 8

FUTURE DIRECTIONS

In this chapter I discuss the questions that remain to be answered for this system and point to possible measurements to explore in the future.

8.1 Limitations to zero-field coherence lifetimes

One of the next major goals with this platform is the generation of indistinguishable photons. However, measurements of the optical coherence lifetimes at this point indicate that we are not yet near the lifetime-limit necessary to show high indistinguishability. Further studies in the device are warranted to understand if the observed coherence lifetimes so far are actually at the limit of what is achievable. Along these lines, more statistics on the coherence lifetimes of different ions within the cavity would be useful to determine whether this is for instance related to the observed strain splitting. Measurements of the coherence in the same bulk crystals as used for the device will be essential for further understanding of the mechanisms of the observed decoherence. After understanding and pushing the limits of the optical coherence, we should be able to further improve this indistinguishability with improved device fabrication and shorter cavity-enhanced lifetimes. If spectral diffusion (T_2^*) continues to be a problem, one could also imagine implementing a post-selection procedure similar to that used in NV centers to improve coherence in the presence of spectral jumps [137].

While the demonstrated $\sim$ 20 ms spin coherence lifetime is promising, it appears we may be approaching the lifetime limit in this sample. Further investigations of this lifetime with magnetic field and temperature should reveal whether this lifetime is limited by spin lattice relaxation or ion-ion interactions. Similar spectroscopy in the bulk material is necessary to verify that this is not intrinsic to ions in the cavity. If the lifetime is indeed limited by ion-ion interactions, the next step would be to move to samples with lower doping concentrations or larger spin inhomogeneous broadening to reduce such interactions. We are currently investigating a variety of sources for the YVO crystals in attempts to achieve lower doping concentrations. To achieve larger inhomogeneous broadening, we could investigate samples that are codoped with other ions such as europium or scandium to introduce more static strain within the sample [149, 150].

For further improvements to coherence lifetimes, another route to explore in the context of single ions will be the high-field regime presented in Chapter 3. In this regime, we observed two-pulse spin echo lifetimes of 6.6 ms at a temperature of $\sim$ 600 mK and magnetic field of 440 mT along the c-axis of the crystal in a significantly higher doping density sample (100 ppm). We expect this to improve even further at higher fields, lower temperatures, or lower doping concentrations as the contribution to dephasing from Yb-Yb interactions is reduced. These long coherence lifetimes could be extended even further with the use of dynamical decoupling sequences. The high-field limit would bring a new set of experimental challenges as discussed in Chapter 7, but there are no fundamental difficulties to moving to this regime in the future.

8.2 Coupling to nearby spins

One exciting aspect of this work is the coupling to nearby nuclear spins observed in the CPMG measurements. Straightforward extensions to the initial measurements presented here should allow for characterization and control over this coupling. These nuclear spins could then be harnessed as quantum memories to form a few-qubit quantum register [11, 151]. There is a lot to be explored here and this work will benefit greatly from the progress and techniques demonstrated with the NV center in diamond [11, 143, 144, 152, 153].

8.3 Toward generation of entanglement

Ultimately, the goal is to show that this system is a useful technology for quantum networks. As mentioned, one of the next major steps toward this goal will be the demonstration of indistinguishable photon emission. After showing improvements to the coherence lifetimes, we then want to show a direct measure of the indistinguishability. This can be done initially with photons from the same ion, but ultimately must be shown with two different ions.

We can directly measure the photon indistinguishability using a Hong-Ou-Mandel (HOM) interferometer [109]. To measure indistinguishability between a pair of photons from the single emitter, we can introduce an additional delay line such that we interfere photons from consecutive excitations of the same emitter. For this, we need the delay line to be significantly longer than the lifetime of the ion. Let's get an idea of the requirements of this experiment for the current device. As the fastest observed lifetime is $T_1 = 2.3$ μs, a delay time of a few lifetimes (let's say $4T_1$) corresponds to a delay line of $\approx$ 2 km. For single-mode fiber readily available

from Thorlabs [1], the quoted loss at 980 nm is < 2 dB/km. With the additional insertion loss of the necessary beamsplitters and fiber splices ($\approx$ 1dB total), this would bring the total detection efficiency from 1% to $\approx$ 0.3% for a two-photon detection probability of 9×10^{-6}. For the current Yb-171 singles, a reasonably optimistic estimate for the overall rate of photons generated within the device is 25 kHz given the 10 μs wait time between pulses, the branching ratio, and time necessary to reinitialize the system (2 ms). This then corresponds to ~ 0.2 two-photon coincidences per second. While certainly not impossible, this measurement would be also be made more challenging by the necessity of stabilizing the 2 km fiber interferometer. This particular measurement is then perhaps best suited for faster ions and thus faster experiments.

A more exciting measurement in the future will be to demonstrate indistinguishability between two separate ions. This is significantly more technically challenging overall, but is also a direct step toward entanglement of two ions. The main challenge to interfering single photons from ions in two different ions in two different devices will be the requirement of essentially doubling the experimental infrastructure. This is a significant undertaking, but should be accomplished with enough time, energy, and manpower. Of course, such measurements cannot be accomplished until the remaining questions about the properties of the system are sorted out.

Ultimately, measurements of indistinguishability of photons from separate emitters is the foundation for the demonstration of entanglement of two single rare-earths ions. We can get a sense of the entanglement distribution rates we might be able to achieve within the lab setting with reasonable improvements to the devices. We estimate this based on the well-known Barret-Kok scheme [154]. The success probability in this experiment is simply given by $P_s = \frac{1}{2} p^2 \eta_d^2$, where p is overall device system efficiency (i.e. probability that photon emitted by ion is coupled into fiber) and η_d is the detection chain efficiency.

For the current set of devices, we have $p\eta_d \approx 1\%$. Assuming two such devices could be made and similar efficiencies achieved, the overall success probability would be 5×10^{-5}. Assuming a 25 kHz average excitation rate as above gives a corresponding success rate of 1.25 Hz. The main limits on the system efficiency are the fiber-waveguide coupling and the waveguide-cavity coupling. Based on previously demonstrated devices, it is reasonable that we can improve this overall

[1] e.g. Thorlabs SM980G80

efficiency in the near term by a factor of at least 5. This then corresponds to a success rate of ~ 31 Hz for two ions in the same lab. Further investigations of the ultimate limits of the performance and collection efficiencies in these devices is warranted before making any further speculation. While these rates could enable near-term demonstrations in the lab, we ultimately want much higher count rates to account for fiber-loss when moving to larger scale implementations. In the long-term, the integration of ^{171}Yb:YVO_4 with fabrication architectures that allow for efficient coupling to fiber [50, 121, 155] will be an essential step in significantly improving these success rates.

8.4 Conclusion

In conclusion, this thesis has presented on recent progress toward building a nanophotonic quantum interface with ^{171}Yb:YVO_4 . We first investigated the properties of this previously unexplored material and found it will be useful for a variety of quantum technologies. Building on this work, we were able to optically detect and initialize single ytterbium ions coupled to a nanophotonic cavity. After exploring the properties of an ion with zero-nuclear spin, we showed that the hybrid electron-nuclear spin states of Yb-171 at zero-field enable strong transitions with reduced magnetic field sensitivity. Through the use of dynamical decoupling, we showed spin coherence lifetimes of up to 18 ms. We then made use of the zero-field level structure of ^{171}Yb:YVO_4 to demonstrate high-fidelity single-shot readout of the spin state. These results serve as the foundation for an exciting array of measurements to explore in the future and demonstrate that nanophotonic devices with ^{171}Yb:YVO_4 are a promising platform for solid-state quantum light-matter interfaces.

BIBLIOGRAPHY

[1] T. Zhong, J. M. Kindem, E. Miyazono, and A. Faraon, "Nanophotonic coherent light–matter interfaces based on rare-earth-doped crystals," Nature Communications **6**, 8206 (2015). x, 10, 11, 12, 34

[2] T. Zhong, J. M. Kindem, J. Rochman, and A. Faraon, "Interfacing broadband photonic qubits to on-chip cavity-protected rare-earth ensembles," Nature Communications **8**, 1–7 (2017). x, 13

[3] T. Zhong, J. M. Kindem, J. G. Bartholomew, J. Rochman, I. Craiciu, E. Miyazono, M. Bettinelli, E. Cavalli, V. Verma, S. W. Nam, et al., "Nanophotonic rare-earth quantum memory with optically controlled retrieval," Science **357**, 1392–1395 (2017). x, 14, 17, 34

[4] T. Zhong, J. M. Kindem, J. G. Bartholomew, J. Rochman, I. Craiciu, V. Verma, S. W. Nam, F. Marsili, M. D. Shaw, A. D. Beyer, et al., "Optically Addressing Single Rare-Earth Ions in a Nanophotonic Cavity," Physical Review Letters **121**, 183603 (2018). x, 8, 11, 15

[5] G. F. Koster, J. O. Dimmock, R. G. Wheeler, and H. Statz, *Properties of the thirty-two point groups* (The MIT Press, Cambridge, MA, 1963). xii, 24, 27, 144

[6] J. P. Dowling and G. J. Milburn, "Quantum technology: the second quantum revolution," Philosophical Transactions of the Royal Society A: Mathematical, Physical and Engineering Sciences **361**, 1655–1674 (2003). 1

[7] S. Wehner, D. Elkouss, and R. Hanson, "Quantum internet: A vision for the road ahead," Science **362** (2018). 1

[8] L. M. Duan and C. Monroe, "Colloquium: Quantum networks with trapped ions," Reviews of Modern Physics **82**, 1209–1224 (2010). 1

[9] N. Sangouard, C. Simon, H. de Riedmatten, and N. Gisin, "Quantum repeaters based on atomic ensembles and linear optics," Reviews of Modern Physics **83**, 33–80 (2011).

[10] A. Reiserer and G. Rempe, "Cavity-based quantum networks with single atoms and optical photons," Reviews of Modern Physics **87**, 1379–1418 (2015). 1, 75

[11] D. D. Awschalom, R. Hanson, J. Wrachtrup, and B. B. Zhou, "Quantum technologies with optically interfaced solid-state spins," Nature Photonics **12**, 516–527 (2018). 1, 2, 127

[12] W. B. Gao, A. Imamoglu, H. Bernien, and R. Hanson, "Coherent manipulation, measurement and entanglement of individual solid-state spins using optical fields," Nature Photonics **9**, 363–373 (2015). 2

[13] A. Faraon, C. Santori, Z. Huang, V. M. Acosta, and R. G. Beausoleil, "Coupling of nitrogen-vacancy centers to photonic crystal cavities in monocrystalline diamond," Physical Review Letters **109**, 2–6 (2012). 2, 79

[14] A. Sipahigil, R. E. Evans, D. D. Sukachev, M. J. Burek, J. Borregaard, M. K. Bhaskar, C. T. Nguyen, J. L. Pacheco, H. A. Atikian, C. Meuwly, et al., "An integrated diamond nanophotonics platform for quantum-optical networks," Science **354**, 847–850 (2016). 2, 50, 54

[15] R. E. Evans, M. K. Bhaskar, D. D. Sukachev, C. T. Nguyen, A. Sipahigil, M. J. Burek, B. Machielse, G. H. Zhang, A. S. Zibrov, E. Bielejec, et al., "Photon-mediated interactions between quantum emitters in a diamond nanocavity," Science **362**, 662–665 (2018). 2

[16] D. D. Sukachev, A. Sipahigil, C. T. Nguyen, M. K. Bhaskar, R. E. Evans, F. Jelezko, and M. D. Lukin, "Silicon-Vacancy Spin Qubit in Diamond : A Quantum Memory Exceeding 10 ms with Single-Shot State Readout,", **223602**, 1–6 (2017). 2

[17] J. N. Becker, B. Pingault, D. Groß, M. Gündoğan, N. Kukharchyk, M. Markham, A. Edmonds, M. Atatüre, P. Bushev, and C. Becher, "All-Optical Control of the Silicon-Vacancy Spin in Diamond at Millikelvin Temperatures," Physical Review Letters **120**, 053603 (2018). 2

[18] G. H. Dieke, *Spectra and energy levels of rare earth ions in crystals* (Interscience, New York, 1968). 5, 7

[19] S. P. Horvath, J. V. Rakonjac, Y.-H. Chen, J. J. Longdell, P. Goldner, J.-P. R. Wells, and M. F. Reid, "A comprehensive understanding of ground and optically-excited hyperfine structure of ^{167}Er^{3+}:Y$_2$SiO$_5$," arxiv 1809.01058 (2018). 5, 6

[20] B. G. Wybourne, *Spectroscopic properties of rare earths* (Wiley, New York, NY, 1965). 7

[21] S. Hufner, "Optical Spectra of Transparent Rare Earth Compounds.," (2014). 7, 144

[22] G. Liu and B. Jacquier, eds., *Spectroscopic Properties of Rare Earths in Optical Materials*, vol. 83 of *Springer Series in Materials Science* (Springer-Verlag, Berlin/Heidelberg, 2005), ISBN 3-540-23886-7. 7, 21, 50

[23] A. Abragam and B. Bleaney, *Electron Paramagnetic Resonance of Transition Ions* (Oxford University Press, Oxford, 2012), ISBN 0191023000. 7, 19, 20

[24] A. Schweiger and G. Jeschke, "Principles of Pulse Electron Paramagnetic Resonance," Principles of Pulse Electron Paramagnetic Resonance (2001). 7

[25] R. M. Macfarlane and R. M. Shelby, in *Spectroscopy of Solids Containing Rare Earth Ions*, edited by A. A. Kaplyanskii and R. M. Macfarlane (Elsevier Science BV, North-Holland, 1987), chap. Coherent T. 7, 30, 31

[26] M. P. Hedges, J. J. Longdell, Y. Li, and M. J. Sellars, "Efficient quantum memory for light.," Nature **465**, 1052–1056 (2010). 8, 17

[27] M. Sabooni, Q. Li, S. Kröll, and L. Rippe, "Efficient quantum memory using a weakly absorbing sample," Physical Review Letters **110**, 133604 (2013). 17

[28] P. Jobez, I. Usmani, N. Timoney, C. Laplane, N. Gisin, and M. Afzelius, "Cavity-enhanced storage in an optical spin-wave memory," New Journal of Physics **16**, 083005 (2014). 8

[29] P. Jobez, C. Laplane, N. Timoney, N. Gisin, A. Ferrier, P. Goldner, and M. Afzelius, "Coherent Spin Control at the Quantum Level in an Ensemble-Based Optical Memory," Physical Review Letters **114**, 1–5 (2015). 8

[30] C. Laplane, P. Jobez, J. Etesse, N. Gisin, and M. Afzelius, "Multi-mode and long-lived quantum correlations between photons and spins in a crystal,", **210501**, 1–5 (2017). 8

[31] N. Sinclair, E. Saglamyurek, H. Mallahzadeh, J. A. Slater, M. George, R. Ricken, M. P. Hedges, D. Oblak, C. Simon, W. Sohler, et al., "Spectral Multiplexing for Scalable Quantum Photonics using an Atomic Frequency Comb Quantum Memory and Feed-Forward Control," Physical Review Letters **113**, 053603 (2014).

[32] P. Jobez, N. Timoney, C. Laplane, J. Etesse, A. Ferrier, P. Goldner, N. Gisin, and M. Afzelius, "Towards highly multimode optical quantum memory for quantum repeaters," Physical Review A - Atomic, Molecular, and Optical Physics **93**, 1–9 (2016). 8

[33] C. Laplane, P. Jobez, J. Etesse, N. Timoney, N. Gisin, and M. Afzelius, "Multiplexed on-demand storage of polarization qubits in a crystal," New Journal of Physics **18**, 013006 (2016). 8, 17

[34] E. Saglamyurek, J. Jin, V. B. Verma, M. D. Shaw, F. Marsili, S. W. Nam, D. Oblak, and W. Tittel, "Quantum storage of entangled telecom-wavelength photons in an erbium-doped optical fibre," Nature Photonics **9**, 83–87 (2015). 8

[35] A. I. Lvovsky, B. C. Sanders, and W. Tittel, "Optical quantum memory," Nature Photonics **3**, 706–714 (2009). 8

[36] C. Simon, M. Afzelius, J. Appel, A. Boyer de la Giroday, S. J. Dewhurst, N. Gisin, C. Y. Hu, F. Jelezko, S. Kröll, J. H. Müller, et al., "Quantum memories," The European Physical Journal D **58**, 1–22 (2010).

[37] K. Heshami, D. G. England, P. C. Humphreys, P. J. Bustard, V. M. Acosta, J. Nunn, and B. J. Sussman, "Quantum memories: emerging applications and recent advances," Journal of Modern Optics **63**, 2005–2028 (2016). 8

[38] L. A. Williamson, Y.-H. Chen, and J. J. Longdell, "Magneto-Optic Modulator with Unit Quantum Efficiency," Physical Review Letters **113**, 203601 (2014). 8

[39] C. O'Brien, N. Lauk, S. Blum, G. Morigi, and M. Fleischhauer, "Interfacing superconducting qubits and telecom photons via a rare-earth-doped crystal," Physical Review Letters **113**, 063603 (2014). 8

[40] X. Fernandez-Gonzalvo, Y. H. Chen, C. Yin, S. Rogge, and J. J. Longdell, "Coherent frequency up-conversion of microwaves to the optical telecommunications band in an Er:YSO crystal," Physical Review A - Atomic, Molecular, and Optical Physics **92**, 1–7 (2015). 8

[41] X. Fernandez-Gonzalvo, S. P. Horvath, Y.-H. Chen, and J. J. Longdell, "Cavity enhanced Raman heterodyne spectroscopy in Er:YSO for microwave to optical signal conversion," Arxiv 1712.07735 pp. 1–6 (2017). 8

[42] R. Kolesov, K. Xia, R. Reuter, R. Stöhr, a. Zappe, J. Meijer, P. Hemmer, and J. Wrachtrup, "Optical detection of a single rare-earth ion in a crystal," Nature Communications **3**, 1029 (2012). 8

[43] T. Utikal, E. Eichhammer, L. Petersen, a. Renn, S. Götzinger, and V. Sandoghdar, "Spectroscopic detection and state preparation of a single praseodymium ion in a crystal.," Nature Communications **5**, 3627 (2014). 8

[44] E. Eichhammer, T. Utikal, S. Götzinger, and V. Sandoghdar, "Spectroscopic detection of single Pr 3+ ions on the 3h4-1d2 transition," New Journal of Physics **17**, 083018 (2015). 8

[45] P. Siyushev, K. Xia, R. Reuter, M. Jamali, N. Zhao, N. Yang, C. Duan, N. Kukharchyk, a. D. Wieck, R. Kolesov, et al., "Coherent properties of single rare-earth spin qubits.," Nature communications **5**, 3895 (2014). 8

[46] K. Xia, R. Kolesov, Y. Wang, P. Siyushev, R. Reuter, T. Kornher, N. Kukharchyk, A. D. Wieck, B. Villa, S. Yang, et al., "All-Optical Preparation of Coherent Dark States of a Single Rare Earth Ion Spin in a Crystal," Physical Review Letters **115**, 093602 (2015). 8

[47] K. Xia, R. Kolesov, Y. Wang, P. Siyushev, T. Kornher, R. Reuter, and S. Yang, "Optical and spin properties of a single praseodymium ion in a crystal," arXiv:1706.08736v2 **4**, 2–6 (2017). 8

[48] T. Kornher, K. Xia, R. Kolesov, N. Kukharchyk, R. Reuter, P. Siyushev, R. Stöhr, M. Schreck, H.-w. Becker, B. Villa, et al., "Production yield of rare-earth ions implanted into an optical crystal Production yield of rare-earth ions implanted into an optical crystal," Applied Physics Letters **053108**, 1–5 (2015). 8

[49] K. Groot-Berning, T. Kornher, G. Jacob, F. Stopp, S. T. Dawkins, R. Kolesov, J. Wrachtrup, K. Singer, and F. Schmidt-Kaler, "Deterministic single ion implantation of rare-earth ions for nanometer resolution colour center generation," Arxiv 1902.05308 pp. 1–9 (2019). 8, 55

[50] A. M. Dibos, M. Raha, C. M. Phenicie, and J. D. Thompson, "Atomic Source of Single Photons in the Telecom Band," Physical Review Letters **120**, 243601 (2018). 8, 54, 56, 70, 129

[51] E. T. Miyazono, Ph.D. thesis, California Institute of Technology (2017). 9, 55, 56, 60

[52] E. Miyazono, I. Craiciu, A. Arbabi, T. Zhong, and A. Faraon, "Coupling erbium dopants in yttrium orthosilicate to silicon photonic resonators and waveguides," Optics Express **25**, 2863 (2017). 9, 15

[53] T. Zhong, J. Rochman, J. M. Kindem, E. Miyazono, and A. Faraon, "High quality factor nanophotonic resonators in bulk rare-earth doped crystals," Optics Express **24**, 536 (2016). 9, 11, 12, 17, 55

[54] S. Mosor, J. Hendrickson, B. C. Richards, J. Sweet, G. Khitrova, H. M. Gibbs, T. Yoshie, A. Scherer, O. Shchekin, and D. G. Deppe, "Scanning a photonic crystal slab nanocavity by condensation of xenon," Applied Physics Letter **87**, 10–13 (2005). 10, 62

[55] J. G. Bartholomew, T. Zhong, J. M. Kindem, R. Lopez-Rios, J. Rochman, I. Craiciu, E. Miyazono, and A. Faraon, "Controlling rare-earth ions in a nanophotonic resonator using the ac Stark shift," Physical Review A **97**, 1–13 (2018). 11, 15

[56] I. Diniz, S. Portolan, R. Ferreira, J. M. Gérard, P. Bertet, and A. Auffèves, "Strongly coupling a cavity to inhomogeneous ensembles of emitters: Potential for long-lived solid-state quantum memories," Physical Review A **84**, 063810 (2011). 13

[57] S. Putz, D. Krimer, R. Amsüss, A. Valookaran, T. Nöbauer, J. Schmiedmayer, S. Rotter, and J. Majer, "Protecting a spin ensemble against decoherence in the strong-coupling regime of cavity QED," Nature Physics **10**, 720–724 (2014). 13

[58] D. O. Krimer, S. Putz, J. Majer, and S. Rotter, "Non-Markovian dynamics of a single-mode cavity strongly coupled to an inhomogeneously broadened spin ensemble," Physical Review A **90**, 043852 (2014). 13

[59] S. Probst, H. Rotzinger, S. Wünsch, P. Jung, M. Jerger, M. Siegel, A. V. Ustinov, and P. A. Bushev, "Anisotropic rare-earth spin ensemble strongly coupled to a superconducting resonator," Physical Review Letters **110**, 1–5 (2013). 13

[60] E. Miyazono, T. Zhong, I. Craiciu, J. M. Kindem, and A. Faraon, "Coupling of erbium dopants to yttrium orthosilicate photonic crystal cavities for on-chip optical quantum memories," Applied Physics Letters **108** (2016). 15

[61] J. M. Kindem, J. G. Bartholomew, P. J. T. Woodburn, T. Zhong, I. Craiciu, R. L. Cone, C. W. Thiel, and A. Faraon, "Characterization of 171 Yb 3 + : YVO 4 for photonic quantum technologies," Phys. Rev. B **80**, 1–10 (2018). 17

[62] R. W. Equall, Y. Sun, R. L. Cone, and R. M. MacFarlane, "Ultraslow optical dephasing in Eu3+:Y2SiO5," Physical Review Letters **72**, 2179–2182 (1994). 17

[63] T. Böttger, C. W. Thiel, R. L. Cone, and Y. Sun, "Effects of magnetic field orientation on optical decoherence in Er:YSO," Physical Review B **79**, 115104 (2009).

[64] M. Zhong, M. P. Hedges, R. L. Ahlefeldt, J. G. Bartholomew, S. E. Beavan, S. M. Wittig, J. J. Longdell, and M. J. Sellars, "Optically addressable nuclear spins in a solid with a six-hour coherence time," Nature **517**, 177–180 (2015). 34

[65] M. Rančić, M. P. Hedges, R. L. Ahlefeldt, and M. J. Sellars, "Coherence time of over a second in a telecom-compatible quantum memory storage material," Nature Physics **14** (2017). 17, 63

[66] W. Tittel, M. Afzelius, T. Chaneliére, R. Cone, S. Kröll, S. Moiseev, and M. Sellars, "Photon-echo quantum memory in solid state systems," Laser & Photonics Reviews **4**, 244–267 (2009). 17

[67] E. Saglamyurek, N. Sinclair, J. A. Slater, K. Heshami, D. Oblak, and W. Tittel, "An integrated processor for photonic quantum states using a broadband light-matter interface," New Journal of Physics **16** (2014).

[68] M. Gündogan, P. M. Ledingham, K. Kutluer, M. Mazzera, and H. de Riedmatten, "Solid State Spin-Wave Quantum Memory for Time-Bin Qubits.," Physical Review Letters **114**, 230501 (2015). 17

[69] B. Lauritzen, S. R. Hastings-Simon, H. de Riedmatten, M. Afzelius, and N. Gisin, "State preparation by optical pumping in erbium-doped solids using stimulated emission and spin mixing," Physical Review A **78**, 043402 (2008). 17

[70] E. Baldit, K. Bencheikh, P. Monnier, S. Briaudeau, J. A. Levenson, V. Crozatier, I. Lorgeré, F. Bretenaker, J. L. Le Gouët, O. Guillot-Noël, et al., "Identification of lambda-like systems in Er:YSO and observation of electromagnetically induced transparency," Physical Review B **81**, 144303 (2010). 17

[71] S. Welinski, A. Ferrier, M. Afzelius, and P. Goldner, "High Resolution Optical Spectroscopy and Magnetic Properties of Yb 3 + in Y 2 SiO 5," Physical Review B **94**, 155116 (2016). 17, 18, 33

[72] A. Tiranov, A. Ortu, S. Welinski, A. Ferrier, P. Goldner, N. Gisin, and M. Afzelius, "Spectroscopic study of hyperfine properties in Yb-171:YSO," Physical Review B **98**, 195110 (2018). 18

[73] H.-J. Lim, S. Welinski, A. Ferrier, P. Goldner, and J. J. Morton, "Coherent spin dynamics of ytterbium ions in yttrium orthosilicate," Physical Review B **97**, 064409 (2018).

[74] A. Ortu, A. Tiranov, S. Welinski, F. Fröwis, N. Gisin, A. Ferrier, P. Goldner, and M. Afzelius, "Simultaneous coherence enhancement of optical and microwave transitions in solid-state electronic spins," Nature Materials **17**, 671–675 (2018). 17, 30, 35, 99, 105

[75] Z. Kis, G. Mandula, K. Lengyel, I. Hajdara, L. Kovacs, and M. Imlau, "Homogeneous linewidth measurements of Yb3+ ions in congruent and stoichiometric lithium niobate crystals," Optical Materials **37**, 845–853 (2014). 17

[76] T. Böttger, C. W. Thiel, R. L. Cone, Y. Sun, and A. Faraon, "Optical spectroscopy and decoherence studies of Yb^{3+}:YAG at 968 nm," Physical Review B **94**, 045134 (2016). 17, 27, 33

[77] H. de Riedmatten, M. Afzelius, M. U. Staudt, C. Simon, and N. Gisin, "A solid-state light-matter interface at the single-photon level.," Nature **456**, 773–7 (2008). 17

[78] C. Kränkel, D. Fagundes-Peters, S. T. Fredrich, J. Johannsen, M. Mond, G. Huber, M. Bernhagen, and R. Uecker, "Continuous wave laser operation of Yb3+: YVO4," Applied Physics B: Lasers and Optics **79**, 543–546 (2004). 18, 27

[79] R. Wyckoff, *Crystal Structures* (John Wiley & Sons, New York, NY, 1963), 2nd ed. 18

[80] E. V. Pestryakov, V. V. Petrov, V. I. Trunov, A. V. Kirpichnikov, M. A. Merzliakov, A. V. Laptev, and V. N. Matrosov, "Availability of new Yb:YV04 and Yb:GdxY(1-x)VO4 laser crystals for femtosecond laser systems at low temperature," Proc. of SPIE **6054** (2006). 19, 21

[81] U. Ranon, "Paramagnetic resonance of Nd3+, Dy3+, Er3+ and Yb3+ in YVO4," Physics Letters A **28**, 228–229 (1968). 21, 25

[82] E. C. Cook, P. J. Martin, T. L. Brown-Heft, J. C. Garman, and D. A. Steck, "High passive-stability diode-laser design for use in atomic-physics experiments," Review of Scientific Instruments **83**, 043101 (2012). 20, 66

[83] C. Wei, S. A. Holmstrom, N. B. Manson, J. P. D. Martin, X. F. He, and P. T. H. Fisk, "Raman heterodyne-detected magnetic resonance. Part 1. CW and coherent transient measurements," Appl. Magn. Reson. **11**, 521–538 (1996). 23, 30

[84] T. Blasberg and D. Suter, "Excitation of coherent Raman beats in rare earth solids with a bichromatic laser field," Optics Communications **109**, 133–138 (1994). 23

[85] T. Blasberg and D. Suter, "Bichromatic excitation of coherent Raman beats in rare-earth solids," Physical Review B **51**, 6309–6318 (1995). 32

[86] A. Walther, A. N. Nilsson, Q. Li, L. Rippe, and S. Kröll, "Fast all-optical nuclear spin echo technique based on EIT," European Physical Journal D **70** (2016).

[87] D. Serrano, J. Karlsson, A. Fossati, A. Ferrier, and P. Goldner, "All-optical control of long-lived nuclear spins in rare-earth doped nanoparticles," Nature Communications **9** (2018). 23

[88] B. Di Bartolo, *Optical interactions in solids* (Wiley, New York, 1968), ISBN 9789814295741. 25, 27

[89] B. Henderson and G. Imbush, *Optical spectroscopy of inorganic solids* (Oxford University Press, 2006), URL `http://linkinghub.elsevier.com/retrieve/pii/S1369702106716236`. 25, 27, 50, 144

[90] H. S. Shi, G. Zhang, and H. Y. Shen, "Measurement of refractive indices and thermal refractive index coefficients of \YVO\ crystal," J. Synth. Cryst **30**, 85–88 (2001). 26

[91] E. M. Purcell, "Spontaneous emission probabilities at radio frequencies," Physical Review **69**, 681 (1946). 27, 41

[92] D. S. Sumida and T. Y. Fan, "Effect of radiation trapping on fluorescence lifetime and emission cross section measurements in solid-state laser media," Optics Letters **19**, 1343 (1994). 27

[93] V. E. Kisel, S. E. Troshin, N. S. Tolstik, V. G. Shcherbitsky, N. V. Kuleshov, V. N. Matrosov, T. S. Matrosova, and M. I. Kupchenko, "Spectroscopy and continuous-wave diode-pumped laser action of Yb3+:YVO4.," Optics Letters **29**, 2491–3 (2004). 27

[94] T. Böttger, C. W. Thiel, Y. Sun, and R. L. Cone, "Optical decoherence and spectral diffusion at 1.5 μm in Er3+: Y2 SiO5 versus magnetic field, temperature, and Er3+ concentration," Physical Review B **73**, 075101 (2006). 28, 30, 54, 63

[95] W. Mims, "Phase Memory in Electron Spin Echoes, Lattice Relaxation Effects in CaWO4:Er, Ce, Mn," Physical Review **168**, 370–389 (1968). 29

[96] Y. Sun, C. W. Thiel, R. L. Cone, R. W. Equall, and R. L. Hutcheson, "Recent progress in developing new rare earth materials for hole burning and coherent transient applications," Journal of Luminescence **98**, 281–287 (2002). 30

[97] J. Ganem, Y. P. Wang, D. Boye, R. S. Meltzer, W. M. Yen, and R. M. Macfarlane, "Nonexponential Photon-Echo Decays of Paramagnetic Ions in the Superhyperfine Limit," Physical Review Letters **66**, 695–698 (1991). 30

[98] J. V. Rakonjac, Y.-H. Chen, S. P. Horvath, and J. J. Longdell (2018), 1802.03862, URL http://arxiv.org/abs/1802.03862. 30, 35, 99

[99] P. T. H. Fisk, X. F. He, K. Holliday, and N. B. Manson, "Anomalous lineshapes in Raman heterodyne detected EPR," Journal of Luminescence **45**, 26–28 (1990). 30

[100] J. Karlsson, N. Kunkel, A. Ikesue, A. Ferrier, and P. Goldner, "Nuclear spin coherence properties of 151Eu and 153Eu in a Y2O3 transparent ceramic," Journal of Physics Condensed Matter **29** (2017). 31

[101] R. L. Ahlefeldt, M. R. Hush, and M. J. Sellars, "Ultranarrow Optical Inhomogeneous Linewidth in a Stoichiometric Rare-Earth Crystal," Physical Review Letters **117**, 250504 (2016). 33

[102] J. G. Bartholomew, R. L. Ahlefeldt, and M. J. Sellars, "Engineering closed optical transitions in rare-earth ion crystals," Physical Review B **93**, 014401 (2016). 34

[103] R. J. Elliott and K. W. H. Stevens, "The Theory of Magnetic Resonance Experiments on Salts of the Rare Earths," Proceedings of the Royal Society A: Mathematical, Physical and Engineering Sciences **218**, 553–566 (1953). 34

[104] T. G. Tiecke, J. D. Thompson, N. P. De Leon, L. R. Liu, V. Vuletić, and M. D. Lukin, "Nanophotonic quantum phase switch with a single atom," Nature **508**, 241–244 (2014). 36, 38, 45, 46, 57

[105] E. Waks and D. Sridharan, "Cavity QED treatment of interactions between a metal nanoparticle and a dipole emitter," Physical Review A - Atomic, Molecular, and Optical Physics **82**, 1–14 (2010). 36, 47

[106] P. R. Rice and H. J. Carmichael, "Single-Atom Cavity -Enhanced Absorption I : Photon Statistics in the Bad-Cavity Limit,", **24**, 1351–1366 (1988). 36, 38, 39, 40, 50

[107] H. Carmichael, *Statistical methods in quantum optics: master equations and Fokker-Planck equations* (Springer, Berlin; London, 2011), ISBN 9783642081330 3642081339. 36, 38, 46

[108] D. A. Steck, "Quantum and Atom Optics," (2007). 37, 38, 40, 41, 46, 75

[109] C. Santori, D. Fattal, and Y. Yamamoto, *single-photon devices and applications* (Wiley-VCH, 2010), ISBN 978-3-527-40807-8. 37, 44, 81, 113, 127

[110] M. Fox, *Quantum optics: an introduction* (Oxford University Press, Oxford, 2006). 40, 81

[111] L. Allen and J. H. Eberly, *Optical resonance and two-level atoms* (Dover Publ., New York, 2014). 40

[112] J. Bylander, I. Robert-Philip, and I. Abram, "Interference and correlation of two independent photons," European Physical Journal D **22**, 295–301 (2003). 44

[113] T. Grange, G. Hornecker, D. Hunger, J. P. Poizat, J. M. Gérard, P. Senellart, and A. Auffèves, "Cavity-Funneled Generation of Indistinguishable Single Photons from Strongly Dissipative Quantum Emitters," Physical Review Letters **114**, 1–5 (2015). 44

[114] I. Fushman, D. Englund, A. Faraon, N. Stoltz, P. Petroff, and J. Vuc, "Controlled Phase Shifts with a Single Quantum Dot,", **320**, 769–773 (2008). 46

[115] J. Johansson, P. Nation, and F. Nori, "QuTiP 2: A Python framework for the dynamics of open quantum systems," Computer Physics Communications **184**, 1234–1240 (2013). 46

[116] F. J. P. Schuurmans, P. D. Vries, and A. Lagendijk, "Local-field effects on spontaneous emission of impurity atoms in homogeneous dielectrics," Physics Letters A pp. 472–477 (2000). 50, 51

[117] P. de Vries and A. Lagendijk, "Resonant scattering and spontaneous emission in dielectrics: Microscopic derivation of local-field effects," Physical Review Letters **81**, 1381–1384 (1998). 51

[118] H. T. Dung, S. Y. Buhmann, and D. G. Welsch, "Local-field correction to the spontaneous decay rate of atoms embedded in bodies of finite size," Physical Review A - Atomic, Molecular, and Optical Physics **74**, 1–11 (2006). 51

[119] J. Meijer, B. Burchard, M. Domhan, C. Wittmann, T. Gaebel, I. Popa, F. Jelezko, and J. Wrachtrup, "Generation of single color centers by focused nitrogen implantation," Applied Physics Letters **87**, 261909 (2005). 54

[120] R. Kolesov, K. Xia, R. Reuter, R. Stöhr, A. Zappe, J. Meijer, P. R. Hemmer, and J. Wrachtrup, "Optical detection of a single rare-earth ion in a crystal," Nature Communications **3** (2012). 55

[121] S. Gröblacher, J. T. Hill, A. H. Safavi-naeini, J. Chan, and O. Painter, "Highly efficient coupling from an optical fiber to a nanoscale silicon optomechanical cavity," Applied Physics Letters **181104** (2013). 57, 129

[122] L.-s. Ma, P. Jungner, J. Ye, and J. L. Hall, "Delivering the same optical frequency at two places : accurate cancellation of phase noise introduced by an optical fiber or other time-varying path," Optics letters **19**, 1777–1779 (1994). 67

[123] R. W. P. Drever, J. L. Hall, F. V. Kowalski, J. Hough, G. M. Ford, a. J. Munley, and H. Ward, "Laser phase and frequency stabilization using an optical resonator," Applied Physics B **31**, 97–105 (1983). 68

[124] E. D. Black, "An introduction to Pound – Drever – Hall laser frequency stabilization," American Journal of Physics pp. 79–87 (2001). 68

[125] F. Marsili, V. B. Verma, J. A. Stern, S. Harrington, A. E. Lita, T. Gerrits, I. Vayshenker, B. Baek, M. D. Shaw, R. P. Mirin, et al., "Detecting single infrared photons with 93% system efficiency," Nature Photonics **7**, 210–214 (2013). 70

[126] J. G. Bartholomew, Ph.D. thesis, Australian National University (2014). 76

[127] R. M. Macfarlane, "Optical Stark spectroscopy of solids," Journal of Luminescence **125**, 156–174 (2007). 79, 105

[128] K. A. Fischer, K. Müller, K. G. Lagoudakis, and J. Vučković, "Dynamical modeling of pulsed two-photon interference," New Journal of Physics **18**, 113053 (2016). 81, 84

[129] C. Santori, Ph.D. thesis, Stanford University (2003). 82

[130] C. Adetunmise, T. Silva, N. E. Ralph, M. Joanna, Y. Ju, D. Jin, and D. Brian, "Indistinguishable single photons with flexible electronic triggering," Optica **3**, 493–498 (2016). 84

[131] S. C. Kitson, P. Jonsson, J. G. Rarity, and P. R. Tapster, "Intensity fluctuation spectroscopy of small numbers of dye molecules in a microcavity," Physical Review A - Atomic, Molecular, and Optical Physics **58**, 620–627 (1998). 85

[132] I. Aharonovich, S. Castelletto, D. A. Simpson, A. D. Greentree, and S. Prawer, "Photophysics of chromium-related diamond single-photon emitters," Physical Review A - Atomic, Molecular, and Optical Physics **81**, 1–7 (2010). 85

[133] L. Besombes, C. Bougerol, M. Richard, S. Tatarenko, G. Sallen, A. Tribu, T. Aichele, R. Andre, K. Kheng, and J. Poizat, "Subnanosecond spectral diffusion measurement using photon correlation,", **4**, 2–5 (2010). 89

[134] E. Z. Cruzeiro, A. Tiranov, I. Usmani, C. Laplane, J. Lavoie, A. Ferrier, P. Goldner, N. Gisin, and M. Afzelius, "Spectral hole lifetimes and spin population relaxation dynamics in neodymium-doped yttrium orthosilicate," Physical Review B **95**, 205119 (2017). 91

[135] R. Hanson, O. Gywat, and D. D. Awschalom, "Room-temperature manipulation and decoherence of a single spin in diamond," Physical Review B - Condensed Matter and Materials Physics **74**, 1–4 (2006). 93

[136] V. V. Dobrovitski, A. E. Feiguin, R. Hanson, and D. D. Awschalom, "Decay of Rabi oscillations by dipolar-coupled dynamical spin environments," Physical Review Letters **102**, 1–4 (2009). 93, 111

[137] L. Robledo, H. Bernien, I. V. Weperen, and R. Hanson, "Control and Coherence of the Optical Transition of Single Nitrogen Vacancy Centers in Diamond," Physical Review Letters **177403**, 1–4 (2010). 93, 126

[138] D. L. McAuslan, J. G. Bartholomew, M. J. Sellars, and J. J. Longdell, "Reducing decoherence in optical and spin transitions in rare-earth-metal-ion–doped materials," Physical Review A **85**, 032339 (2012). 99

[139] G. De Lange, Z. Wang, S. Riste, V. V. Dobrovitski, and R. Hanson, "Universal Dynamical Decoupling of a Single Solid-State Spin from a Spin Bath," Science **330**, 60–64 (2010). 115, 117

[140] J. R. Klauder and P. Anderson, "Spectral Diffusion Decay in Spin Resonance Experiments," Physical Review **125** (1961). 115

[141] D. Suter and G. A. Álvarez, "Colloquium: Protecting quantum information against environmental noise," Reviews of Modern Physics **88**, 1–23 (2016). 116, 118

[142] M. J. Biercuk, A. C. Doherty, and H. Uys, "Dynamical decoupling sequence construction as a filter-design problem," Journal of Physics B: Atomic, Molecular and Optical Physics **44** (2011). 116, 117

[143] N. Zhao, J. Honert, B. Schmid, M. Klas, J. Isoya, M. Markham, D. Twitchen, F. Jelezko, R. B. Liu, H. Fedder, et al., "Sensing single remote nuclear spins," Nature Nanotechnology **7**, 657–662 (2012). 117, 127

[144] S. Kolkowitz, Q. P. Unterreithmeier, S. D. Bennett, and M. D. Lukin, "Sensing distant nuclear spins with a single electron spin," Physical Review Letters **109**, 1–5 (2012). 117, 127

[145] Ł. Cywiński, R. M. Lutchyn, C. P. Nave, and S. Das Sarma, "How to enhance dephasing time in superconducting qubits," Physical Review B - Condensed Matter and Materials Physics **77**, 1–11 (2008). 117

[146] N. Bar-Gill, L. Pham, C. Belthangady, D. Le Sage, P. Cappellaro, J. Maze, M. Lukin, A. Yacoby, and R. Walsworth, "Suppression of spin-bath dynamics for improved coherence of multi-spin-qubit systems," Nature Communications **3**, 856–858 (2012). 117

[147] N. Bar-Gill, L. M. Pham, A. Jarmola, D. Budker, and R. L. Walsworth, "Solid-state electronic spin coherence time approaching one second," Nature Communications **4**, 1743–1746 (2013). 119

[148] J. Medford, Ł. Cywiński, C. Barthel, C. M. Marcus, M. P. Hanson, and A. C. Gossard, "Scaling of Dynamical Decoupling for Spin Qubits," Physical Review Letters **108**, 086802 (2012). 119

[149] C. W. Thiel, W. R. Babbitt, and R. L. Cone, "Optical decoherence studies of yttrium oxyorthosilicate Y2SiO5 codoped with Er and Eu for optical signal processing and quantum information applications at 1.5 microns," Physical Review B **85**, 174302 (2012). 120, 126

[150] S. Welinski, C. Thiel, J. Dajczgewand, A. Ferrier, R. Cone, R. Macfarlane, T. Chanelière, A. Louchet-Chauvet, and P. Goldner, "Effects of disorder on optical and electron spin linewidths in Er 3+ ,Sc 3+ :Y 2 SiO 5," Optical Materials **63**, 69–75 (2017). 120, 126

[151] T. H. Taminiau, J. Cramer, T. van der Sar, V. V. Dobrovitski, and R. Hanson, "Universal control and error correction in multi-qubit spin registers in diamond," Nature Nanotechnology **9**, 171–176 (2014). 127

[152] T. H. Taminiau, J. J. T. Wagenaar, T. van der Sar, F. Jelezko, V. V. Dobrovitski, and R. Hanson, "Detection and Control of Individual Nuclear Spins Using a Weakly Coupled Electron Spin," Physical Review Letters **109**, 137602 (2012). 127

[153] G.-Q. Liu, J. Xing, W.-l. Ma, P. Wang, C.-h. Li, H. C. Po, Y.-r. Zhang, H. Fan, R.-b. Liu, and X.-y. Pan, "Single-Shot Readout of a Nuclear Spin Weakly Coupled to a Nitrogen-Vacancy Center at Room Temperature," Physical Review Letters **118**, 150504 (2017). 127

[154] S. D. Barrett and P. Kok, "Efficient high-fidelity quantum computation using matter qubits and linear optics," Physical Review A **71**, 060310 (2005). 128

[155] T. G. Tiecke, K. P. Nayak, J. D. Thompson, T. Peyronel, N. P. de Leon, V. Vuletić, and M. D. Lukin, "Efficient fiber-optical interface for nanophotonic devices," Optica **2**, 70 (2015). 129

[156] R. C. Powell, *Symmetry, group theory, and the physical properties of crystals* (Springer, New York, 2010), URL http://site.ebrary.com/id/10434901. 144

Appendix A

TRANSITION SELECTION RULES IN ^{171}YB:YVO_4

In this chapter, I work through the basics of the transition selection rules and state assignment for the ^{171}Yb:YVO_4 spectroscopy. The idea here is to make the connection between the group theoretical picture and the more user friendly spin Hamiltonian picture used in the text. The main goal is to show we can use the symmetry of the crystal and the observed transitions rules to assign the appropriate labels to the energy states.

There are many fine references that approach this problem and provide an introduction to group theory in the specific context of energy levels in crystals. I am largely working from Powell 2010 [156]. Hendersen and Imbusch [89] and Hufner [21] are both nice references with worked examples for transition selection rules in other symmetries. For working through calculations, there are many useful tables that can be found in Koster [5][1]. Note that here the goal is to predict relative transition strengths. Mike Reid's chapter in Jacquier and Liu
citeLiu2005 is a good reference for getting an idea of how one would go about predicting transition strengths from the full crystal field theory.

The basic idea is that we start with a crystal symmetry and want to write down the states of the ion in terms of irreducible representations of that group. For a given symmetry, we can write down how the electric and magnetic dipole operators transform and thus can determine the selection rules between the different irreducible representations. We then figure out the corresponding labels for the observed states in our system by measuring which optical transitions are observed in the crystal for different orientations of the input light relative to the crystal symmetry axes (e.g. polarization along or perpendicular to c with light propagating along or perpendicular to c).

A.1 Setting up the problem

The $4f^{13}$ configuration of Yb^{3+} consists of only two electronic multiplets: $^2F_{\frac{7}{2}}$ in the ground state and $^2F_{\frac{5}{2}}$ in the excited state. In the crystal field of YVO_4, these

[1] This text can be difficult to find, but a quick internet search will find these tables reproduced in a variety of places.

split into 4 and 3, respectively, Kramers doublets. Yb substitutes for Y in sites of D_{2d} point symmetry. The character table for D_{2d} is given in Table A.1:

Table A.1: Character table for D_{2d}

Powell	Koster	E	$\bar{E}$	$2S_4$	$2\bar{S}_4$	$C_2/\bar{C}_2$	$C_2'/\bar{C}'_2$	$\sigma_d/\bar{\sigma}_d$	
A_1	Γ_1	1	1	1	1	1	1	1	
A_2	Γ_2	1	1	1	1	1	-1	-1	
B_1	Γ_3	1	1	-1	-1	1	1	-1	
B_2	Γ_4	1	1	-1	-1	1	-1	1	z
E	Γ_5	2	2	0	0	-2	0	0	x,y
$D_{1/2}$	Γ_6	2	-2	$\sqrt{2}$	$-\sqrt{2}$	0	0	0	
${}_2D$	Γ_7	2	-2	$-\sqrt{2}$	$\sqrt{2}$	0	0	0	

We then want to write the spin-orbit multiplets(${}^2F_{\frac{5}{2}}$ and ${}^2F_{\frac{7}{2}}$)in terms of the irreducible representations of this symmetry. We can get these from (e.g. Powell p. 89). For an operator with rotation through angle α where j is the angular momentum, we have

$$\chi(\alpha) = \frac{\sin[(j+\frac{1}{2})\alpha]}{\sin[\frac{\alpha}{2}]} \tag{A.1}$$

$$\chi(E) = 2j+1 \tag{A.2}$$

$$\chi(R) = -(2j+1). \tag{A.3}$$

The resulting character table for the spin-orbit multiplets is given in Table A.2.

Table A.2: Character table for angular momentum states

j	$\chi(E)$	$\chi(S_4)$	$\chi(C_2)$
5/2	6	$\sqrt{2}$	0
7/2	8	0	0

We can see by inspection that $\Gamma_{\frac{5}{2}} = 2\Gamma_6 + \Gamma_7$ and $\Gamma_{\frac{7}{2}} = 2\Gamma_6 + 2\Gamma_7$. This is to say that the ${}^2F_{\frac{7}{2}}$ and ${}^2F_{\frac{5}{2}}$ multiplets will split into crystal field levels that will be either Γ_6 or Γ_7.

We are measuring the optical transitions between the lowest energy crystal field levels of ${}^2F_{\frac{7}{2}}$ and ${}^2F_{\frac{5}{2}}$. Now the question is which states do we have? (i.e. are these

states both Γ_6, both Γ_7, or one of each?) We can figure this out by looking at the dipole selection rules. From e.g. table 33 of Koster, the electric dipole operator behaves as Γ_4 for $E \parallel c$ (π polarization) and as Γ_5 for $E \perp c$ (σ polarization). We can then calculate the selection rules between the different states. In short, a transition between reps Γ_i and Γ_j is for the dipole operator with rep Γ_x if $\Gamma_x \times \Gamma_j$ contains Γ_i. This gives rise to the selection rules shown in A.3.

Table A.3: Electric dipole selection rules in D_{2d}

	Γ_6	Γ_7
Γ_6	σ	π, σ
Γ_7	π, σ	σ

In our system, we find that the 984 nm optical transition exists for both π and σ polarizations, which implies that one state is Γ_6 and the other is Γ_7.

Let's then add in the nuclear spin of the Yb-171 isotope. The nuclear spin $1/2$ goes as Γ_6 (e.g. Koster Table 33). Then by coupling the electron and nuclear spin the states become (Koster Table 34)

$$\Gamma_6 \times \Gamma_6 = \Gamma_1 + \Gamma_2 + \Gamma_5 \tag{A.4}$$

$$\Gamma_6 \times \Gamma_7 = \Gamma_3 + \Gamma_4 + \Gamma_5. \tag{A.5}$$

That is to say, by introducing the nuclear spin we split into three levels in the ground and excited state as observed. Γ_5 corresponds to the $|S = 1, m_s = \pm 1\rangle$ state (i.e. this is the doubly degenerate state). Looking at Table 39 of Koster, we see that Γ_1 and Γ_3 correspond with the antisymmetric $|S = 0, 0\rangle$ state while Γ_2 and Γ_4 correspond with the symmetric $|S = 1, m_s = 0\rangle$ state.

Now let us look at the optical transitions allowed between these states. Again, the electric dipole operator behaves as Γ_4 for $E \parallel c$ (π polarization) and as Γ_5 for $E \perp c$ (σ polarization). We can then derive the electric dipole transition selection rules for the zero field states using e.g. Table 34 from Koster as given in Table A.4.

From this, we see that at zero field we expect three π-polarized transitions and four σ-polarized transitions, which is what we observe! We also note that the $\Gamma_1 \to \Gamma_3$ ($|00\rangle \to |00\rangle$) and $\Gamma_2 \to \Gamma_4$ ($|10\rangle \to |10\rangle$) transitions are forbidden. This then helps the assignment to the order of the energy levels based on the observed transitions.

Table A.4: Electric dipole transition selection rules

	Γ_1	Γ_2	Γ_5
Γ_3	-	π	σ
Γ_4	π	-	σ
Γ_5	σ	σ	π

Further, we can observe how the transitions split in a magnetic field. We observe that highest energy optical transition splits into four in an applied magnetic field, which means that the degenerate state $|1 \pm 1\rangle$ is lowest in energy in the ground state and the highest energy in the excited state. There is then still a sign ambiguity on the ordering of the $|00\rangle$ and $|01\rangle$ states. This ambiguity can be resolved from the measured values of g and A, which (through judicious following of Eliot and Stevens) fixes the order of these states.

The ordering of the states is then (from low to high) $|1 \pm 1\rangle$, $|00\rangle$, $|01\rangle$ for the ground state manifold and $|00\rangle$, $|01\rangle$, $|1 \pm 1\rangle$ for the excited state.

A.2 Calculating transition strengths from the spin Hamiltonian

The transition strength S_{ij} between the two states $|i\rangle$ and $|j\rangle$ goes as

$$S_{ij} \sim \left|\langle i| \hat{P}_\alpha |j\rangle\right|^2, \tag{A.6}$$

where $\hat{P}_\alpha$ is the electric dipole operator for the α polarization. In terms of our spin Hamiltonian, we can write the electric dipole operator for light polarized along z as

$$\hat{P}_z = \sigma_{z,e} \otimes \mathbb{I}_n, \tag{A.7}$$

where $\sigma_{z,e}$ is the Pauli z matrix acting on the electron spin basis and $\mathbb{I}_n$ is the identity on the nuclear spin basis. From above, we see that $\hat{P}_z$ transforms as Γ_4 and we can do similar for the other polarizations. The nuclear spin contribution to the optical transition strength is then given by the overlap of these states. In the spin Hamiltonian language, we'll use the basis of the form

$$\begin{pmatrix} |\uparrow\uparrow\rangle \\ |\uparrow\downarrow\rangle \\ |\downarrow\uparrow\rangle \\ |\downarrow\downarrow\rangle, \end{pmatrix}, \tag{A.8}$$

where our notations is $|m_e, m_n\rangle$, with $|\uparrow\rangle \rightarrow m_s = +1/2$ and $|\downarrow\rangle \rightarrow m_s = -1/2$. We can then write $\hat{P}_z$ as

$$\hat{P}_z = \begin{pmatrix} 1 & 0 & 0 & 0 \\ 0 & 1 & 0 & 0 \\ 0 & 0 & -1 & 0 \\ 0 & 0 & 0 & -1 \end{pmatrix}. \tag{A.9}$$

We can then check that the selection rules in the spin Hamiltonian picture match those given by the group theoretical approach:

$$\langle 1 \pm 1 | \hat{P}_z | 1 \pm 1 \rangle \neq 0, \tag{A.10}$$

which correspond to the $\Gamma_5 \rightarrow \Gamma_5$ transition being allowed for π polarization. And similarly,

$$\langle 10 | \hat{P}_z | 10 \rangle = 0 \tag{A.11}$$

$$\langle 00 | \hat{P}_z | 00 \rangle = 0 \tag{A.12}$$

$$\langle 10 | \hat{P}_z | 00 \rangle \neq 0 \tag{A.13}$$

So we have $\Gamma_2 \rightarrow \Gamma_4$ and $\Gamma_1 \rightarrow \Gamma_3$ are not allowed for π polarization, while $\Gamma_1 \rightarrow \Gamma_4$ and $\Gamma_3 \rightarrow \Gamma_2$ are allowed. In a similar way, one can also show that σ polarization transition rules in the spin Hamiltonian picture have been properly mapped to the selections we predict.